Development and early testing of a novel axial-flow Left Ventricular Assist Device (LVAD) configuration

Andrea Guadalupe Sanchez Aguilar

MSc in Experimental Surgery

Department of Surgery

McGill University

Montreal, Quebec

August 2020

A thesis submitted to McGill University in partial fulfillment of the requirements of the degree of Master of Science

ABSTRACT

The use of continuous Left Ventricular Assist Devices (LVADs) as a treatment for patients with advanced heart failure has exhibited better clinical outcomes than medical management and first-generation pulsatile pumps. Although these devices improve quality of life, patients still suffer from adverse events after implantation, such as infections, bleeding, hemolysis, and thrombosis. Studies suggest that these complications are due to the non-physiological flow mechanics to which blood is exposed when in contact with the device. Ongoing research focuses on the evaluation of different geometries and pump configurations aiming to develop improved devices. The purpose of this study is to demonstrate the proof-of-concept of a novel axial-flow LVAD configuration through the assessment of the characteristic performance curves of the pump. The singularity of this design departs fully from the conventional axial pump morphology as the blades are mounted on the outer part of the device, increasing thus, the cross-sectional area for blood carriage through the central hollow space. This configuration also opens the possibility of having a fully collapsible pump with a complete minimally-invasive delivery procedure. Using CFTurbo software, the pump geometry was designed at a Design Operating Point (DOP) of pressure rise ΔP=6.666 x 10^3 Pa [50 mmHg], flow rate Q=5 x 10^{-5} m s^{-3} [3 L $\min^{-1}$], and a rotational speed N =335.1 rad s^{-1}[3200 RPM]. Then, two different versions of the pump with similar external diameter *OD* of 2.5 x 10^{-2} m and different blade radial extensions *b* of 7 x 10^{-3} m (Design A) and 9 x 10^{-3} m (Design B) were created to evaluate particular percentages of flow guided by the blades. Using ANSYS CFX, a Computational Fluid Dynamic (CFD) simulation was developed to evaluate pressure rise ΔP, flow rate Q, high wall shear stress regions, and Reynolds number Re of both pump design variations at rotational speeds N of $209.4, 335.1, 418.8, 628.3,$ and 837.7 rad s^{-1}[200, 3200, 4000,6000, and 8000 RPM]. Lastly, the in-vitro hydraulic evaluation of Design A was performed in a constructed test-rig and a comparison between experiments and virtual predictions was assessed. Overall the pump provided flow rates of 8.33 x 10^{-6} m s^{-3} [0.5 L $\min^{-1}$] to 5.83 x 10^{-5} m s^{-3} [3.5 L $\min^{-1}$], pressure rises of 6.66 x 10^2 Pa [5 mmHg] to 5.332 x 10^3 Pa [40 mmHg], and hydraulic efficiencies of 4% to 12% at rotational speeds *N*= $209.4, 335.1,$ and 418.8 rad s^{-1} [2000, 3200, and 4000 RPM]. The novel pump concept can provide circulatory support for patients with heart failure but with reduced pressure rise. Therefore, further design optimization is required to reach optimal physiological pressures for left ventricular assistance ΔP of 6.66 x 10^3 Pa [50 mmHg] to 13.33 x 10^3 Pa [100 mmHg]. This feasibility study generates a starting point for future device development.

RÉSUMÉ

L'utilisation de dispositifs continus d'assistance ventriculaire gauche (LVADs en anglais) en tant que traitement pour les patients ayant des insuffisances cardiaques graves s'est avérée fournir de meilleurs résultats que les traitements médicaux classiques ou que les pompes pulsatives de première génération. Bien que ces appareils permettent d'améliorer la qualité de vie du patient, ceux-ci souffrent néanmoins d'effets secondaires après implantation tels que des infections, des saignements ou bien d'hémolyse ou de thrombose. Des études suggèrent que ces complications sont dues aux écoulements mécaniques non physiologiques auxquels le sang est exposé lorsqu'il entre en contact avec le dispositif. Aujourd'hui, la recherche se concentre sur l'évaluation de différentes géométries et configurations de pompes dans le but de concevoir des dispositifs plus performants. L'objectif de cette étude est d'obtenir une démonstration de faisabilité d'une nouvelle pompe ventriculaire axiale. La conception de cette pompe diffère grandement de la conventionnelle pompe axiale car les aubes sont montées à l'extérieur du dispositif, laissant un conduit intérieur pour le transport du sang. Cette configuration permet également de réduire la taille du dispositif et donc de faciliter son implantation chirurgicale minimalement invasive. L'utilisation du logiciel CFTurbo a permis de concevoir la pompe axiale au point de fonctionnement suivant: taux de $\Delta P = 6.66 \text{ x } 10^3$ Pa, débit de $Q = 5 \text{ x } 10^{-5}$ m s^{-3} et une vitesse de rotation de $N = 335.1$ rad s^{-1}. Deux prototypes ont été développés afin d'évaluer l'influence de la taille des aubes sur les performances mécaniques de la pompe. Plus précisément, chacun des prototypes possède un diamètre externe *OD* de *OD* de 2.5×10^{-2} m mais different par leurs tailles d'aubes; le Prototype A possède des aubes de rayon $b = 7 \text{ x } 10^{-3}$ m alors que le Prototype B possède des aubes de rayons $b = 9 \text{ x } 10^{-3}$ m. Le logiciel ANSYS CFX a été utilisé pour simuler l'écoulement au travers de la pompe et d'évaluer des performances de celle-ci (taux de ΔP, débit Q, contraintes de cisaillement τ…) pour différentes vitesses de rotation N allant de $209.4, 335.1, 418.8, 628.3,$ à 837.7 rad s^{-1}. Enfin, le Prototype A a été testé expérimentalement sur un banc d'essai hydraulique et les résultats ont été comparés aux simulations numériques. Dans l'ensemble, la pompe a fourni un débit volumique allant de $8.33 \text{ x } 10^{-6}$ m s^{-3} à $5.83 \text{ x } 10^{-5}$ m s^{-3}, une augmentation de pression de $6.66 \text{ x } 10^2$ Pa à $5.33 \text{ x } 10^3$ Pa, et un rendement hydraulique entre 4% et 12% pour des vitesses de $209.4, 335.1,$ et 418.8 rad s^{-1}. Par conséquent, cette nouvelle pompe est capable de fournir un écoulement sanguin pour les patients atteints d'insuffisances cardiaques mais avec une augmentation de pression. Ainsi, davantage de travail et de développement sont nécessaires pour atteindre les pressions physiologiques optimales de $6.66 \text{ x } 10^3$ Pa a $13.33 \text{ x } 10^3$ Pa. La présente recherche sert donc de point de départ satisfaisant pour des études ultérieures.

ACKNOWLEDGEMENTS

To my academic supervisor Dr. Renzo Cecere, for trusting in my skills and for having given the opportunity to collaborate in this ambitious and visionary project.

To my co-supervisor, Dr. Rosaire Mongrain, for providing space in his laboratory and for facilitating resources for the realization of the project.

To Prof. Nedic, Prof. Amabili, Prof. Leask, Mathieu Beauchesne, Greg, and Mario Locabaccio, from the department of Mechanical Engineering, for facilitating tools and equipment.

To Dr. Pramod Bonde, for giving me the opportunity to collaborate and deepen my knowledge in the field at Yale University.

To the Mexican National Council for Science and Technology (CONACYT), MITACS Globalink Program, The Research Institute of MUHC, and McGill University, for providing funding.

To Line Desssureault, Jennifer Marcotte, Sharon Turner, and Dr. Anie Philip, for their assistance in administrative matters.

To my peers from the "Grad Café” and office mates, for sharing their technical expertise which facilitated the resolution of research related problems and for creating a friendly work environment.

To Paola Ulacia, Sandybel Angeles and Twisha Singh for becoming my family in Montreal.

To Khristopher McGill for his unwavering patience and for staying close despite the distance.

To my parents and sisters, for their unconditional love and constant support.

TABLE OF CONTENTS

NOMENCLATURE

List of abbreviations

Abbreviation	*Meaning*
LVAD	Left Ventricular Assist Device
CO	Cardiac output
CFH	Congestive heart failure
HFrEF	Heart failure with reduced ejection fraction
HF	Heart failure
LV	Left ventricle
NYHA	New York Health Association
ACC	American College of Cardiology
AHA	American Heart Association
CIHI	Canadian Institute of Health Information
CPB	Cardiopulmonary bypass
IABPs	Intra-aortic balloon pumps
VADs	Ventricular assist devices
FDA	Food and Drug Administration
BTT	Bridge-to-transplant
FDA	Food and Drug Administration
REMATCH	Randomized Evaluation of Mechanical Assistance for the Treatment of Congestive Heart Failure
DT	Destination therapy
INTERMACS	Interagency Registry for Mechanically Assisted Circulatory Support
NIH	National Institutes of Health
MagLev	Magnetic-levitating
RBC	Red blood cells
CFD	Computational Fluid Dynamics
pfHb	Plasma free hemoglobin
TiN	Titanium nitride

DLC	Diamond-like carbon
MPC	2-methacryloyloxyethyl phosphorylcholine
EC	Endothelial cell
DOP	Design operating point
HQ Curve	Head-Flow curve
η Curve	Hydraulic efficiency curve
WSS	Wall shear stress
BLDC	Brushless direct-current
DC	Direct-current
LE	Leading edge
TE	Trailing edge
RANS	Reynolds Averaged Navier Stokes
cP	Centipoise
RMS	Root mean square
CAD	Computer-aided drawing
PTFE	Polytetrafluoroethylene
PLA	Polylactic acid
FDM	Fused deposition modeling
SLA	Stereolithography
UV	Ultraviolet
PID	proportional–integral–derivative
e(t)	Error
PV	Process variable
SP	Set point
G(s)	Transfer function
DAQ	Data acquisition card
LSM	Least-squares method
PCU	Pressure control unit

LIST OF SYMBOLS

Symbol	Meaning	Units
$\dot{\gamma}$	Shear rate	$[\mathrm{s}^{-1}]$
ΔP	Pressure rise, pressure head	[Pa, mmHg]
H	Head	[m]
Q	Flow rate	$[\mathrm{m}^3\mathrm{s}^{-1}, \mathrm{L\ min}^{-1}]$
N	Rotational speed	$[\mathrm{rad\ s}^{-1}, \mathrm{RPM}]$
D_s	Specific diameter	[n/a]
N_s	Specific speed	[n/a]
V_a	Axial component of flow velocity	$[\mathrm{m\ s}^{-1}]$
V_r	Radial component of flow velocity	$[\mathrm{m\ s}^{-1}]$
V_u	Tangential component of flow velocity	$[\mathrm{ms}^{-1}]$
U_m	Tangential velocity of the impeller at r_m	$[\mathrm{m\ s}^{-1}]$
r_m	Mean radius	[m]
r_t	Impeller tip radius	[m]
r_h	Impeller hub radius	[m]
U_1	Velocity at the inlet of the pump	$[\mathrm{m\ s}^{-1}]$
U_2	Velocity at the outlet of the pump	$[\mathrm{m\ s}^{-1}]$
V_{a1}	Axial component of velocity at the inlet of the pump	$[\mathrm{m\ s}^{-1}]$
V_{a2}	Axial component of velocity at the outlet of the pump	$[\mathrm{m\ s}^{-1}]$
V_m	Meridional axial component of flow velocity	$[\mathrm{m\ s}^{-1}]$
A	Cross-sectional area for flow	$[\mathrm{m}^2]$
A_1	Cross-sectional area for flow at the inlet of the pump	$[\mathrm{m}^2]$
A_2	Cross-sectional area for flow at the outlet of the pump	$[\mathrm{m}^2]$
g	Gravitational acceleration	$[\mathrm{m\ s}^{-2}]$
ΔH	Head rise	[m]
V_{u1}	Tangential component of velocity at the inlet of the pump	$[\mathrm{m\ s}^{-1}]$

V_{u2}	Tangential component of velocity at the outlet of the pump	[m s^{-1}]
D_t	Impeller tip diameter	[m]
D_h	Impeller hub diameter	[m]
D_m	Impeller mean diameter	[m]
b	Blade radial extension	[m]
s	Pitch	[m]
Z_b	Number of blades	[n/a]
ν	Hub-ratio	[n/a]
c/s	Solidity	[n/a]
c	Chord	[m]
U	Tangential velocity vector	[m s^{-1}]
W	Relative velocity vector	[m s^{-1}]
V	Absolute or total velocity vector	[m s^{-1}]
V_{a1}	Axial component of velocity at the inlet section of the impeller	[m s^{-1}]
V_{a2}	Axial component of velocity at the outlet section of the impeller	[m s^{-1}]
V_{u1}	Tangential component of velocity at the inlet section of the impeller	[m s^{-1}]
V_{u2}	Tangential component of velocity at the outlet section of the impeller	[m s^{-1}]
U_1	Tangential blade velocity at the inlet	[m s^{-1}]
U_2	Tangential blade velocity at the outlet	[m s^{-1}]
W_1	Relative blade velocity at the inlet	[m s^{-1}]
W_2	Relative blade velocity at the outlet	[m s^{-1}]
β_1	Inlet relative angle measured from the axial direction	[$\circ$]
β_2	Outlet relative angle measured from the axial direction	[$\circ$]
α_1	Inlet angle of the diffuser blades	[$\circ$]
$\dot{m}$	Mass flow rate	[kg s^{-1}]
μ	Dynamic viscosity	[Pa s, cP]
ρ	Density	[kg m^{-3}]

D	Diameter	[m]
η	Hydraulic efficiency	[n/a]
P_o	Useful output power	[Watts]
P_h	Hydraulic power	[Watts]
P_i	Input energy	[Watts]
P_m	Mechanical power	[Watts]
ϕ	Wrap angle	[$\circ$]
τ	Torque or shear stress or wall shear stress	[N m or Pa or Pa]
Re	Reynolds number	[n/a]
d	Internal diameter of the pipe or impeller diameter	[m]
ψ	Head coefficient	[n/a]
Φ	Flow coefficient	[n/a]
Π	Power coefficient	[n/a]
P_s	Shaft power	[Watts]
ψ_m	Head coefficient of the model	[n/a]
Φ_m	Flow coefficient of the model	[n/a]
$\mathit{\Pi}_m$	Power coefficient of the model	[n/a]
ψ_p	Head coefficient of the prototype	[n/a]
Φ_p	Flow coefficient of the prototype	[n/a]
Π_p	Power coefficient of the prototype	[n/a]
ID	Hollow hub diameter (internal diameter)	[m]
OD	Shroud diameter (external diameter)	[m]
Z	Total axial extension of the pump	[m]
$\mathit{\Delta} t$	timestep	[s]

LIST OF TABLES

LIST OF FIGURES

CHAPTER 1: INTRODUCTION

1.1 Motivation

Since the 1980s, the prevalence of heart failure (HF), along with the number of patients treated with Left Ventricular Assist Devices (LVADs) has increased. These devices have evolved from pulsatile operated pumps to continuous-flow rotary machines. Aside from being characterized by having smaller and more durable designs, continuous-flow implantable LVAD designs are known for having an internal rotating component (i.e., impeller or rotor) through which circulatory support flow is administered to the patient.

Although continuous-rotary LVADs improve quality of life and survival rates of patients with HF (Class III and Class IV), a significant number of patients still suffer from adverse events, such as infections, bleeding, thrombosis, and hemolysis. Pump-related infections are a consequence of the external driveline of the pump, while bleeding, thrombosis, and hemolysis are caused by the non-physiological induced flow of the device.

Axial-flow blood pumps are known for having the highest operating regime in terms of rotational speed. This results in increased shear stresses and blood damage. Therefore, ongoing research focuses on the evaluation of different pump geometries and configurations aiming to reduce shear forces linked to blood trauma.

Up to date, there is no way to completely eradicate blood trauma, however, having a close-to-fully biocompatible axial-flow blood pump for long-term therapy with minimally invasive implantation approaches, remains an unmet clinical need in the field of mechanical circulatory support.

1.2 Product Concept, Goal, Hypotheses and Research Objectives

Supporting the theory that adverse events in axial-flow blood pumps are repercussions of the morphology and the high rotational speeds at which the pump rotates, a novel LVAD configuration has been put forward (Fig. 1.1), US 9,726,195 B2, herein referred to as the 'hubless' axial-flow blood pump.

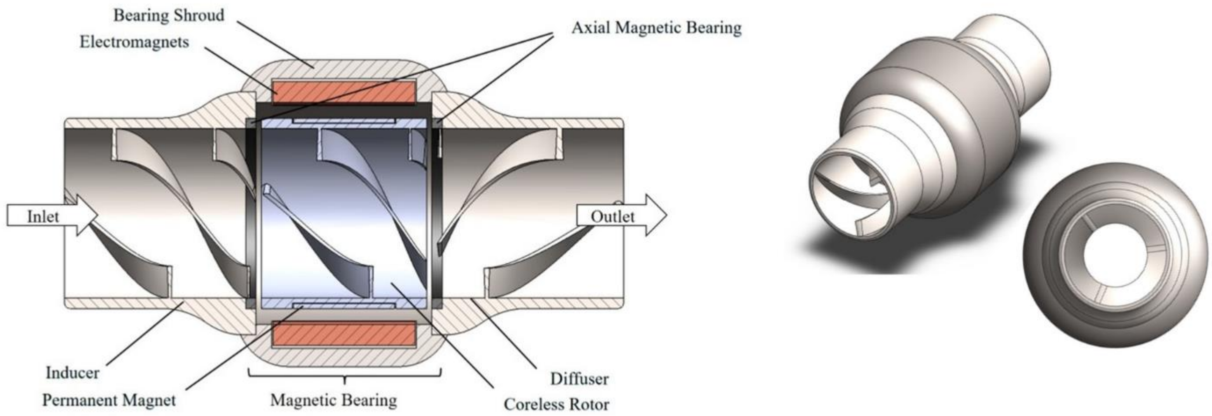

Figure 1.1 Hubless pump concept (left). Isometric and front views (right).

The geometric singularity of this configuration relies on the way the blades are mounted on the pump. Unlike conventional axial-flow blood pumps, the blades are fixed on a shroud, providing thus, an increased cross-sectional area for flow passage and a larger pumping volume through unit time. The theoretical advantage of this configuration is the reduction of the rotational speed to achieve certain flow rate. Hence, the flow velocity gradients and the stress levels linked to blood damage would decrease [1-3]. Similarly, the hollow central space opens the possibility of having a fully collapsible pump for a complete minimally-invasive delivery procedure.

The main goal of this project is to demonstrate the proof-of-concept of the novel 'hubless' LVAD configuration in terms of prototype development and preliminary testing to validate the concept for future device development.

In this study, it has been hypothesized that successful partial circulatory support for patients with heart failure is achievable with the axial 'hubless' LVAD configuration.

The research objectives are as follows:

1. Define an initial geometry of the 'hubless' concept using turbomachinery concepts.
2. Conduct performance testing of the 'hubless' concept to analyse achievable flow rates and pressure rise.

1.3 Thesis Overview

Chapter 1 provides a general introduction to the project. Chapter 2 is divided into four sections. The first part provides an overview of the structural and physiological characteristics of the circulatory system. The second section covers the condition of interest: heart failure. The third section expands on the use of mechanical circulatory support devices as treatment option for patients with end-stage heart failure, along with a brief explanation of current technologies, and the state of art of left ventricular assist devices. And the last section explores mechanical approaches used in LVAD design, testing, and optimization. Chapter 3 describes the methods and approaches used for LVAD design of the novel 'hubless' concept along with the materials/equipment required to virtually and experimentally characterize the performance of the pump. Chapter 4 presents the results. And Chapter 5 discusses the results, the significance of findings in view of current limitations, and suggested future work for the continuation of the project.

CHAPTER 2: LITERATURE REVIEW

2.1 Cardiovascular Physiology

This section provides an overview of the structural and physiological characteristics of the circulatory system. Mean pressures and blood flow are briefly discussed, and Congestive Heart Failure (CHF) is introduced.

2.1.1 Circulatory System

The circulatory system (Fig. 2.1) is a complex and vital structure. It contains blood vessels entering and exiting the heart to transport nutrients and oxygen to the body through the pumping action of the heart. Blood vessels are categorized according to their flow direction and size. Arteries are the strongest and thicker vessels in the circulatory system since their main function is to transport oxygenated blood at high pressure from the heart to the systemic circulation. The veins are thinner because they carry deoxygenated blood at low pressure from body to the lungs through the pulmonary circulation. The largest artery in the human body is the aorta with an average diameter of 3×10^{-2} m [4]. Due to their location, blood through the arteries flows at higher velocities than in the veins.

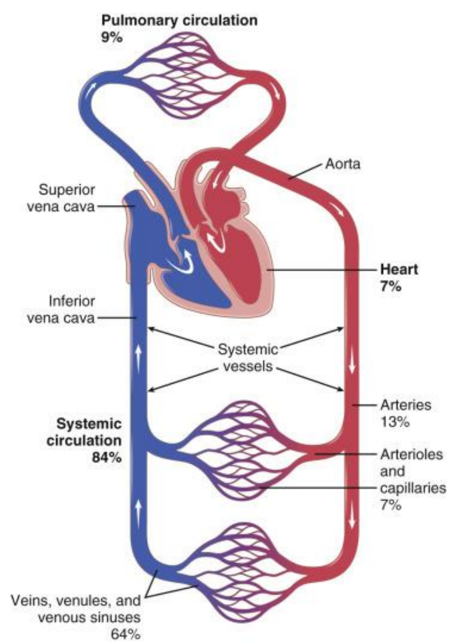

Figure 2.1 Circulatory system. Reprinted with permission from [4].

2.1.2 The Heart

The heart is divided in two sides (Fig. 2.2), the right and the left side. Each side of the heart has two chambers separated by heart valves, in order to prevent backflow to other cavities. The first chamber is the atrium, whose function is to transport blood into the second chamber known as ventricle [4]. Figure 2.3 shows the schematic connection between the right and left heart. The right side of the heart receives deoxygenated blood from the body through the vena cava and transports it through the pulmonary artery to the lungs (pulmonary circulation). The left side of the heart receives oxygenated blood from the lungs through the pulmonary veins and pumps it through the aorta to the rest of the body (systemic circulation). Due to the nature of its function, the anatomical structure of the left side of the heart has thicker walls and muscles when compared to the right side of the heart.

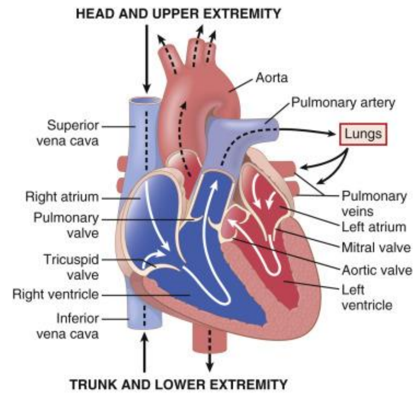

Figure 2.2 Flow pathways through the heart.

Reprinted with permission from [4].

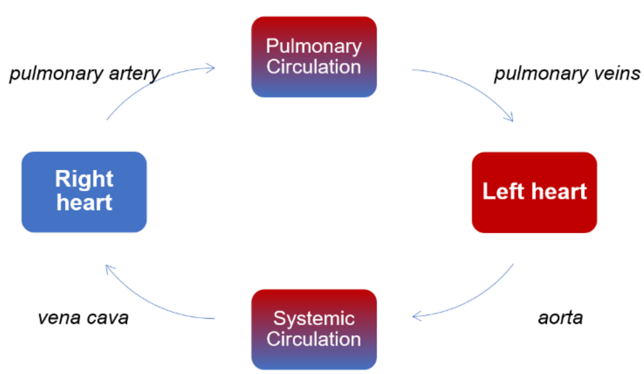

Figure 2.3 Connection between the right and the left heart. Adapted from [5].

2.1.3 Cardiac Cycle

The cardiac cycle occurs in two periods, a period of contraction known as systole and a period of relaxation known as diastole. Systole is characterized by the ejection of blood to the body, whereas diastole is the part of the cycle during which the ventricles fill with blood.

Figure 2.4 represents several events occurring during the cardiac cycle for the left side of the heart. The curve on top along with the black dashed curves represent the pressure changes in the aorta, left ventricle, and left atrium during the cardiac cycle. Mean systolic and diastolic pressures at rest condition through the aorta is 1.6×10^{4} Pa [120 mmHg] and 1.0667×10^{4} Pa [80 mmHg] respectively [4].

The second curve represents the change of volumetric load. As seen in the image, the left ventricles require higher volume of blood than the right ones and the atriums, because the pressure needed to pump blood through the body is higher than the pressure needed to fill the lungs.

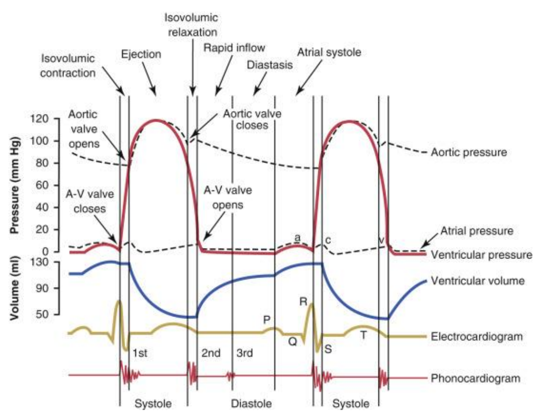

Figure 2.4 Events of the cardiac cycle for left ventricular function.
Reprinted with permission from [4].

2.1.4 Blood Flow and Cardiac Output

Blood flow rate quantifies the amount of blood that passes through a blood vessel per unit of time and the average flow rate of an adult at rest is $8.33 \times 10^{-5}\ \mathrm{m^3\ s^{-1}}$[5 $\mathrm{L\ min^{-1}}$] . Blood flow is also known as cardiac output (CO) [4], and it varies depending on several factors such as the age, the size of the body, the metabolism, and most importantly, the level of physical activity. If measured in the ascending aorta, CO of a health adult oscillates from $8.33 \times 10^{-5}\ \mathrm{m^3\ s^{-1}}$ [5 $\mathrm{L\ min^{-1}}$] to $3.33 \times 10^{-4}\ \mathrm{m^3\ s^{-1}}$ [20 $\mathrm{L\ min^{-1}}$] from rest to exercise, respectively. Congestive

Heart Failure (CHF) is a severe cardiovascular condition and it arises by the inability of the heart to generate enough cardiac output.

2.2 Clinical Background: Congestive Heart Failure

This section aims to provide the reader a brief overview Congestive Heart Failure (CFH). Current statistics and future epidemiologic projections of the disease. Treatment options, and the introduction of mechanical circulatory support as treatment for patients with end-stage heart failure.

Congestive heart failure (CHF) is a serious cardiovascular disease associated with a substantial death rate. It occurs when the heart is unable to pump enough blood to the body and it can affect the right, left, or both sides of the heart.

Because the right-side affliction generally results from left heart failure, the present study focusses only in the systolic heart failure, also known as reduced ejection fraction (HFrEF) of the left ventricle (LV). HFrEF is characterized by the reduction of oxygenated blood towards the systemic circulation branches occasionated by the loss of contraction capability of the left ventricle [6] [7].

Worldwide, the prevalence of HF reaches up to approximately 26 million people. In the US, from 2011 to 2014, 6.5 million people over the age of 20 had heart failure [8-11]. Projections for the next decades show a rise on the incidence of patients diagnosed with heart failure as the aging population continues to elongate [12-14]. Although aging is not a direct cause of heart failure, the cardioprotective system gradually lose its integrity [15] triggering thus, the initiation processes of the disease.

Congestive Heart Failure can be classified in two different ways. As a functional classification by New York Heart Association (NYHA), in which CHF is divided into four categories (I, II, III, IV) depending on the severity of the symptoms [16] or as an objective assessment by the American College of Cardiology (ACC)/American Heart Association (AHA) (Stages A, B, C, D) [6, 17].

CHF is a progressive condition as it gets worse with time. Treatment options for heart failure depend on the stage of the disease, from mild pre-heart failure to end-stage, the options are: changes on lifestyle (e.g. exercising regularly, quit smoking) to surgical procedures such as the coronary bypass, heart valve replacement, long-term mechanical support devices and heart transplant; last one only available for patients with end-stage HF (Class III-IV) [6, 18].

Although heart transplant is the gold standard for end-stage HF, this alternative is limited to the number of available heart donors. The Canadian Institute of Health Information (CIHI) reported in 2017 that the growing number of patients on the wait-list for heart transplants has overpassed the heart transplants since 2007 [19]. Due to the increasing demand and the constant supply, many patients die on the waitlist wishing for a chance of survival [20-22].

In the late 1960s and early 1970s, visionary people started to devise ways to artificially assist the heart. Originating thus, the field of mechanical circulatory support (MCS). During these decades, innovation in cardiac surgical procedures became a key component for the development of mechanical assist devices. Since then, many kinds of mechanical assist devices have been developed to assist the heart, such as the cardiopulmonary bypass machines (CPB), intraortic balloon pumps (IABPs), and Ventricular Assist Devices (VADs), being the last one, a promising long-lasting therapy for patients with CHF.

2.3 Left Ventricular Assist Devices (LVADs)

This section provides an overview of LVADs used to treat heart failure. A historical review of LVAD evolution and a brief explanation of current technologies and challenges. Towards the end of the section, the state of novel designs aiming to overcome challenges and biocompatibility limitations of current devices is also included.

LVADs also known as heart pumps, are electromechanical pumps used to partially assist patients with end-stage heart failure. These devices emerged to offer temporary support to patients waiting for a heart transplant, also known as bridge-to-transplant (BTT) therapy.

2.3.1 Historical Review

Precursors devices, such as the expandable chamber by Dr. Kantrowitz (1963) [23] and the gas-energized synchronized left ventricular bypass pump by Dr. DeBakey (1966) [24], emerged in the late 1960s to offer an opportunity to patients with cardiac dysfunction. Initially, the development and clinical assessment of these initial devices were regulated by individual academic medical centers until the FDA started regulating medical devices research(1976). [25, 26]. The first successful bridge-to-transplant LVAD procedure was performed in 1978 [27] and from there until the late 1990s, the boom of heart pumps began. The evolution of LVADs has been divided in generations of development, and each generation has its own characteristic principle of operation:

First Generation

First-generation LVADs were characterized by having a pulsatile volume displacement mechanism. The principle of operation relies on the application of an external pneumatic or electric force, applied to a collapsible blood chamber with two unidirectional flow valves, one at the inlet and the other at the outlet of the chamber. This mechanism induced pulsatility, mimicking thus, the pumping action of a native heart [6].

First-generation pumps were implanted intracorporeal or extracorporeal, according to the manufacturer’s design. Figure 2.5 shows some first-generation displacement pumps.

Figure 2.5 First-Generation LVADs. (A) Thoratec Intracorporeal (IVAD), (B) Thoratec Paracorporeal, (C) Berlin Heart EXCOR, and (D) HeartMate XVE.

It was not until 2001 that first-generation LVADs proved to offer clinical benefits as a result of a REMATCH trial [28]. This study compared two groups of patients with HF Class IV. The first group composed of 68 patients was treated with LVAD therapy, whereas the other one, with 61 patients, received optimal medical management. Outcomes of the study showed that with LVAD therapy, 48% reduction in risk of death after 12 months was observed when compared to the medical management therapy, and most importantly, it provided enough scientific evidence for FDA approval of LVADs as destination therapy (DT) in 2003 [6, 26].

Although the REMATCH trial reported advantages against conventional therapy, patients receiving LVAD therapy had significant complications as 35% of the pumps failed within a time-frame 24 months [28] and the patients had double the incidences of infection and bleeding, compared with the patients treated with conventional medical therapy [6]. These disadvantages led to the second-generation.

Second Generation

The first second-generation implantation procedure was performed in the late 1980s [29] and it was the first time the continuous rotary mechanism was explored, characteristic principle of operation of second-generation pumps. In contrast with the first-generation, second generation devices do not imitate the pulsatility of the native heart; instead, they provide continuous alternative flow path to simultaneously support to the pumping function of the heart.

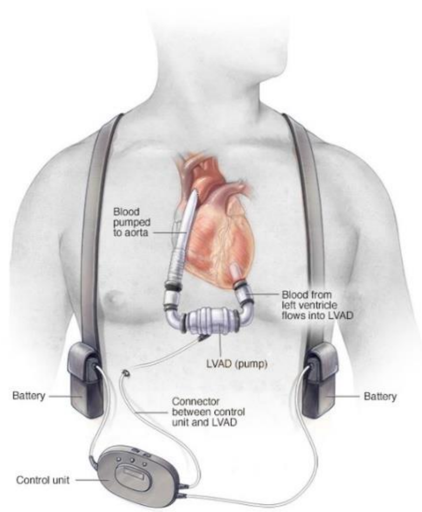

Figure 2.6 LVAD placement configuration.

Reprinted with permission from Mayo Clinic [30]

A conventional continuous rotary pump system (Fig. 2.6) consists of an implantable LVAD, a percutaneous cable that connects the pump to a wearable external control unit, rechargeable batteries, a battery charger, and an external power supply. Blood within the pump flows from the apex of the left ventricle to the inlet of the pump through an inflow graft. The control unit stores process and collect data to drive the central rotary part (rotor or impeller) of the implantable LVAD. The modulation of rotating speed and generated flow rate is given by a feedback control of the data acquisition system. The activated rotor pushes blood towards an outflow graft anastomosed to the ascending aorta. Creating thus, an alternative parallel blood pathway to the conventional blood flow within the left side of the heart. Within the pump, the flow depends on the morphology of the impeller. In general, an impeller is a rotating component with airfoil blades which transfers energy from the power supply unit to the fluid. More details about the fluid fundamentals involved in LVAD design are given in the following subsection.

Continuous rotary pumps are classified according to the blood flow direction as either axial-flow, radial-flow, and mixed-flow machines. Figure 2.7 shows the most common types of LVADs machines. In axial-flow pumps (Fig. 2.7 [left]), blood enters and discharges the impeller in a parallel direction to the rotation axis. In a radial-flow pump (Fig. 2.7 [right), also known as centrifugal configuration, blood enters the pump parallel to the rotation axis, then travels radially through the impeller blades by centrifugal forces, and discharges blood perpendicularly the rotation axis of the impeller [6, 31]. Figure 2.8 shows some examples of second-generation continuous rotary LVADs.

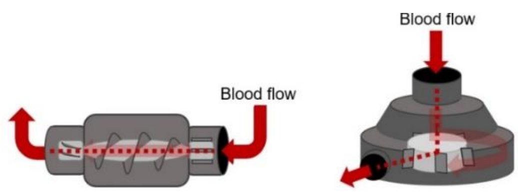

Figure 2.7 Continuous rotary LVAD configurations. Axial-flow pump (left) and centrifugal-flow pump (right).

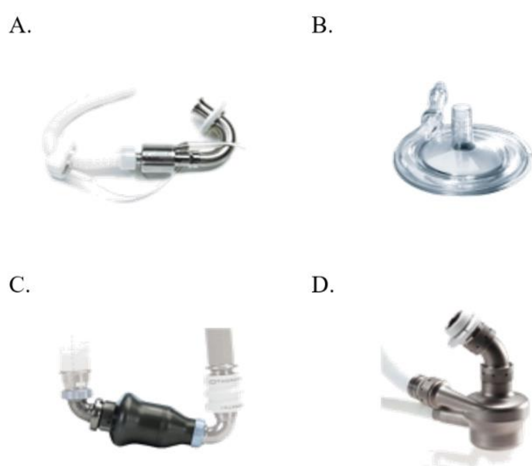

Figure 2.8 Second-Generation LVADs. (A) HeartAssist 5, (B) RotaFlow, (C) HeartMate II, and (D) EvaHeart.

The Interagency Registry for Mechanically Assisted Circulatory Support (INTERMACS) was founded in 2006 as a result of a collaboration between the National Institutes of Health (NIH), the FDA and Center for Medicare & Medicaid Services [25, 26] to maintain record and analyze patient's outcomes treated with different LVAD configurations.

It took almost two decades since the beginning of second-generation LVADs, for a randomized study to compare a second-generation LVAD (HeartmateII, Thoratec Corporation) with a first-generation (Heartmate XVE, Thoratec Corporation) pump [32]. The study included 200 patients with CHF (Class IIIB or IV) who aleatory received a first or second-generation LVAD. Outcomes of the study showed that although both devices improved the functional capacity and quality of life, the second-generation device significantly improved, followed two years, the stroke-free survival with less device failure as compared with the first-generation pump [6].

Miller (2013) supported the outcomes of the study with a two-year survival rate study in which she compared medical management therapy, pulsatile first-generation LVADs, and continuous rotary second-generation pumps. The study showed that, for patients with advanced HF, continuous flow LVADs had the highest percentages of survival rate when compared with first-generation pump therapy and medical management.

Second-generation LVADs exhibit great reliability and hemocompatibility for short-term therapy as they are designed to address the drawbacks of large, bulky and noisy first-generation pumps. Although these devices are used with great success nowadays, ongoing research aims to reduce biocompatibility limitations that these devices bring after implantation to achieve a long-term therapy [6, 28, 32-34].

Third Generation

The third and latest generation of LVADs became advantageous due to their small size, and lack of bearings to maintain the rotor centered inside the housing of the pump. In this context, impellers of this generation have incorporated a magnetically levitating principle to avoid any mechanical contact with the stationary parts of the pump. One of the latest third-generation LVAD approved for destination therapy is HeartMate 3 (HM3) by Abbott Laboratories [35, 36].

The fully magnetic-levitating (MagLev) technology emerged to address the mechanical wear associated with bearings of second-generation LVADs, since bearing systems are essential contributors to low hemocompatibility [33, 37]. The levitating concept for blood pumps was initially described in 1969 [38]. But it was not until 1995 that the first extracorporeal third-generation assistive device (Centrimag, Abbott Laboratories) was commercialized. In 2002, the first implantation of an intracorporeal third-generation (INCOR, Berlin Heart) pump was performed [6].

A recently published multicenter clinical trial assessed the long-term outcomes of the MagLev technology [39, 40]. MOMENTUM 3 study compares the magnetic levitating centrifugal-flow pump (HM3, Abbott Laboratories) with the mechanical-bearing axial-flow pump (HM2, Abbott Laboratories) in patients with advanced heart failure (Class IIIB or IV). Where 190 patients were assigned to the centrifugal-flow pump treatment and 176 to the axial-flow pump treatment. The two-year study demonstrated that although the rates of death were similar in both groups, less reoperation for pump malfunction, lower rate of stroke, and less thrombotic events occurred in the third- generation device group when compared to the second generation device group, proving thus, promising long-term advantages of the MagLev technology.

2.3.2 Continuous Rotary LVAD in a Biological Environment

Although continuous rotary pumps have met the perfusion requirements for patients with advanced HF, blood damage remains a problem as a result of mechanical stresses, high temperatures, turbulence, cavitation, and foreign materials to which blood is exposed [6, 41]. To delve into the non-physiological device-blood interaction, it is important to understand blood and its rheological behavior

Blood is a complex heterogeneous tissue composed of a fluid portion called plasma and three major types of blood cells:

- Erythrocytes or red blood cells (RBC), which contain a special protein called hemoglobin and whose main function is to transport oxygen from the lungs to the tissues of the body through. RBC represent 95% of all cells present in blood.
- White cells or leukocytes, protectors of external organisms and involved in immune functions representing 0.15% of all cells and

- Platelets or thrombocytes involved in homeostasis and blood clotting processes. Representing less than 5% of all cells [42].

RBC have no nuclei and their flexible structure and unusual bioconcave-bioconvex shape allows them to align with flow direction. Due to their deformability, their aggregation capacity, and its concentration in blood (hematocrit); blood behaves as a Non-Newtonian fluid [42, 43].

A Newtonian fluid is one in which viscosity at fixed temperature and pressure is independent to shear stress [44], whereas a Non-Newtonian fluid is a fluid whose viscosity is variable depending on the applied stress or force (Fig. 2.10), and it does not obey Newton's law of viscosity:

$$\tau = \mu\,\dot{\gamma} \tag{2.1}$$

where τ represents shear stress, μ represents viscosity, and $\dot{\gamma}$ represents shear rate.

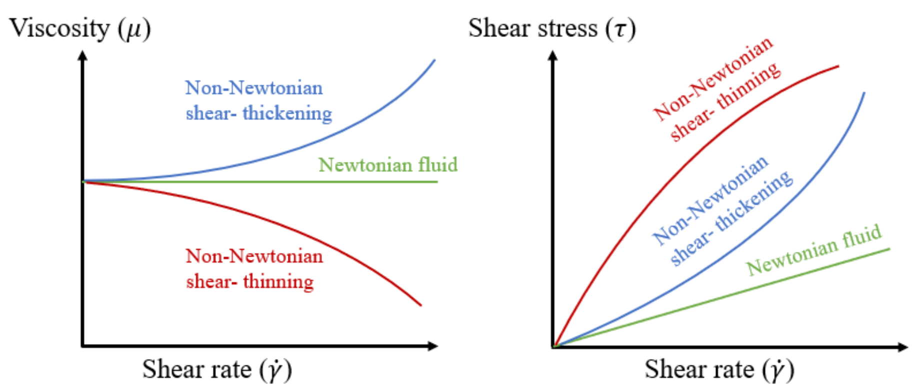

Figure 2.9 Rheological properties of fluids. Adapted from [43].

While blood plasma is considered a Newtonian fluid, blood as a whole follows a Non-Newtonian behaviour. When blood is exposed to high shear rates, RBC rearrange and align with the flow direction due to their viscoelastic interaction. Causing a reduction of resistance in the fluid, thus a reduction in viscosity. On the contrary, when blood is subject to small shear rates or no flow, blood forms stacks of aggregated RBC, known as rouleaux [41-43]. These adaptive forms give blood its characteristic shear-thinning behaviour.

Dynamic viscosity of blood (μ) ranges between $3.23 \text{ x } 10^{-3}$ Pa s to $4.20 \text{ x } 10^{-3}$ Pa s [4] and it varies depending on the hematocrit levels. Blood viscosity is considered to have a constant value (Newtonian behaviour) above non-physiological high shear rates ($> 100\ s^{-1}$), such as the case of LVADs [44, 45]. The assumption of blood as an incompressible fluid with constant viscosity is widely used to model blood in Computational Fluid dynamic (CFD) simulations to analyse LVAD-blood interaction [45-49].

Current LVADs rely on the rotary principle which induces blood flow through the rotation of an impeller. Therefore, blood prolongated contact and collision with surfaces of biomaterials at high shear stress regions have undesirable effects on blood cells. In fact, blood is exposed to high mechanical shear stresses of ~ 1000 Pa in the presence of continuous rotary pumps, which is two orders of magnitude higher than the normal physiological shear stresses (usually less than 10 Pa) [6, 50]. High shear stress regions lead to gradual or abrupt release of hemoglobin to the plasma due to the degradation and eventual rupture of the erythrocyte cell membrane [6, 51]. The rupture of RBC is known as hemolysis and the measurement of plasma hemoglobin (pfHb) in blood quantifies the level of hemolysis[43, 52].

Blood damage is originated under the effect of an external force at a specific amplitude and frequency over a period of time. Although many computational, in vitro, and in vivo studies have investigated the rupture of RBC aiming to reduce the hemodynamic risk induced by LVADs [45, 48, 49, 53-56]; the processes leading to hemolysis have not yet fully described [6, 41, 43].

At the beginning, it was believed that a minimal hemolysis threshold of ~ 150 Pa could cause direct cell damage [51]. However, recent studies estimate that short-term exposure ranging between 400 Pa to 600 Pa is required to induce significant hemolysis [57-59].

Apart from the rupture of RBC, due to the unnatural exposure to non-physiological environments (e.g.: high shear, high rotational speeds) and biomaterial surfaces, activated platelets trigger the clotting cascade, leading to the formation of a blood cloths. These blood cloths impede the flow of blood within the vessel or can cause the device to fail (LVAD thrombosis) [41, 60]. A high incidence of thrombolytic events is one of the major limitations of ventricular assist devices [33]. Hence, patients implanted heart pumps are usually treated with anticoagulants (e.g.: heparin, bivalirudin, warfarin, aspirin, clopidogrel, etc.) to prevent the coagulopathic response. Increasing thus, the unexpected risk of bleeding and infection [6, 41].

Up to date, more than 18,000 patients with LVAD support have entered into the INTERMACS database, and recent reports indicate that bleeding and infections are the most predominately adverse events in patients with LVAD support, followed by neurological dysfunction complications [41, 61, 62].

Infections can be classified as LVAD-specific infections (the ones related to hardware e.g.: pump and percutaneous driveline infection, pocket infection or cannula infection), LVAD-related infections (the ones that can also occur in patients who do not have LVADs e.g.: infective endocarditis, blood stream infection or mediastinitis), and non-LVAD infections in LVAD recipients [63]. Driveline infections are the most common type of LVAD-specific infections [64, 65] because the driveline exit site creates an easy port of entry for bacteria to form biofilms.

In this context, the selection of biomaterials for blood-contacting surfaces is essential for improved hemocompatibility. Besides stainless steel, titanium, its alloys, and polyurethane are excellent material used in LVADs due to their biocompatibility and mechanical properties [66]. Likewise, LVADs use surface coatings to reduce thrombosis and infections. Coatings can be categorized in: inorganics (e.g.: polished titanium nitride [TiN], diamond-like carbon [DLC]), organics (e.g: 2-methacryloyloxyethyl phosphorylcholine [MPC] polymer), and bio-actives (e.g.: heparin, textured surfaces, endothelial cell [EC] linings) [66].

Since several studies show an association between thrombus formation, infections, bleeding and strokes with the mortality rate and LVAD replacement [61, 65, 67], blood trauma remains a major challenge in LVAD design [41].

2.3.3 Current Trends and Advancements in LVAD Techology

The global Ventricular Assist Device market was valued at USD 1.15 billion in 2018. By 2022, it is expected to reach around USD 2.5 billion and is anticipated to increase at a compound annual growth rate of 11.4% over 2025 [68, 69].

Continuous-rotary LVADs occupy approximately 85% of the total VAD market. Therefore, second and third generation devices such as Jarvik 2000 (Jarvik Heart Inc.), Incor (Berlin Heart), DuraHeart (Terumo Heart), HeartMate II and III (Thoratec now Abbot Laboratories), and HVAD (HeartWare now Medtronic) play an important role for the long-term circulatory support.

The observation of current challenges and rapid evolution of LVADs have opened new opportunities to search for improved alternatives. One if the latest advance in circulatory support, is the miniaturization of these devices, such as the HVAD by HeartWare now Medtronic and HeartMate III by Thoratec now Abbot Laboratories. These devices offer less invasive surgical procedures with smaller incisions (thoracotomy or median sternotomy) when compared with the classic implantation procedures (full sternotomy).

While miniaturization and improved surgical techniques for a less invasive surgical procedures are still being investigated, it is of primary importance for physicians and engineers to evaluate whether new designs are biocompatible over the long run.

Novel advancements, departing totally from existing LVAD technologies, are attempting to demonstrate benefits over conventional continuous rotary pump approaches [70]. For instance, Neptune by CorWave, incorporates a membrane technology which provides a pulsatile flow following the heart rate [71]; the automatic synchronous pulsatile support of TORVAD with adjustable flow rate to demand [72]; and the EVAHEART pump, which respects heart native pulsatility and includes a new cannulation technique [73].

Likewise, progress towards a fully-implantable LVAD to eliminate the percutaneous driveline infection using transcutaneous wireless energy transfer systems is being investigated [74-77]. The first LVAD implanted with this technology was the LionHeart 2000 (Arrow International) [78], and the last one, the Jarvik 2000 (Jarvik Heart Inc.), using Leviticus Cardio's wireless power transfer technology [79].

Up to date, there is no way to completely eliminate blood damage produced by LVADs [41], however, the acceptability of novel and improved technologies rely on three main aspects.

1. Device-minimization
2. Closeness to a "minimally-invasive" implantation procedure, and
3. The ability to provide superior or comparable performance (e.g.: lower shear stresses) with significant blood-trauma reduction [6, 70].

2.4 LVAD Mechanic Design Fundamentals

This section explores the fundamentals of turbomachinery applied in LVAD design, the conventional steps for axial pump design, the basis for numerical and experimental performance analysis, and a brief introduction to design optimization using similarity laws.

2.4.1 Turbomachinery-based LVAD Design Procedure

Continuous rotary LVADs are considered to be turbomachines because, similar to industrial pumps, their main function is to transfer mechanical energy to generate flow [80, 81].

Energy transformation within a pump occurs in stages [31]. The first stage takes place when the pump receives electric energy from the power source and converts it into mechanical energy to activate the impeller, the second stage occurs as a result of the rotating motion of the impeller because the fluid velocity rises, and the last one occurs when the kinetic energy is transformed into pressure as a result of the diffusion process at the outlet of the impeller [31, 82].

According to turbomachinery theories [31, 83] and LVAD design methodology [6], the efficiency point at which the LVAD should operate in terms of pressure rise ΔP or head *H*, flow rate Q and *N* [31]. Since head and flow are parameters conditioned by the system in which they are located [84]; LVAD applications target to achieve flow rates Q of $1.66 \text{ x } 10^{-5}\ \mathrm{m^3 s^{-1}}$ to $8.33 \text{ x } 10^{-5}\ \mathrm{m^3 s^{-1}}$[18, 85] at physiological relevant pressures of $\Delta P \approx$ $6.66 \text{ x } 10^3$ to $13.33 \text{ x } 10^3$ Pa [41, 45]. The rotating speed *N* is estimated to meet the above mentioned flow and pressure conditions [83].

Having established the DOP in terms of *N* *Q* and *H*; specific speed N_s can be defined in a dimensional and non-dimensional form as

$$\frac{NQ^{1/2}}{H^{3/4}} \text{ and} \tag{2.2}$$

$$\frac{NQ^{1/2}}{(gH)^{3/4}} \tag{2.3}$$

respectively; where *N* is the rotating speed, *Q* is flow rate, *H* is head, and g is gravity.

The specific speed allows the estimation of a proper impeller type for a given application. The use of a Cordier diagram (Fig. 2.11) [86] facilitates the process as it shows the correlation between non-dimensional specific speed, non-dimensional specific diameter (to be defined later), and the types of impellers for single stage pumps.

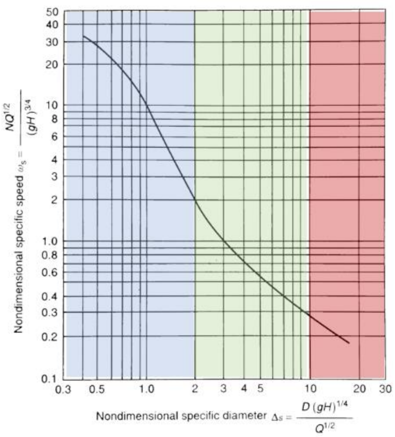

Figure 2.10 Non-dimensional N_s and D_s correlation with impeller types.

Adapted from [31].

Figure 2.12 shows a derived dimensional form of the Cordier diagram illustrating the impeller types for a given N_s. It can be observed that for pumps operating at N_s below 10000, the radial or centrifugal-flow and mixed-flow impeller configurations are selected, whereas axial-flow impellers are selected when the pump is expected to operate at N_s between 10000 and 15000 [31].

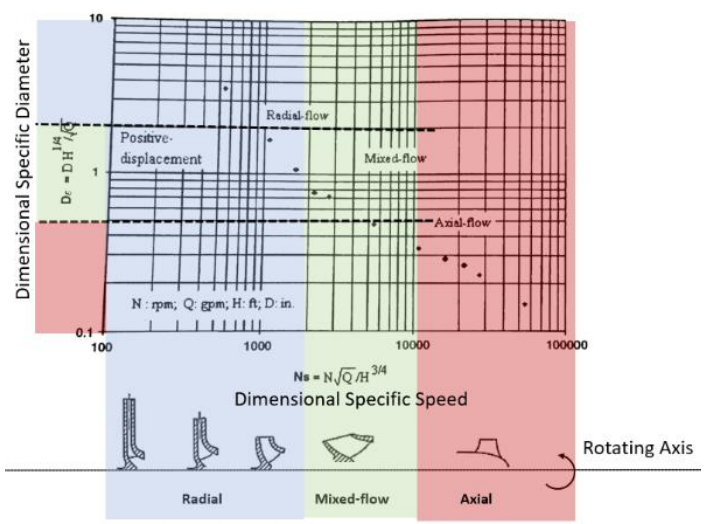

Figure 2.11 N_s and D_s correlation with impeller types.

Adapted from [31].

Analogous to the specific speed N_s; specific diameter D_s is a design factor which indicates the estimated impeller's tip diameter D_t with

$$D_s = \frac{D_t H^{1/4}}{Q^{1/2}} \tag{2.4}$$

where D_t impeller's tip diameter, *H* is head and Q is flow rate [31, 83, 86].

Unlike industrial pump design, special considerations in size, morphology and stress regions should be made when designing a long-term LVAD because the size of the pump is constrained to fit in the chest cavity; the morphology of the blades of the impeller should reduce as much as possible the viscous effect of boundary layers; and because the high shear regions should be kept as small as possible due to the natural biological response of blood, which can lead to undesired hemolysis and thrombosis [6].

Because the Cordier diagram does not provide information regarding the impeller's blade morphology [87], blade profile, angles, number of blades, and many other design parameters are defined after having selected a proper impeller type (radial/centrifugal, mixed or axial).

Since the focus of this study is only given to an axial pump configuration, the impeller design overview is limited to this configuration.

Axial-flow Impeller Design

Flow velocity within an impeller, independent of its configuration, can be decomposed into axial V_a, radial V_r,and tangential V_u velocities using the cylindrical coordinates (r,θ,z).

In an axial-flow impeller, flow velocity is mostly axial V_a and tangential V_u, because the impeller has a constant diameter along the flow path and there is no radial velocity V_r change from the inlet (1) to the outlet (2) portions of the impeller, as shown in figure 2.14 [31]. This means that the tangential velocity U_m due to the impeller rotation at the mean radius r_m remains the same in the inlet (1) and outlet (2) sections of the impeller:

$$U_m = U_1 = U_2 = r_m \omega, \tag{2.5}$$

where ω is the angular speed in rad/s.

Mean radius r_m refers to the section on the blade in which the flow analysis is performed and is usually expressed as

$$r_m = \sqrt{\frac{r_t + r_h}{2}}, \tag{2.6}$$

where r_t is the impeller tip radius and r_h is the impeller hub radius (Fig 2.14).

Similarly, in axial impellers, the axial velocity V_a at the inlet V_{a1} and outlet V_{a2} of the pump remains the same and its described in Eq. 2.7

$$V_{a1} = V_{a2} = V_m = \frac{Q}{A}, \tag{2.7}$$

where V_m is the meridional axial component of the flow velocity, Q flow rate, and A is the cross-sectional area for flow described as

$$\text{A}=A_1=A_2=\pi(r_t^2 - r_h^2), \tag{2.8}$$

where A_1 and A_2 are the cross-sectional area for flow at the inlet and outlet of the impeller respectively, and r_t and r_h are the impeller tip and hub radius, respectively (Fig. 2.13).

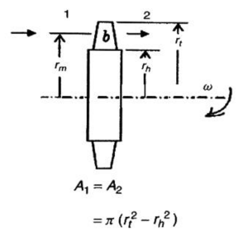

Figure 2.12 Axial impeller configuration (Meridional view).

Reprinted with permission from [31].

Applying Euler's pump equation to a point on an axial impeller blade and assuming no losses we get

$$g\Delta H = U_2 V_{u_2} - U_1 V_{u_1}, \tag{2.9}$$

where g is the gravitational acceleration, ΔH is the head rise, U_1 and U_2 are linear velocities of the impeller inlet and outlet, respectively and V_{u_1} and V_{u_2} are the tangential velocities of the fluid at the impeller inlet and outlet, respectively.

Now, assuming no radial change on the axial impeller, the equation gets simplified to

$$g\Delta H = U_m V_{u_2}, \tag{2.10}$$

where g is the gravitational acceleration, ΔH is the head rise, U_m is the tangential velocity of the fluid due to the impeller rotation in the mean radius and V_{u_2} is the average absolute flow velocity at the outlet (2) section of the impeller.

Figure 2.14 shows the basic dimensions for an axial impeller definition viewed from a meridional (left), top (medium), and front (right) sections where D_t is the impeller tip diameter, r_t is the impeller tip radius, D_h is the impeller hub diameter r_h is the impeller hub radius, D_m is the mean diameter, r_m is the mean radius, b is the blade radial length extension and s is the pitch.

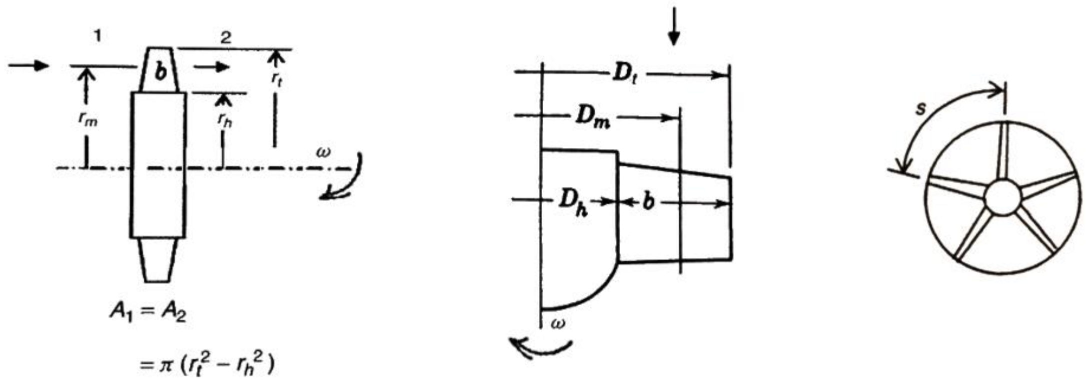

Figure 2.13 Basic dimensions of an axial-flow impeller.
Meridional, top and front views. Reprinted with permission from [31].

The impeller tip diameter D_t and impeller mean radius r_m are defined using Eq 2.4 and 2.6, respectively.

[83] and [31] explain that, as part of the design procedure, the hub-tip ratio ν, the number of blades Z_b, vane thickness, the turning angle of the blades, and the casing are experimental factors. Meaning that these factors are designed using graphical correlations upon experimental validation [31, 81, 83].

Figure 2.15 shows two graphical correlations widely used to define experimental design factors of axial pumps such as the hub-ratio ν (thus, the impeller hub diameter), the number of blades (vanes) Z_b as a factor of ν

$$Z_b = \frac{6\nu}{1-\nu} \tag{2.11}$$

the pitch s using Z_b

$$s = \frac{2\pi r_m}{Z_b} \tag{2.12}$$

and the chord/pitch ratio $\frac{c}{s}$ (also known as solidity)

$$\frac{c}{s} = \frac{10}{(\frac{D_h}{D_t})(\frac{N_s}{1000})^{0.5}} \tag{2.13}$$

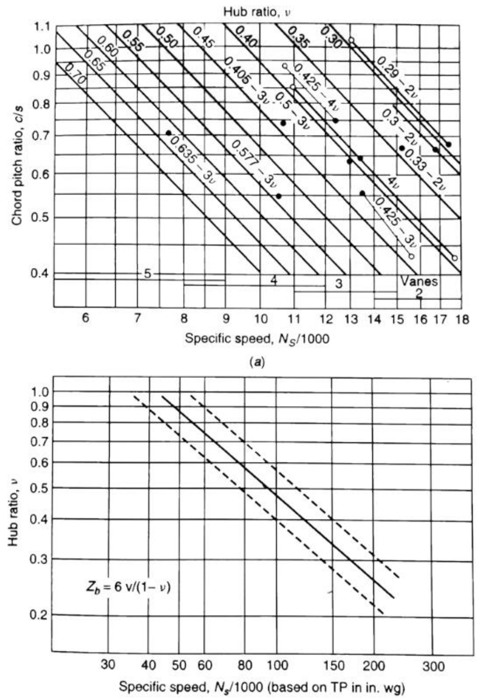

Figure 2.14 Hub-tip ratio, blade number and chord pitch ratio for axial-flow pump
Reprinted with permission from [31].

Solidity $\frac{c}{s}$, refers to the ratio of the blade chord length c and the width spacing between blades, known as pitch s [31].

According to [31, 43] and [83], there are two types of methods used to design the blade profile and angles of an axial impeller. One related to the lift and drag forces over an isolated airfoil and the cascade analysis in terms of fluid deflection and pressure loss at the mean blade line. Because the second approach is widely used in the literature for LVAD design, further details are given below [6, 18, 43, 85].

Blade profile definition through cascade analysis is done using the velocity triangle analysis. The velocity triangle is a symbolic representation of the flow velocity, where the tangential velocity U due to the impeller rotation, the relative flow velocity with respect to the impeller W, and the absolute velocity V of the fluid V= U+W are considered [31].

Figure 2.16 shows the velocity triangle diagram at the inlet (1) and outlet (2) sections of an axial impeller from a cross section of the blade; where V_{a1} and V_{a2}, are the axial velocities at the inlet and outlet of the impeller, respectively, V_{u_2} is the tangential component of the fluid velocity, U_1 and U_2 are the tangential blade velocities, W_1 and W_2 are the relative velocities, β_1 and β_2 are the inlet and outlet relative angles, α_2 is the inlet angle of the diffuser vane, and C is the chord length.

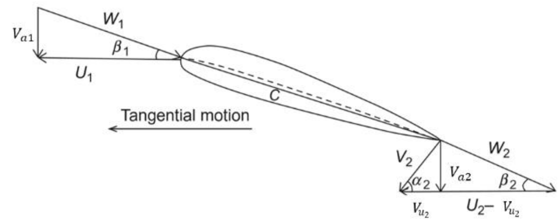

Figure 2.15 Velocity diagram for axial-pump.

Reprinted with permission from [31]

With figure 2.17, applying trigonometry rules, and recalling the tangential velocity at the mean radius U_m and the axial velocities $V_{a1}, V_{a2}$from Eq. 2.5 and Eq. 2.7, respectively; the tangential components of the fluid velocity are defined as:

$$V_{u_1} = V_{a1} \cot \alpha_1 \tag{2.14}$$

$$V_{u_2} = U_m - V_{a2} \cot \beta_2 \tag{2.15}$$

where V_{a1} and V_{a2} are the axial velocity components of the fluid velocity at the inlet and outlet, respectively; α_1 is the angle between the tangential velocity component and the fluid velocity; β_2 is the outlet angle of the impeller measured from the axial direction; and U_m is the tangential velocity due to the impeller rotation at the mean radius .

Therefore, the head estimation in axial impeller based on the inlet and outlet angles can be written as

$$g\Delta H = {V_m}^2 \cot \beta_1 (\cot \beta_1 - \cot \beta_2) \tag{2.16}$$

Where V_m is the meridional axial component of the flow velocity.

Figure 2.17 shows other relevant blade design parameters derived from blade-mean analysis, but for simplicity purposes, their analysis will not be discussed.

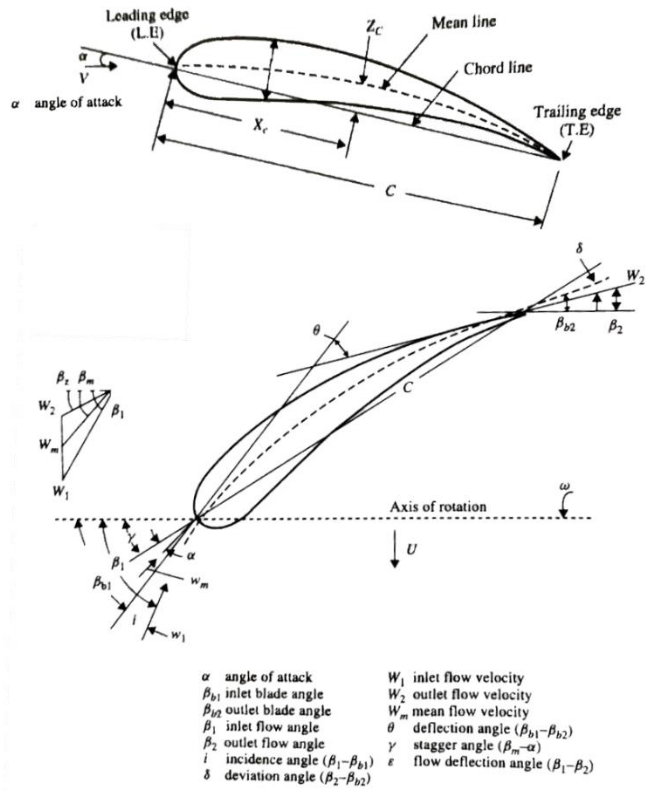

Figure 2.16 Blade geometrical parameters for an axial pump.
Reprinted with permission from [31].

Since blade design for LVAD impellers can turn into a very complex and time-consuming process [43, 88], automated design software is used to ease the pump geometry design definition through the use of turbomachine design theory and empirical correlations [89].

Although theoretical turbomachinery design provides preliminary performance outcomes based on the theoretical desired operating point of the pump, the real operating point is determined through experiments [82]. Therefore, the following subsection aims to describe how LVAD performance is quantified and explain the testing approaches used in the literature [45, 48, 49, 85, 90-98].

2.4.2 Performance Analysis

LVAD performance is expressed in terms of pressure rise ΔP (Pa or mmHg) or head H (m), against volumetric flow rate Q ($\mathrm{m^3\ s^{-1}}$ or $\mathrm{L\ min^{-1}}$) or mass flow rate $\dot{m}$ ($\mathrm{kg\ s^{-1}}$) at a fixed rotating speed N (rad s^{-1} or RPM) and for a constrained impeller diameter D (m). A list of units conversion is included in Appendix E.

A common performance representation enables the visualization of pressure rise or head produced at any point over the capacity range. This representation is known as the head-capacity (HQ) curve [31] in which pressure rise, or head decrease as the flow rate increases [82].

Hydraulic efficiency η (%) is also as a performance predictor since power consumption becomes a crucial parameter when defining requirements of the external power supply.

Hydraulic efficiency quantifies the amount of useful energy P_o or hydraulic power P_h (watts) from the total amount input energy P_i or mechanical power P_m (watts):

$$\eta = \frac{P_o}{P_i}\ x\ 100\ (\%) = \frac{P_h}{P_m}\ x\ 100\ (\%) = \frac{Q\ \Delta P}{N\ \tau}\ x\ 100\ (\%) \qquad (2.17)$$

where Q is the flow rate of the pump, ΔP is the pressure rise across the pump, N is the rotating speed of the pump, and τ is the torque of the motor (Nm).

HQ curve and hydraulic efficiency are known as the performance curves of pumps and are usually plotted in the dependent axis, while the flow rate is placed in the independent axis. Figure 2.18 shows a generic HQ curve for each pump configuration (i.e. radial, axial, mixed) and the typical hydraulic efficiency curve. In LVAD testing, flow rate, also known as capacity range, is usually explored from 0.1 $m^3 s^{-1}$ to 1.66 $x\ 10^{-4}\ m^3 s^{-1}$ and the pressure rise is highly dependent on the design and performance of the pump [41].

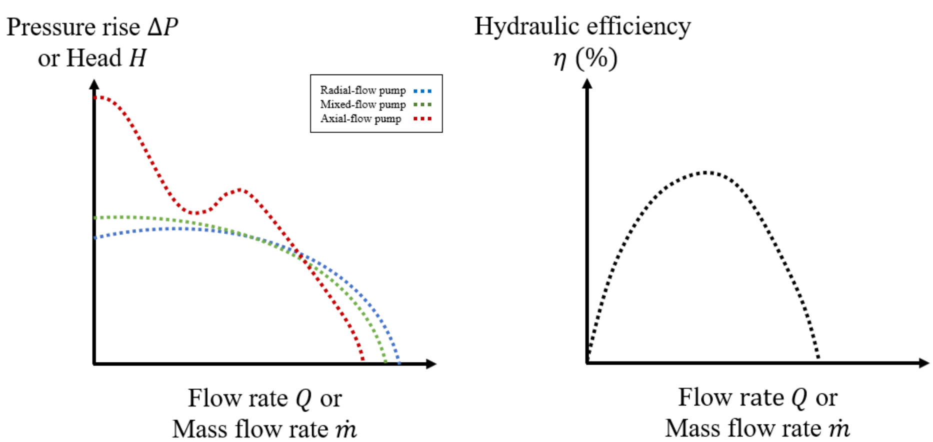

Figure 2.17 Typical HQ curve Pump (left) and hydraulic efficiency curve (right). Adapted from [31, 84].

Each pump has its own characteristic HQ curve and η curve; and the variation of curves is determined by the power, pump size, rotational speed, and geometrical shape of the impeller of the pump [80, 81].

Performance curves can be assessed through Computational Fluid Dynamic (CFD) simulations and physical experiments [45, 46, 98]

Computational Fluid Dynamic (CFD) Predictions

CFD is a numerical technique that allows the characterization of complex three-dimensional flows. The main function of a CFD analysis is to have a comprehensive virtual visualisation in the flow field of a real system.

The analysis is carried through a numerical calculation scheme in which the Navier-Stokes equations are solved with suitable boundary conditions [31, 90]. Navier-Stokes equations are basic governing equations that account for the mass and energy conservation principles of a viscous fluid [80]

Some parameters obtained through CFD simulations are the flow velocities, pressures, secondary flows, flow separation, and shear stresses of a given system.

Over the last decades, the use of CFD for medical devices development (e.g.: stents, heart valves, LVADs) has increased because the time and cost required to do numerical analysis is significantly low when compared with experimental testing [90, 99-101]. However, for blood-contacting devices, experimental evaluation is still required due to the lack of standardization in CFD validation [102, 103]. Therefore, and according to ISO 14708-5 standard [102], the use of CFD is suggested to be only limited to a design stage because of its suitability to obtain preliminary results and relative design comparisons, rather than for the evaluation of absolute quantities.

Experimental In-Vitro Testing

When the estimation of performance curves is carried through experiments, tests are conducted in a hydraulic test rig to measure flow rate, pressure rise, and power consumption [82]. Therefore, instrumentation devices with high sensitivity are recommended. Similarly, cost and complexity of use play an important role when choosing instrumentation devices.

Figure 2.19 shows the hydraulic schematic of standard test rig configuration used in LVAD testing. For better understanding, the flow direction is indicated with a red arrow. In general, the hydraulic setup consists of a fluid reservoir, the test pump, a tubing system, a flow control valve, and a flow directional valve. The main parameters to be measured are the flow rate, pressure rise or head, rotational speed of the impeller and input shaft torque. More details of each component are given below.

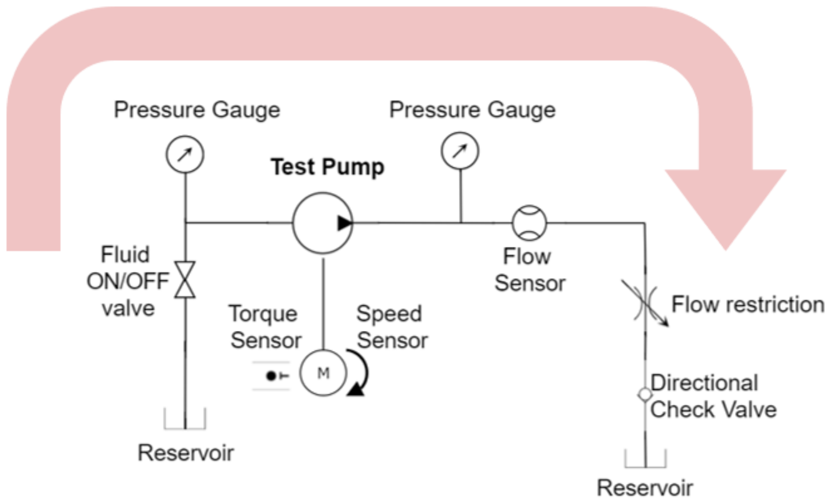

Figure 2.18 Hydraulic schematic of a test rig.

The fluid reservoir or tank stores the fluid that circulates in the loop. When temperature control is not necessary, the reservoir is open to atmospheric pressure and connected to the instrumentation devices through a tubing system. Both output and input holes of the reservoir should be placed at the same height and diameter to avoid differential offset pressure in the system.

Similarly, the use of large tubes and fittings is advisable to minimize the pressure losses and restrictions on the circuit [84].

Local pressure losses are also found in locations where the tubing bends and where valves and tubing fittings are placed. Therefore, it is important to respect the minimum allowed bending radius of the tubing, prevent tubing twisting and compound bends in more than one plane, avoid the use of rigid elbows and T-fittings to discard unnecessary stresses on the circuit, and to use tubing fittings with a gradual reduction rather than angular reduction [84, 104].

Since *laminar flows* and *turbulent flows* are expected in the system [43], both conditions are investigated when constructing a hydraulic test rig. Laminar flow refers to a flow regime in which the fluid particles move along parallel lines and do not mix, whereas turbulent flow refers to the flow regime in which flow streams are not parallel and get mixed as they move (Fig. 2.21) [84].

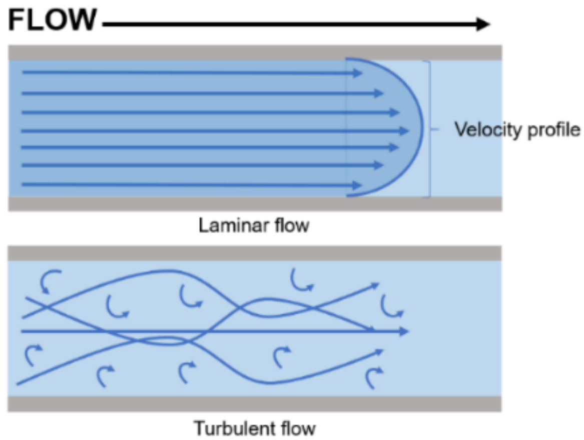

Figure 2.19 Flow regimes. Adapted from [80, 105].

The computation of the non-dimensional Reynolds Number *Re* helps determining whether the flow in a tube is laminar or turbulent in the axial direction:

$$Re = \frac{\rho\, V\, D}{\mu} \tag{2.18}$$

where V is the flow velocity (m s^{-1}), D is the tube diameter (m), ρ is density (kg m^{-3}), and μ is the dynamic viscosity of the liquid (Pa).

For *Re* below 2000, flow is considered to be laminar; for *Re* above 4000, flow is turbulent; and for *Re* ranging between 2000 to 4000, flow is considered to be transitional [106].

Because tubing fittings, curvatures, and valves affect the flow dynamics within a tube, *entrance length* and *fully developed region* should also be investigated. Entrance length refers to the distance in which the flow reaches a fully developed profile [43]. And a fully developed region is a zone where the velocity profile within a tube does not change in the fluid direction [80].

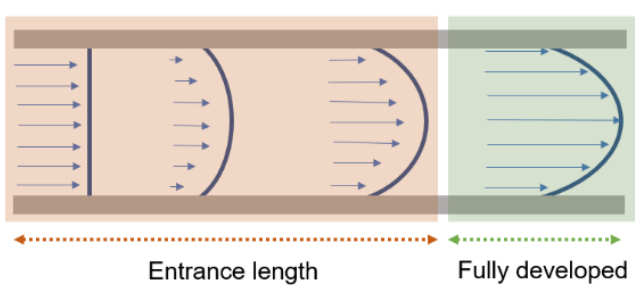

Figure 2.20 Fully developed distance of a fluid in a pipe. Adapted from [105].

According to [43], the recommended fully developed distance to consider for a laminar flow regimes is $L_{laminar} = 0.06\, Re\, d$, where d is the internal diameter of the pipe and $L_{turbulent} = 5.3\, Re^{0.12}\, d$ for a turbulent flow.

Flow rate is measured through a flow sensor. As the circuit follows a series configuration, flow can be measured at the inlet or outlet of the pump. Placing the flow sensor at the inlet becomes advantageous as undesired measurements due to the flow disturbances at the outlet of the pump are not accounted.

Ultrasonic flow probes are the most common type of flow sensors used in LVAD testing. [45, 49, 54, 74]. A significant advantage of this technology is that the device does not come in contact with the fluid. Its principle of operation (Fig. 2.23) relies on the transmission of ultrasonic waves in either upstream or downstream direction through a pair of transducers located at different distances [107].

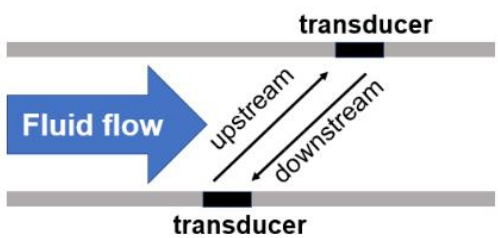

Figure 2.21 Ultrasonic flow probe principle.

Pressure rise or head through the pump is usually measured with two individual piezoelectric/diaphragm pressure transducers placed at the inlet and outlet of the pump [41, 108], or with a differential pressure transducer [109]. For these types of sensors, data acquisition must be employed. The electrical output signal of the pressure transducers and the flow probe might drift with time and the output signal might be affected, therefore, initial calibration runs should be performed, prior experiments, to verify the zero values.

The rotating speed and input shaft torque are used to compute the input mechanical power required to drive the pump. These parameters can be quantified using a tachometer and a dynamic rotary torque sensor, respectively, or with a dynamometer. Alternatively, input power consumption can be also computed by means of the electrical input power, nevertheless this approach also accounts for the electrical and mechanical looses of the system [6].

An electrical motor is also an essential component in the pump as its main function is to drive the impeller. Within the literature, brushed DC motors [85] and more commonly, brushless DC motors [45, 74, 95] are used for LVAD testing. For a proper motor selection, pump designers should consider the desired operating speed N at which the pump will be running during experiments, hence should have an estimated power consumption range. Because the rotating speed may fluctuate during experiments, electronic speed control components are important.

A flow control valve is an essential component in the circuit as it creates fluid resistance to allow the pump to run over its full performance range [82]. Several types of valves could be used to this end; such as the globe valves, diaphragm valves, ball valves, pinch valves, butterfly valves, and throttling valves. The flow restriction valve is usually placed close to the inlet of the reservoir (i.e. last section of the hydraulic test rig), to bypass flow recirculation measurements.

Before running tests, the hydraulic system must be primed. Priming is the start up process in which the test pump and the tubing system of the hydraulic test-rig are filled with fluid to allow a proper suction in the circuit [84]. The placement of a directional valve at the beginning of the suction line and the temporary use of a peristaltic pump is one of the easiest and least expensive approach for priming.

Similarly, the motor settling time should be respected. It refers to the time that the pump needs to reach from zero its nominal rotating speed N [84]. Before reaching the desired rotating speed N, no measurements should be taken but the rotational speed and torque.

Once the pump has reached the desired rotating speed N, the testing procedure [82] goes as follows: The flow restriction valve is set to a fully open position (i.e.: highest flow rate discharge point). Then the fluid must circulate for a few minutes below atmospheric pressure to purge air bubbles trapped in the tubing system (priming). Then, the flow rate and pressure measurements start being recorded along with the already registered torque and rotational speed. Next, the flow restriction valve is tightened to reduce the flow rate to acquire a new data point. And the previous step is usually repeated until the restriction gets closer to the fully closed position to run the pump over its full performance range. Lastly, the data is plotted to get the performance curves (HQ and η curves).

The testing procedure can be repeated for the acquisition of a group of curves, the using either: a different rotating speed *N* with the same impeller or a scaled model of the impeller at the same rotating speed *N* [82].

2.4.3 Design Optimization Process

After experimental performance curves are evaluated, the pump optimization process can be done using the dimensional analysis.

Dimensional analysis is a problem-solving technique aimed to reduce the number of parameters involved in a physical phenomenon into a certain number of non-dimensional parameters through the use of the Buckingham pi-Theorem [31]. The Buckingham pi-theorem states the number of non-dimensional parameters $(\pi_1, \pi_2, \pi_2 \dots \pi_n)$ needed to correlate dimensional variables of a system through a rigorous dimensions-based procedure. Details about the theorem can be explored in [31] Chapter 2.

Dimensional analysis becomes an advantageous tool for pump designers because experimental results of a pump model can be easily correlated to non-dimensional parameters to create performance predictions of scaled up or down prototypes [31, 81].

The non-dimensional parameters used for performance predictions are the head coefficient ψ, the flow coefficient Φ, the Reynolds Number *Re*, and the power coefficient Π [31].

$$\psi = \frac{\Delta p}{\rho D^2 N^2} \tag{2.19}$$

$$\Phi = \frac{Q}{D^3 N} \tag{2.20}$$

$$Re = \frac{\rho D^2 N}{\mu} \tag{2.21}$$

$$\Pi = \frac{P_s}{\rho D^5 N^3} \tag{2.22}$$

Where ΔP is the pressure rise ρ is the fluid density, D is the diameter of the impeller, N is the rotating speed, Q is flow rate, μ is the fluid viscosity, and P_s is the shaft power.

When experimental performance curves are plotted in terms of these non dimensional parameters (Fig. 2.24) and the same fluid circulates through the hydraulic loop, the curves can predict the behaviour of the same model rotating at different speeds or the behaviour of a “geometrically similar” prototype rotating at the same speed as the tested model.

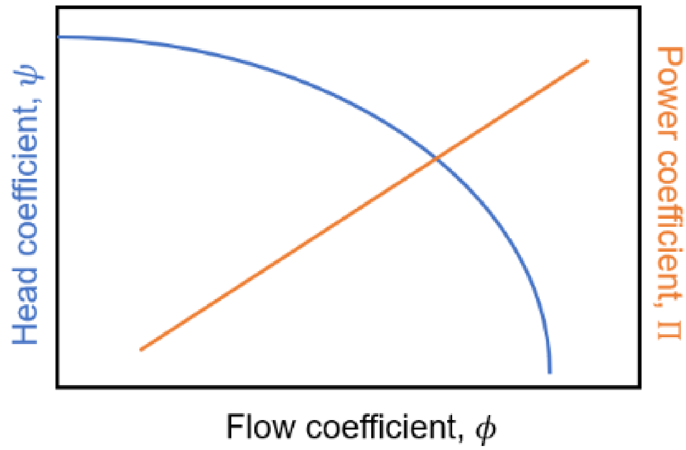

Figure 2.22 Performance curves in terms of non-dimensional parameters. Adapted from [31].

Geometric similarity implies that all linear and angular dimensions between the model and the prototype are in constant proportion (Fig. 2.25).

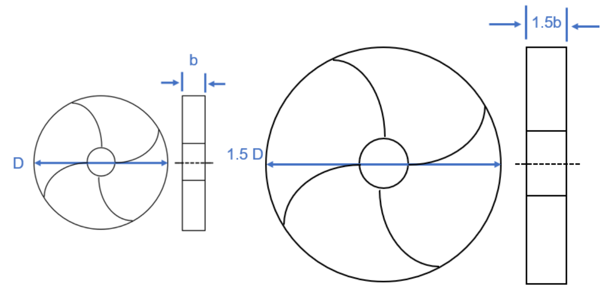

Figure 2.23 Geometric similarity between a tested model and scaled-up prototype. Adapted from [31].

The operating relations between a pump model m, and a geometrically similar prototype p are known as similarity or affinity laws and are expressed as:

$$\psi_m = \psi_p \ or \ \frac{\Delta p_m}{(D_m N_m)^2} = \frac{\Delta p_p}{(D_p N_p)^2} \tag{2.23}$$

$$\Phi_m = \Phi_p \ or \ \frac{Q_m}{{D_m}^3 N_m} = \frac{Q_p}{{D_p}^3 N_p} \tag{2.24}$$

$$\Pi_m = \Pi_p \ or \ \frac{P_{sm}}{\rho_m {D_m}^5 {N_m}^3} = \frac{P_{sp}}{\rho_p {D_p}^5 {N_p}^3} \tag{2.25}$$

CHAPTER 3: MATERIALS AND METHODS

3.1 Geometry Definition

This section presents an overview of the methods and resources used to define the detailed 'hubless' blood pump geometry, followed by an introduction of two design variations.

Pump design is a complex process that involves empirical graphical correlations and a variety of mathematical equations.

The detailed ‘hubless’ geometry was created using CF Turbo (CF Turbo 10.3.5, Dresden, Germany), a modern and interactive pump design software. CF Turbo combines fundamental turbomachinery equations and empirical correlations to start geometries from scratch, or to redesign geometries for adaption or optimization. Similar to conventional pump design, the first step is the definition of the fluid properties and the design operating point (DOP) of the pump in terms of total pressure difference, flow rate and rotational speed. Figure 3.1 shows the Global Setup window where the variables are defined.

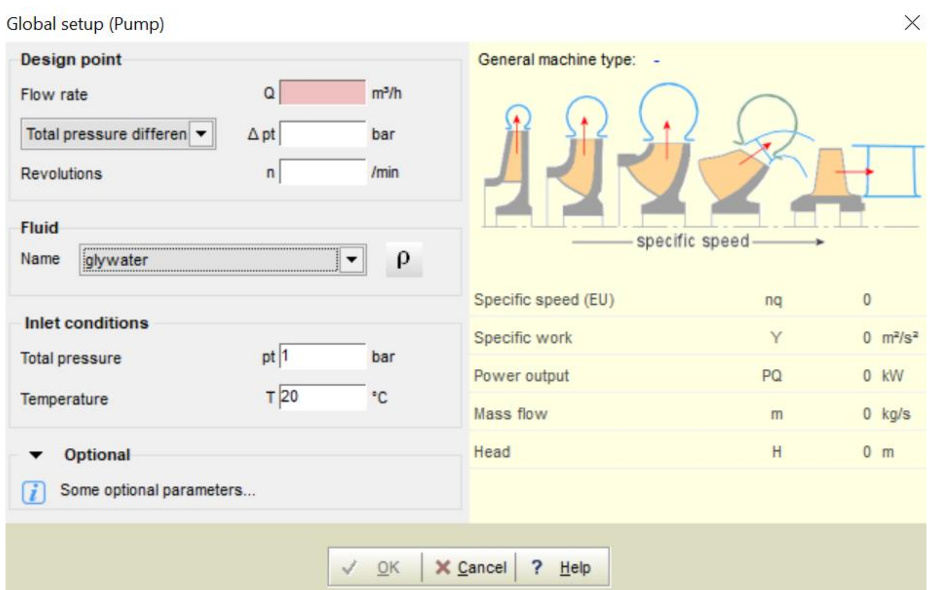

Figure 3.1 Global setup window for pump design in CF Turbo software.

Taking blood as a reference, fluid density and dynamic viscosity were defined as 1060 kg m^{-3} and 3.5 x 10^{-3} Pa s, respectively, and the design operating point (DOP) was set to $\Delta P =$

6.666×10^3 Pa (50 mmHg), $Q = 5 \times 10^{-5}$ m s^{-3} (3 L min^{-1}), and $N = 335.1$ rad s^{-1} (3200 RPM).

The main dimensions of the pump were estimated through the software using the non-dimensional head ψ and flow Φ coefficients and respecting the anatomical dimensions of the aorta, potential placement location of the pump. The external diameter OD of the pump resulted in $2.5\ x\ 10^{-2}$ m, the hollow hub diameter *ID* in $1.1\ x\ 10^{-2}$ m, and the total axial extension *Z* of the pump in $8.2\ x\ 10^{-2}$ m. The axial extensions of the inducer, impeller, and diffuser are listed in table 3.1

Table 3. 1 Axial extensions of the inducer, impeller and diffuser portions of the pump

Part	Axial extension *Z*	Units
Inducer (stator)	$2.0\ x\ 10^{-2}$	m
Impeller (rotor)	$3.0\ x\ 10^{-2}$	m
Diffuser (stator)	$3.2\ x\ 10^{-2}$	m

Due to the nature of the unconventional concept, the blades were fixed to the outer circumference of the pump and no clearance gap between the impeller and the casing of the pump was incorporated.

Using CF Turbo, a total of 18 independent blade parameters in each section of the pump (i.e.: inducer, impeller, and diffuser) can be defined, resulting in an infinite number of possible combinations and pump operating points, when one parameter is changed at a time. Hence, a blade parametric study was performed to predict the best theoretical performance of the pump in terms of efficiency and head pressure. Table 3.2 lists the resultant input values for blade parameters for each section of the pump.

Table 3.2 Blade input parameters for each section of the pump

Part	Blade Parameter	Symbol	Value	Units
Inducer (stator)	Tip clearance inlet	*xIn*	0.0001	m
	Tip clearance outlet	*Xout*	0.0001	m
	Axial extension	*Z*	0.02	m
	Blade radial extension	*R*	.007	m
	Number of blades	*Zb*	4	-
	Number of spans	*y*	2	-

	Thickness LE @hub	*sLEH*	0.002	m
	Thickness LE @shroud	*sLES*	0.002	m
	Thickness TE @hub	*sTEH*	0.001	m
	Thickness TE @shroud	*sTES*	0.001	m
	Blade angle LE	αBLE	90	°
	Blade angle TE	αBTE	90	°
	Meanline LE position (hub)	ϕLE	0	°
	Meanline TE position (hub)	ϕTE	0	°
	Wrap angle (hub)	ϕ	0	°
	Meanline LE position (shroud)	ϕLE	0	°
	Meanline TE position (shroud)	ϕTE	0	°
	Wrap angle (shroud)	ϕ	0	°
Impeller (rotor)	Tip clearance inlet	*xIn*	0.0001	m
	Tip clearance outlet	*Xout*	0.0001	m
	Axial extension	*Z*	0.03	m
	Blade radial extension	*R*	0.007	m
	Number of blades	*Zb*	3	-
	Number of spans	*y*	2	-
	Thickness LE @hub	*sLEH*	0.002	m
	Thickness LE @shroud	*sLES*	0.002	m
	Thickness TE @hub	*sTEH*	0.0001	m
	Thickness TE @shroud	*sTES*	0.0001	m
	Blade angle LE [hub, shroud]	$\beta B1$	[15.0, 15.0]	°
	Blade angle TE [hub, shroud]	$\beta B2$	[12.8, 6.0]	°
	Meanline LE position (hub)	ϕLE	15	°
	Meanline TE position (hub)	ϕTE	250	°
	Wrap angle (hub)	ϕ	235	°
	Meanline LE position (shroud)	ϕLE	25	°
	Meanline TE position (shroud)	ϕTE	250	°
	Wrap angle (shroud)	ϕ	225	°
Diffuser (stator)	Tip clearance inlet	*xIn*	0.0001	m
	Tip clearance outlet	*Xout*	0.0001	m
	Axial extension	*Z*	0.032	m
	Blade radial extension	*R*	0.007	m
	Number of blades	*Zb*	5	-
	Number of spans	*y*	2	-
	Thickness LE @hub	*sLEH*	0.001	m
	Thickness LE @shroud	*sLES*	0.001	m
	Thickness TE @hub	*sTEH*	0.002	m

	Thickness TE @shroud	*sTES*	0.002	m
	Blade angle LE	αBLE	5	°
	Blade angle TE	αBTE	150	°
	Meanline LE position (hub)	ϕLE	5	°
	Meanline TE position (hub)	ϕTE	150	°
	Wrap angle (hub)	ϕ	80	°
	Meanline LE position (shroud)	ϕLE	5	°
	Meanline TE position (shroud)	ϕTE	150	°
	Wrap angle (shroud)	ϕ	80	°

Overall, the inducer was designed with 4 blades parallel to the flow axis (i.e.: blade angle in the leading edge *LE* and trailing edge *TE* of 90°). The impeller had 3 curved blades with a wrap angle ϕ of 235° and 225° at the hub and shroud sections of the pump, respectively. And the diffuser had 5 blades with a wrap angle ϕ of 80° at the hub and shroud sections of the pump. The meridional view of the 'hubless' configuration is shown in figure 3.2, and figure 3.3 illustrates the 3D view of the design of the blades.

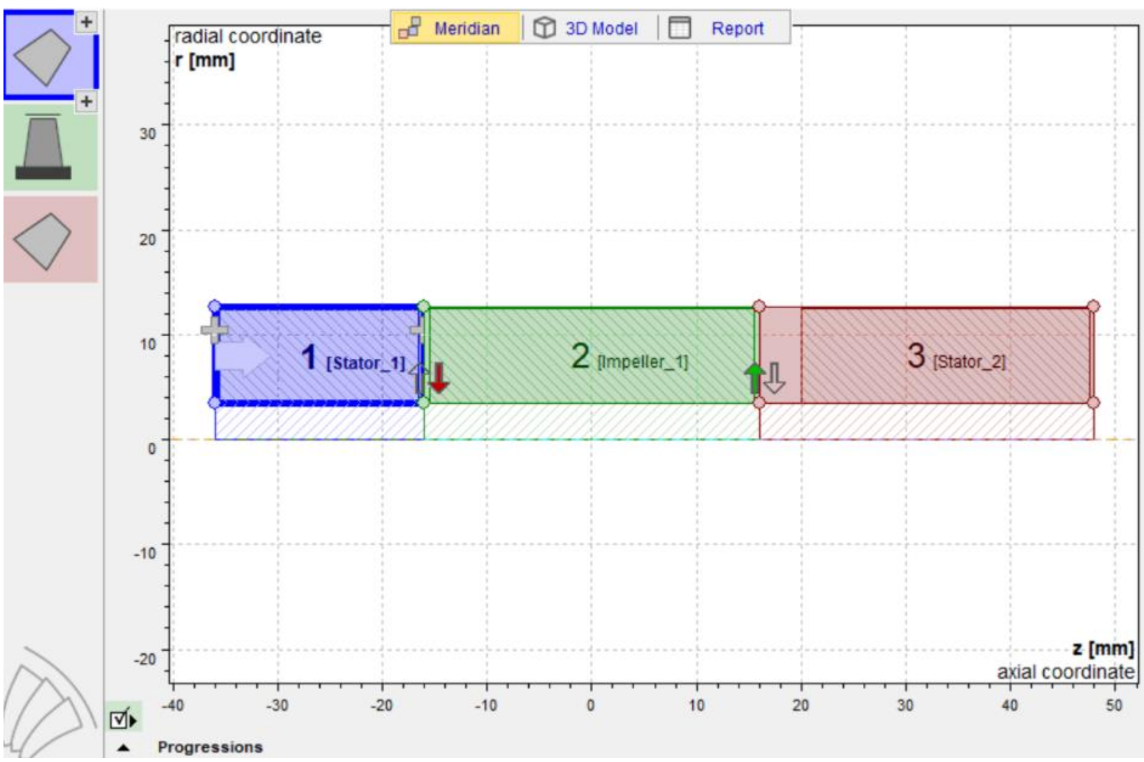

Figure 3.2 Meridional view of the axial-pump.

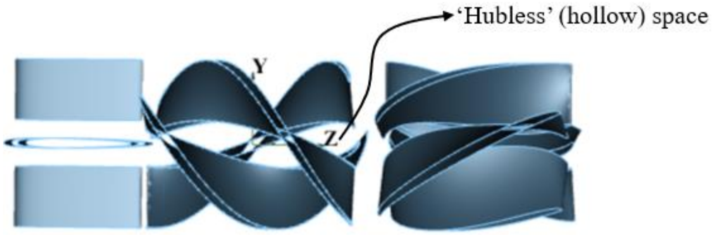

Figure 3.3 3D view of the 'hubless' blade design.

Keeping in mind that each blade design parameter affects the theoretical pump performance estimation, an alternative geometry (Design B) was created to evaluate the impact of having a different percentage of flow guided by the blades. Therefore, the initial blade radial extension b perpendicular to the axial extension Z, b= 7×10^{-3} m (Design A) was increased to b=9×10^{-3} m, while all other blade parameters were kept constant in both designs. Figure 3.4 shows a graphical representation of the variation in b at the impeller section between the initial 'hubless' design (Design A), and the modified geometry (Design B).

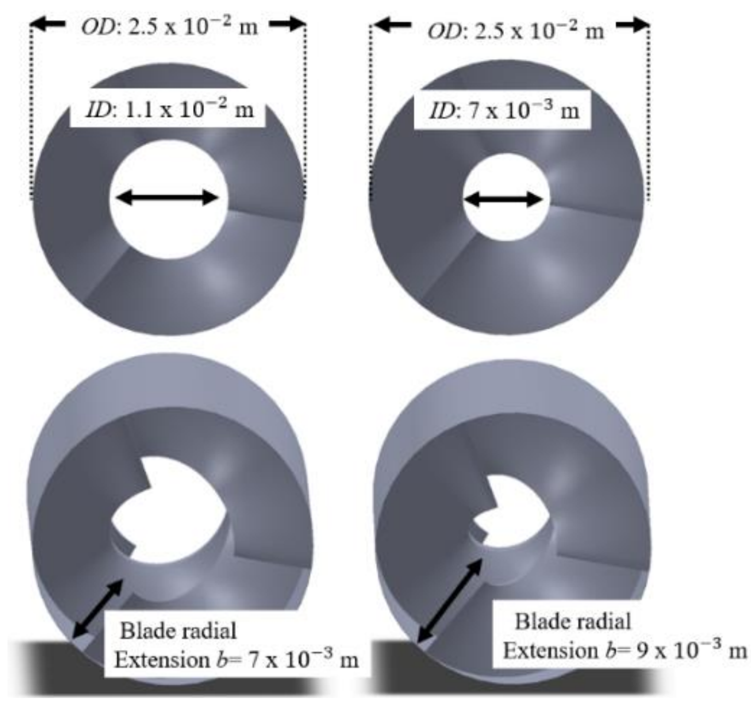

Figure 3.4 Impeller blade radial extension *b*.

Comparison between Design A and Design B.

Table 3.3 shows the percentage of the flow cross sectional area guided and non-guided by the blades in Design A and Design B.

Table 3.3 Percentage of flow guided by the blades in Design A and Design B.

Shroud diameter *OD* (m)	Outer Area (m^2)	Blade radial extension *b* (m)	Hollow Hub diameter *ID* (m)	Inner hollow Area (m^2)	% of the total flow non-guided by the blades	% of the total flow guided by the blades
0.025 m	$0.000490\ \mathrm{m}^2$	0.007 m (Design A)	0.011 m	$0.000095\ \mathrm{m}^2$	19.36 %	80.64 %
		0.009 m (Design B)	0.007 m	$0.0000385\ \mathrm{m}^2$	7.84 %	92.16 %

3.2 Computational Fluid Dynamic (CFD) simulations

This section provides detailed information of the CFD model. Fluid domain extraction, meshing process, and the boundary conditions definition for the virtual assessment of the performance curves.

Numerical simulations of Design A and Design B were carried out to quantify pressure rise, flow rate, wall shear stress regions, and Reynolds number at different rotating speeds.

3.2.1 Geometry Definition

The geometries of Design A and Design B were imported into ANSYS CFX (ANSYS Inc., Pennsylvania, USA) and simplified to facilitate convergency and accuracy of the numerical model.

The fluid domain (i.e.: the fluid bounded by the walls of the pump) was extracted using the 'Bolean Substract' tool of Design Modeler and two extra cylindrical sections were added on the extremes of the inducer and diffuser to ease the numerical solver since complicated internal flows are expected in the numerical model. Figure 3.5 shows an illustration of the steps for the fluid domain extraction of Design A.

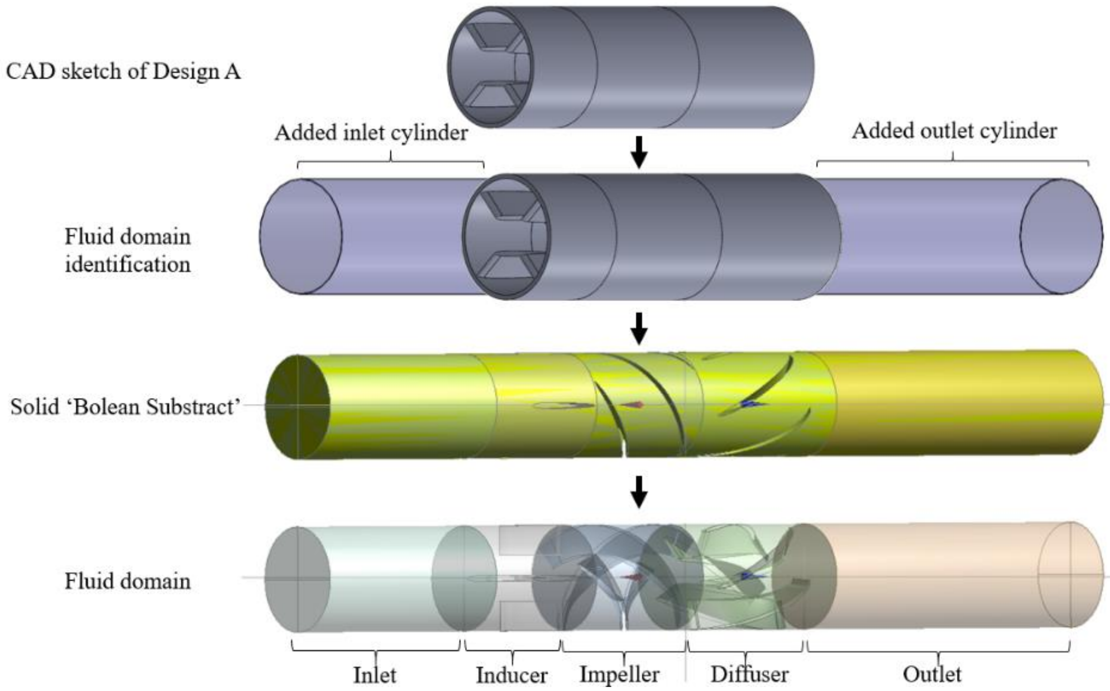

Figure 3.5 Geometrical adequation of Design A for simulations.

Because two extra cylindrical sections were added at the inlet and outlet of the pump, the fluid domain was divided in 5 parts: inlet, inducer, impeller, diffuser, and outlet.

3.2.2 Mesh

Each fluid domain was meshed separately using ANSYS Workbench Meshing tool and a conformal mesh was applied to match nodes at the interface of each part. This approach makes the solver computation faster and more accurate.

The first and the last domains were meshed using a 'MultiZone' hexahedral/prism method, while the three middle domains were meshed using a 'Patch Conforming Method' composed of tetrahedral elements.

Figure 3.6 illustrates the structured grid applied on the edges of the blades (top left), the conformal interface connection between tetrahedral and hexahedral elements of the diffuser and outlet sections, respectively (top right), and the side view of the final conformal mesh (bottom) used in the simulations.

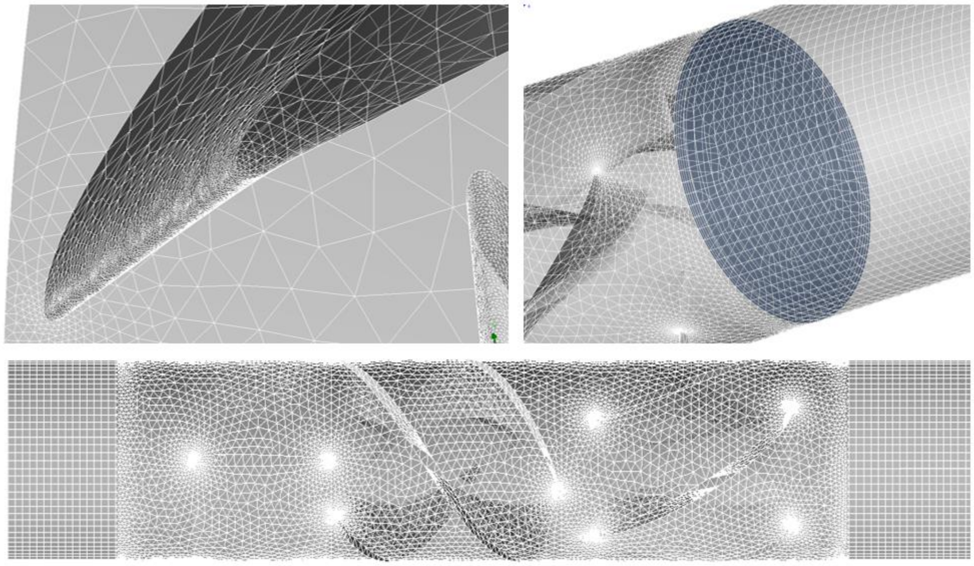

Figure 3.6 Conformal mesh used for CFD simulations.

A 'First layer thickness' inflation of $2.5\ x\ 10^{-4}$m with a maximum of 5 layers was also applied to the geometry with a growth rate of 1.1. Inflation captures the boundary layer effects close to the wall and helps to better resolve flow physic detachments near the wall [6]. Figure 3.7 shows the front and side section views of the inflation layer applied on the walls of Design A and Design B.

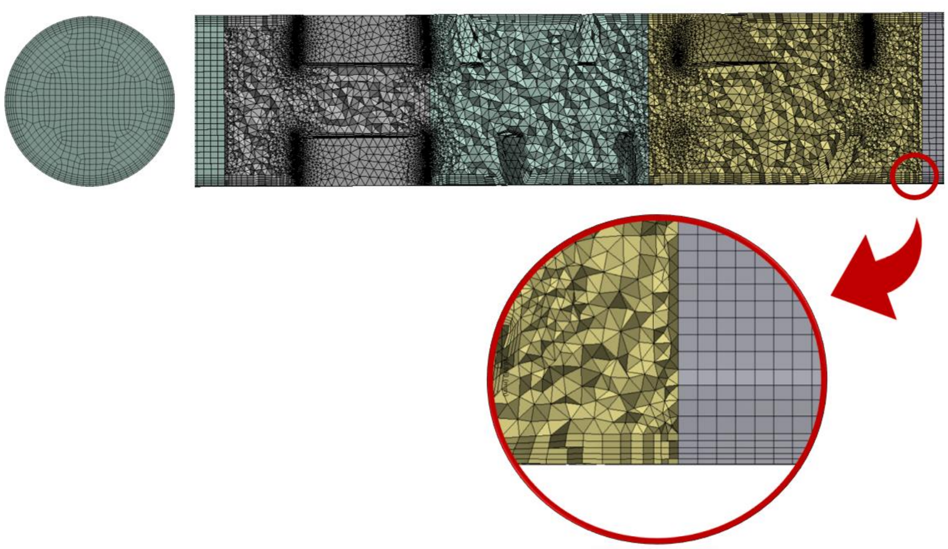

Figure 3.7 Inflation layer. Fluid domain front (left) and side (right) views.

The mesh was iteratively modified until acceptable metric controls in terms of Aspect Ratio, Skewness, and Orthogonal Quality were achieved. More details about the mesh quality are provided in Appendix A.

The resultant mesh of Design A contained 2,556,636 elements and 771,911 nodes with maximum and minimum face sizes of $5\,x\,10^{-3}$ m and $5\,x\,10^{-5}$ m, respectively. Mesh information of Design A and Design B is shown in Table 3.4.

Table 3.4 Mesh information for CFD simulations of Design A and Design

	Design A		Design B	
Domain	Nodes	Elements	Nodes	Elements
Inlet	48,399	45,400	48,399	45,400
Inducer	190,521	704,486	227,381	836,546
Impeller	167,690	621,158	203,831	752,864
Diffuser	289,381	1,113,860	352,381	1,354,843
Outlet	75,920	71,732	75,920	71,732
All domains	771,911	2,556,636	897,011	3,061,385

3.2.3 Simulation Setup

Reynolds averaged Navier-Stokes (RANS) equations were solved using a shear-stress transport (SST) turbulent model; this turbulent model has been widely used in rotary pumps CFD simulations [46, 90, 110, 111]. Numerical simulations were performed in two stages. First, 3D steady-state runs were carried out on a fully stationary fluid domain and the result of this stage was used to initialize transient runs. The second stage were the transient runs, and the results of this stage were used to acquire data points in order to recreate the performance curves. Steady-state runs provided numerical stability and facilitated convergency of the transient runs, while the transient runs, demonstrated the flow dynamics of the operation of the pump.

Blood was modeled as an incompressible Newtonian fluid with a constant viscosity of $3.5\,x\,10^{-3}$ Pa s and an average constant density of 1060 kg m^{-3}. No specific heat was defined in the model since heat transfer and friction analysis are beyond the scope of this study.

Mass flow rate $\dot{m}$ and a zero reference static pressure were specified as inlet and outlet boundary conditions, respectively. The performance curves were obtained for flow rates from $1.66 \text{ x } 10^{-6}$ m^3 s^{-1} to $1.16 \text{ x } 10^{-4}$ m^3 s^{-1} by adjusting mass flow rate $\dot{m}$ (kg s^{-1}) inlet boundary condition as a function of ρ and Q:

$$\dot{m} = \rho\, Q \tag{3.1}$$

Table 3.5 shows all the possible inlet boundary conditions in terms of Q and $\dot{m}$, and figure 3.8 shows the location of the boundary condition as seen in the Setup Menu.

Table 3.5 Inlet boundary conditions in terms of flow rate and mass flow rate

Flow Rate Q (m^3 s^{-1})	Inlet BC Mass Flow Rate $\dot{m}$ (kg s^{-1})
$1.66\, x\, 10^{-6}$	0.001766702
$8.33\, x\, 10^{-6}$	0.00883351
$1.66\, x\, 10^{-5}$	0.01766702
$2.50\, x\, 10^{-5}$	0.02650053
$3.33\, x\, 10^{-5}$	0.03533404
$4.16\, x\, 10^{-5}$	0.04416755
$5.00\, x\, 10^{-5}$	0.05300106
$5.83\, x\, 10^{-5}$	0.06183457
$6.66\, x\, 10^{-5}$	0.07066808
$8.33\, x\, 10^{-5}$	0.0883351
$1.00\, x\, 10^{-4}$	0.10600212
$1.16\, x\, 10^{-4}$	0.12366914

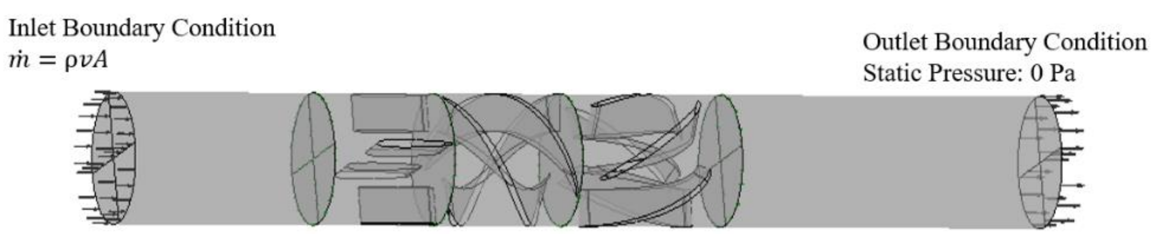

Figure 3.8 Inlet and outlet boundary conditions of the pump fluid domain.

The wall of the fluid domain was specified as 'Smooth' with 'No-Slip' condition and a 'General Connection' was applied in all simulations at the interface between domains.

The motion of fluid domains in steady-state runs was defined as 'stationary', while the fluid domain of transient runs included 'stationary' (inlet, inducer, diffuser, and outlet) and 'rotary' (impeller) motions. Figure 3.9 shows the block diagram connection between a Steady-State run and transient runs rotating at different rotating speeds.

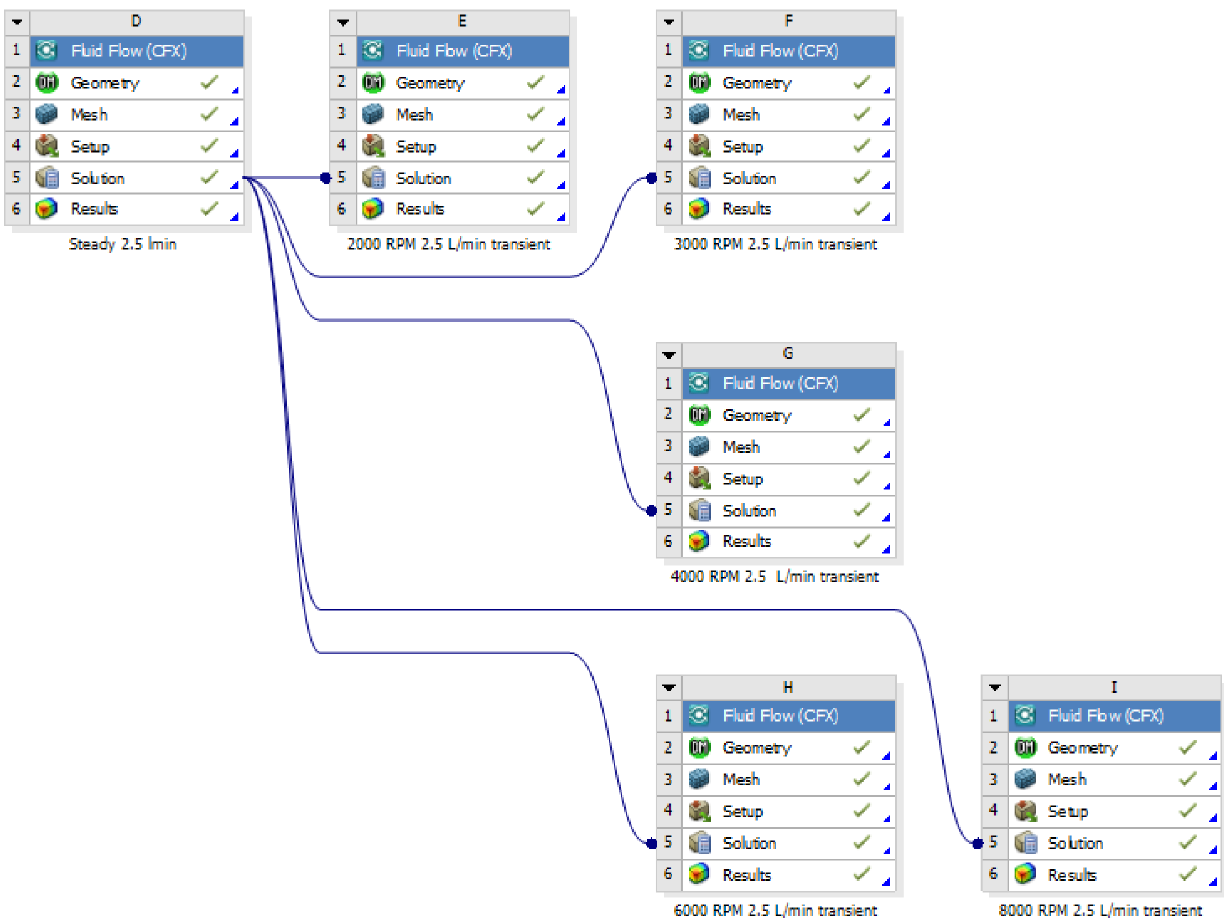

Figure 3.9 Steady-state initialization of transient runs.

Table 3.6 summarizes the input parameters and boundary conditions of steady-state and transient runs.

Table 3.6 Input parameters and boundary conditions for the simulation setup

Type	Description	Steady State	Transient
Solver	CFX Analysis type		
Material	Fluid	Blood (incompressible) Temperature: 37◦C Density: 1060 kg m^{-3} Viscosity 0.035 Pa s	Blood (incompressible) Temperature: 37◦C Density: 1060 kgm^{-3} Viscosity 0.035 Pa s
Fluid Modelling	Turbulence Scheme RANS	SST Newtonian Model	SST Newtonian Model
Boundary Conditions	Inlet Outlet Wall Domain Motion	Mass Flow Static Pressure No-slip/Smooth Wall all fluid domains: Stationary	Mass Flow Static Pressure No-slip/Smooth Wall Impeller: rotating All other: stationary
Interface	Model Frame change model Boundary Details	General Connection Stationary Conservative Interface flux	General Connection Frozen Rotor Model Conservative Interface flux
Variables	mass flow inlet BC (kg/s) Rotational Speed (rad/s)	Table 3.5 n/a	Table 3.5 209.43-335.10-418.87-628.31-837.75
Convergence criteria	RMP Convergence Control	<10^-5 250 iterations	<10^-5 total time, timestep

The transient runs were iterated for 10 revolutions with a timestep Δt every 10 degrees of rotation ($\Delta t =$time of 1 rotation (s)/36). ‘Rotating Frame of Reference’ and ‘Frozen rotor’ features were used to spin the impeller at predetermined rotating speeds of 209.43- 335.10- 418.87- 628.31 and 837.75 rad s^{-1} and to link regions between stationary and rotating frames, respectively. Additionally, scalar wall shear stresses were estimated to identify high stress regions where possible blood trauma could develop [112, 113].

3.2.4 Solution

The steady-state results were obtained after the root mean square (RMS) of the momentum and mass equations reached convergency criteria of <10^{-5}. The transient results were obtained after the total time taken to rotate the pump 10 revolutions was reached. The computational time for steady and transient runs was 1 hour and ~30 hours, respectively.

3.3 Development of the Physical Prototype

The following section outlines the materials and tools used to develop a physical prototype of the 'hubless' concept for experimental in-vitro hydraulic testing.

3.3.1 Adapted pump geometry

A hydraulic test rig and a physical 3D printed prototype of the initial 'hubless' pump (Design A) were constructed to experimentally assess the performance curves. The pump geometry was previously defined by [114] and [3] and figure 3.10 shows the 'Shaded' and 'Hidden Lines' drawings of the pump geometry.

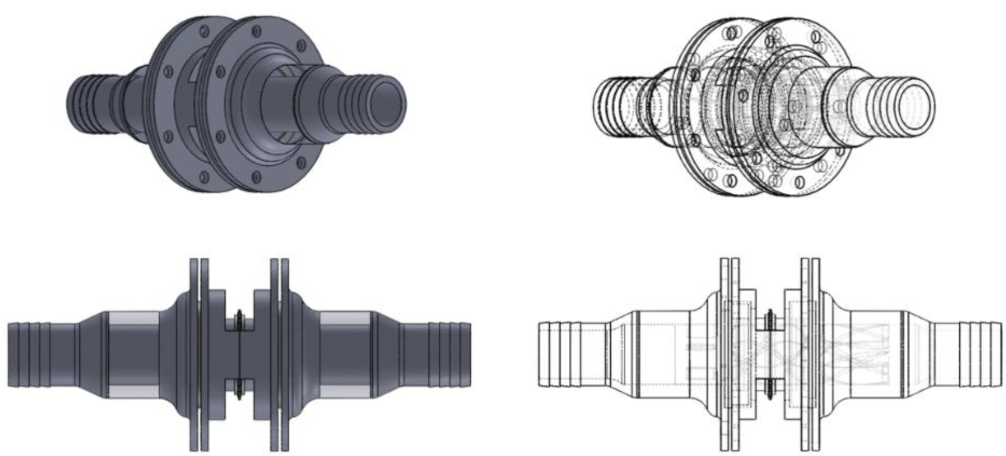

Figure 3.10 Pump geometry.
'Shaded' (left) and 'Hidden Lines' (right) views.

To properly integrate the pump in the test rig, the geometry had some geometrical adjustments such as the incorporation of a driver sprocket on the impeller (Fig. 3.11), to rotate the impeller from its outer circumference, and two ceramic bearings (6806-LL/T9/C3 LD SI3N4 30X42X7 mm, Boca Bearings, Florida, USA) along with a 3D printed stationary casing, to axially support the impeller with seven stainless steel rods (93805A636, McMaster-Carr, Illinois, USA). Figure 3.12 shows the exploded view of the adapted pump design.

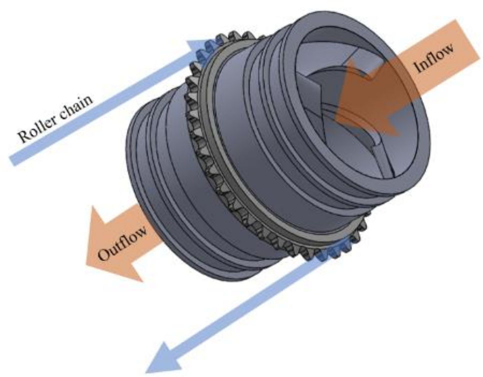

Figure 3.11 Modified drawing of the impeller with driver sprocket and inflow, outflow and rotation directions.

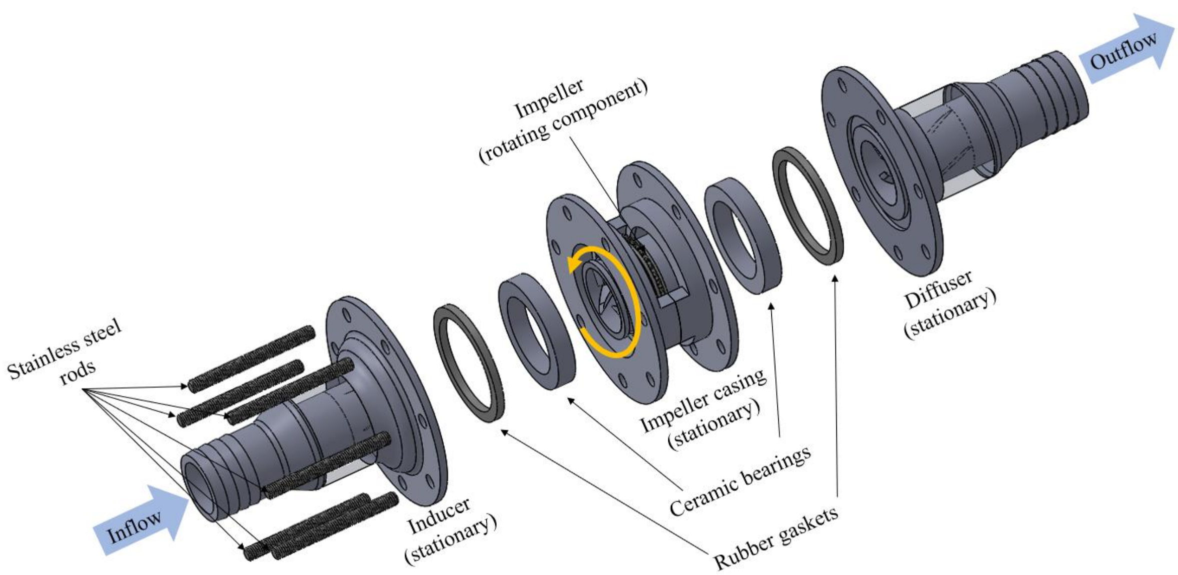

Figure 3.12 Exploded view of the pump showing the external components and the impeller rotation direction highlighted in yellow.

Initially, steel bearings were used to rotate the impeller, but the metallic bearings wear as a result of the fluid interaction, affecting thus, power measurements. Therefore, metallic bearings were replaced with ceramic bearings due to their excellent corrosive-resistant properties.

To prevent leaks, mechanical seals (Fig. 3.13) were placed in three sections of the pump assembly. The first one was designed as an L shape with silicone mold rubber (Smooth-On Pennsylvania, USA) and was placed between the outer static part of the ceramic bearings and the impeller casing. For the second seal, a rubber gasket (5081K89, McMaster-Carr, Illinois, USA) was used to provide a tight seal between the inducer or diffuser flanges and the static part of the bearing and casing. And the last sealing, made of PTFE tape (4502K32, McMaster-Carr, Illinois, USA), was placed in the outer impeller flanges and the rotating part of the bearing to provide tight seal during rotation.

.

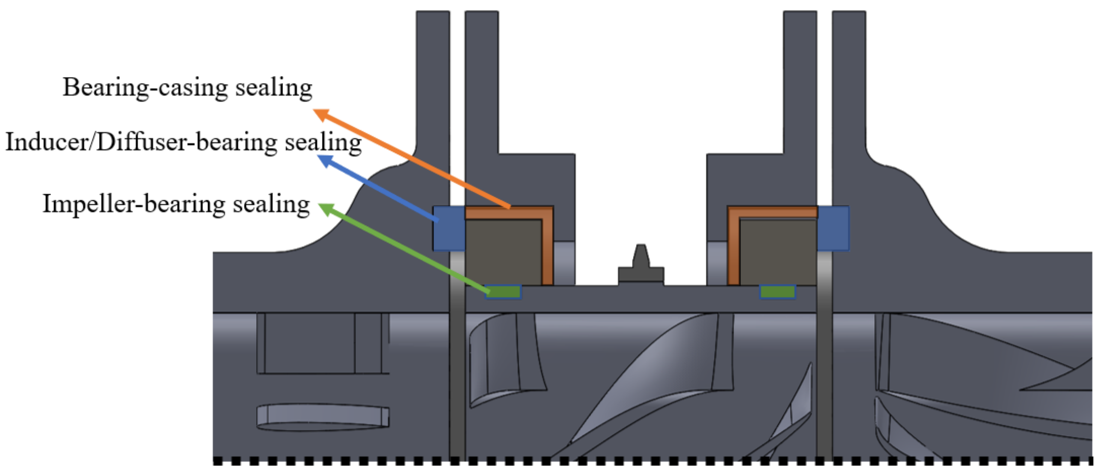

Figure 3.13 Three portions of the pump (highlighted in blue, green and orange) where the mechanical seals were incorporated between stationary and rotary parts of the pump.

3.3.2 3D Printed Prototypes

The first pump was quickly manufactured using a cost-effective fused deposition modeling (FDM) 3D printer (Ultimaker 3, Ultimaker, Utrecht, Netherlands). The manufacturing process of FDM printers is additive, hence, an object is built by extruding melted thermoplastic in a predetermined layer-by-layer path.

The initial prototype was printed using polylactide (PLA) filament of $2.86\ x\ 10^{-3}$ m of diameter with a layer resolution of 200 µm and 40% of infill support. The final product is shown in figure 3.14.

Figure 3.14 Initial pump prototype using a FDM printer.

Because FDM printing has the lowest dimensional accuracy and resolution when compared with other 3D printing technologies [115], the model did not provide suitable mechanical and hydraulic integrity for testing, therefore a second prototype was developed using a stereolithography (SLA) printer (Form 2, Formlabs, Massachusetts, USA). SLA printing process consists of selectively curing successive layers of resin with a highly-focused UV laser [115]. SLA printers are known for having better printing resolution than FDM printers and are suitable for complex prints. In this context, a clear photopolymer resin (RS-F2-GPCL-04, Formlabs, Massachusetts, USA) was used to develop the second and final 'hubless' pump prototype with a layer resolution of 25 µm.

The post-processing procedure consisted of 15 minutes of wash in a 99% IPA solution and 15 minutes in a curing unit for the material to achieve its optimal mechanical properties. Figure 3.15 shows a transparent printing comparison between the chosen SLA printer (left) and the initially used FDM printer (right). The final disassembled pump prototype is shown in figure 3.16

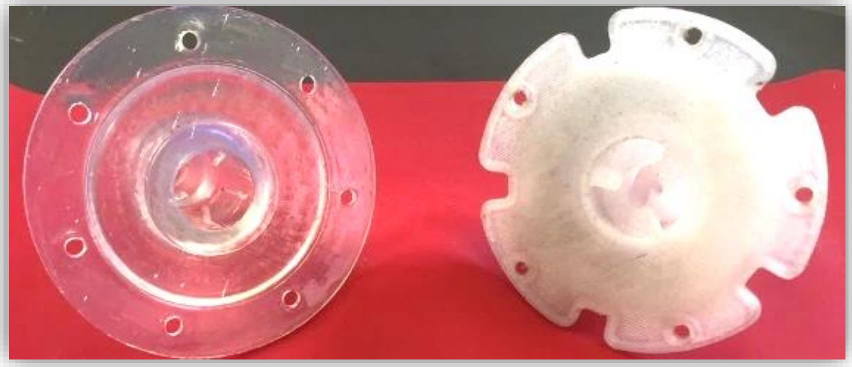

Figure 3.15 SLA and FDM transparent pump model comparison.

A. B. C.

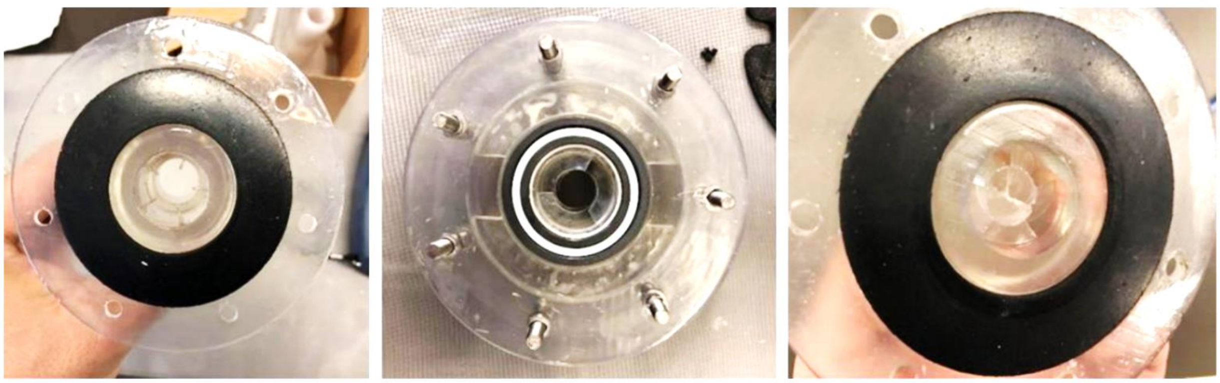

Figure 3.16 Final pump prototype presented in sections. (A) Inducer and bearing sealing. (B) Impeller and internal sealings within the impeller casing and ceramic bearings. (C) Diffuser with bearing sealing.

3.4 Design and Construction of the Hydraulic Test-Rig

This section provides an overview of the materials, sensors and components used to construct the hydraulic test rig for in-vitro performance testing.

A hydraulic test rig was constructed to obtain the performance curves of the ‘hubless’ LVAD configuration. Figure 3.17 shows a picture of the continuous-flow test-rig, along with its physical components. A detail description of the electrical system integration is described in section 3.4.4.

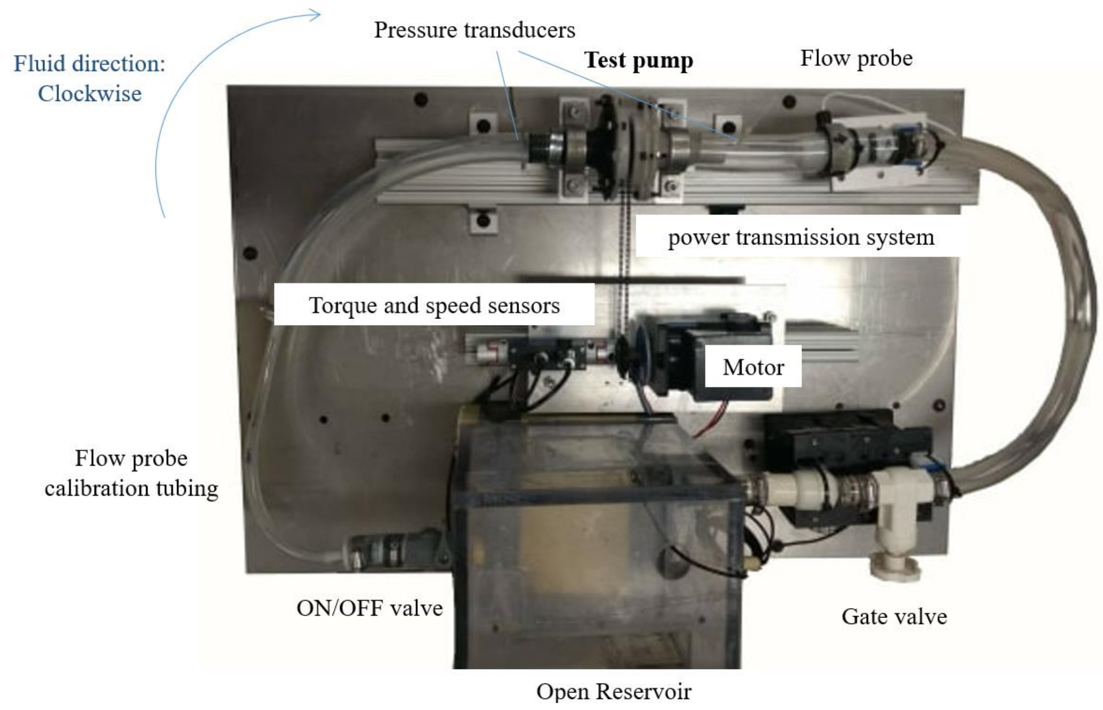

Figure 3.17 Top view of the hydraulic test rig for in-vitro experiments and respective components

3.4.1 Power Transmission System

Since magnetic bearings are intended to suspend the rotor in the housing for outer activation [1], the test rig included a 1:1 power transmission system to properly rotate the impeller from its outer embodiment (Fig. 3.18).

Figure 3.18 One-on-one power transmission system.

A lightweight acetal miniature roller-chain of 0.1227" pitch (64225K72, McMaster-Carr, Illinois, USA) and two press-fit miniature sprockets of 0.1227" pitch with 36 teeth (64205K831, McMaster-Carr, Illinois, USA), were used to assure rotation between the driver and driven sprockets with the least frictional loss. The driver sprocket was placed on the shaft of the motor (59835K62, McMaster-Carr, Illinois, USA), while the driven shaft was placed at on outer part of the impeller.

Because the 1:1 gear ratio on the power transmission system assures equal rotation in the motor and in the impeller. The speed measurement system was placed on the motor's side of the power transmission system.

3.4.2 Speed Control System

A 1 hole 3D printed encoder disc, a generic photoelectric infrared sensor module (LM393), a motor controller (HB-25,Parallax, California, USA), and a microcontroller development board (Arduino Uno, Arduino, Massachusetts, USA) were used to measure and regulate the rotating speed of the motor. Figure 3.19 shows the electronic schematic of the speed control system.

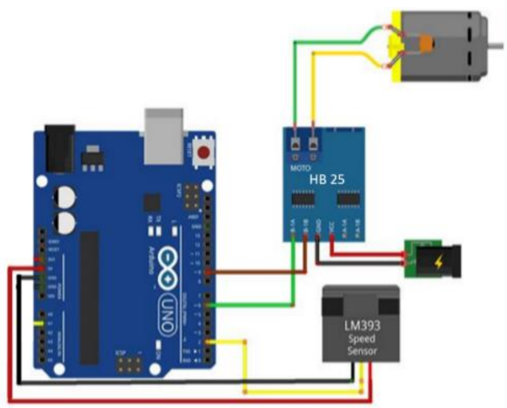

Figure 3.19 Electronic schematic of speed control using Arduino.

Similarly, a PID closed-loop control system was generated to regulate the speed. A proportional–integral–derivative (PID) control loop is a mechanism employing feedback to modulate a signal. It calculates an error value e(t) as the difference between the desired set point (SP) and the measured process variable (PV) and applies a correction based on proportional, integral, and derivative terms.

The constants of the DC motor transfer function $G(s)\frac{Km}{\tau s+1}$, were obtained using the least-squares method (LSM) and the block diagram of the motor's characterization was used to compute the PID constants through the PID autotuning tools of Simulink (MATLAB R2017b, MathWorks, Massachusetts, USA). Figure 3.20 shows the block diagram of the PID implementation in Simulink along with the first-order transfer function of the DC motor. More details about the auto-tuning of the PID constants and developed software are shown in Appendix B.

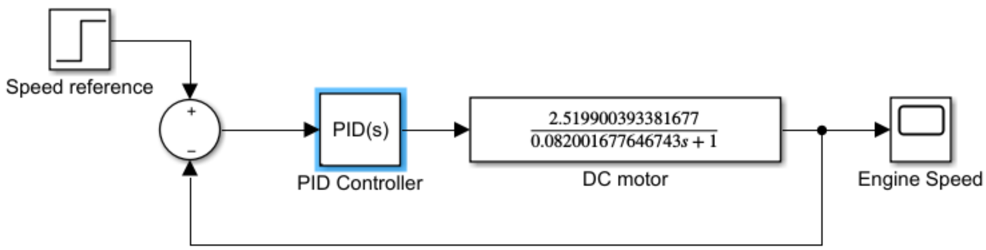

Figure 3.20 Simulink Block diagram for the assessment of the PID constants.

3.4.3 Sensors

A torque sensor (ZHKY8050DS, Shenzhen Sensor and Control Co., Shenzhen, China) and a torque meter (PY801, Shenzhen Sensor and Control Co., Shenzhen, China) were incorporated in the rig to compute the dynamic rotary torque of the shaft of the motor. To axially support the sensor with the shaft of the motor and the driver sprocket, two mechanical couplings were included.

Likewise, two aluminum supports were machined to hold the sensor in place and a 50A neoprene bed of 6×10^{-3} m thickness (1290N17, McMaster-Carr, Illinois, USA) was included and to dampen vibrations. Figure 3.21 shows the physical adaptation of the torque sensor on the test rig.

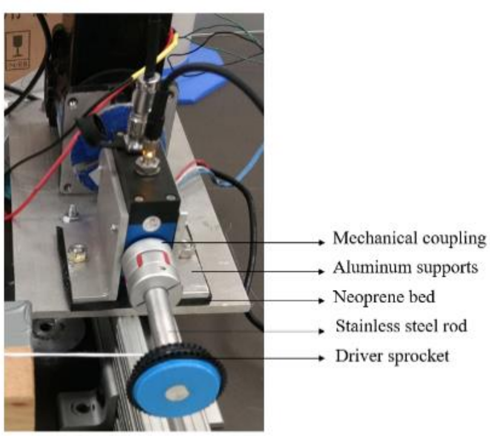

Figure 3.21 Torque sensor setup on the test rig.

Two catheter pressure transducers (SPR-524 Mikro-Tip ®, Millar Instruments Inc., Texas, USA) and a pressure control unit (PCU-2000, Millar Instruments Inc., Texas, USA) were used to quantify the pressure rise across the pump. The first sensor was placed at the inlet portion of the inducer and the second at the outlet portion of the diffuser.

An ultrasonic flow probe (EP690, Carolina Medical Electronics, Inc., North Carolina, USA) was placed at the outlet section of the pump to measure flow rate. An electromagnetic flowmeter (501D, Carolina Medical Electronics, Inc., North Carolina, USA) was required to amplify and transmit the output signal of the sensor for data acquisition.

Abrasive-resistant flexible rubber tubing (5546K53, McMaster-Carr, Illinois, USA) and general purpose worm clamps were used to adjust the flow probe to the piping network, as shown in figure 3.22.

Figure 3.22 Flow probe adjustment on the test rig.

A digital tachometer was used to compare speed measurements with Arduino readings. Calibration weights traveling at a constant speed were used to validate torque sensor measurements. A syringe and pressure gauge system (Fig. 3.23) was used to verify pressure values, and a peristaltic pump (7523, Masterflex L/S™ Easy-Load, Cole Palmer, Illinois, USA) was placed in series with the flow probe to validate flow rates.

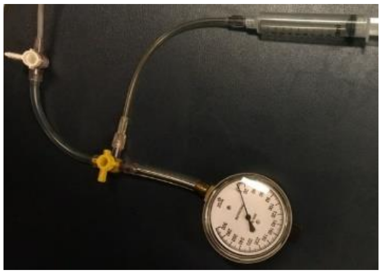

Figure 3.23 In-house pressure validation system for pressure sensor gain adjustment prior in-vitro data acquisition.

3.4.4 Data Acquisition System

The output voltages of pressure transducers and flow sensor were transferred into a Data Acquisition Card *DAQ* (USB-6009, NI, Texas, USA) using three universal 1/4” mono plug TS cables. Two cables were used to acquire single pressure signals and the last one to acquire the flow rate output voltage signal.

Torque measurements were directly read from the torque meter and speed measurements were included in the LabView interface through the USB port. Figure 3.24 shows the DAQ ports used to acquire pressure and flow signals.

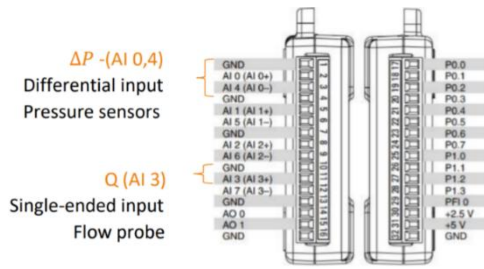

Figure 3.24 NI DAQ pin selection for pressure sensors and flow probe placement.

Using LabView (LabView 2016, NI, Texas, USA), a customized software was developed for data visualization. Figure 3.25 show the block diagram of the system and figure 3.26 shows the flow chart logic implemented on the software.

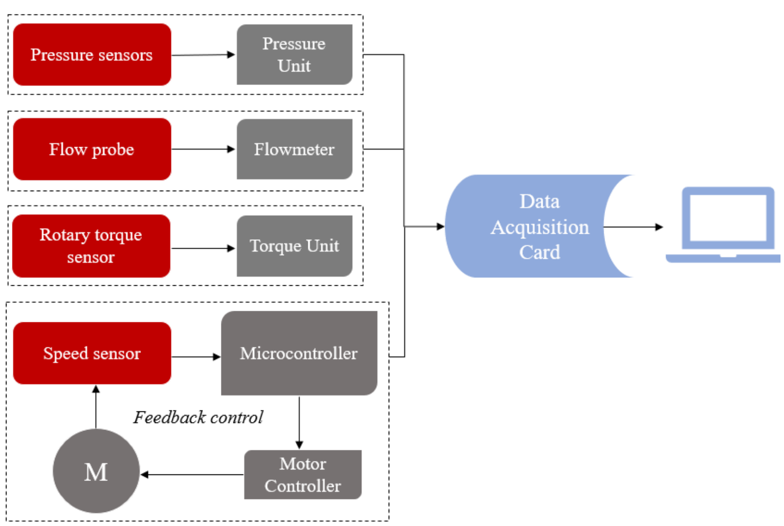

Figure 3.25 Block diagram of the data acquisition software.

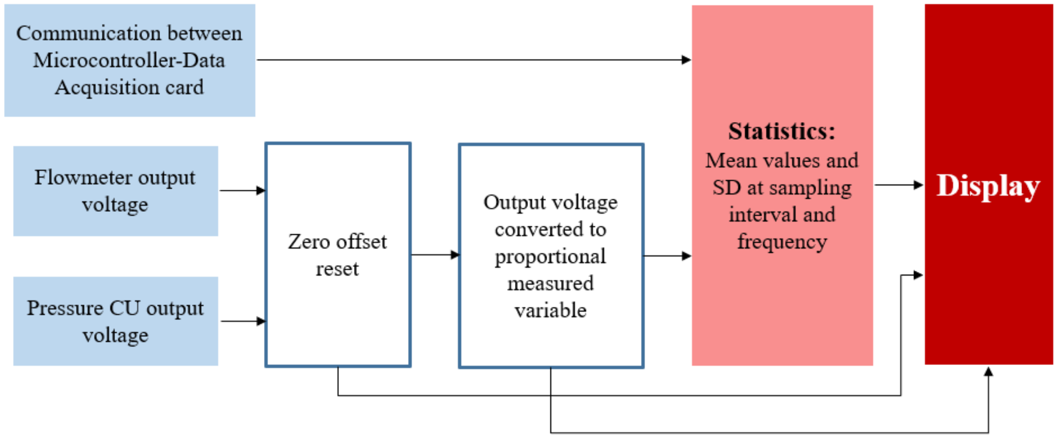

Figure 3.26 Flow chart logic of the LabView software.

LabView interface data files were saved as .csv extension and data analysis was performed after converting the files into a spreadsheet format. Details about the initial calibration and the experimental protocol are provided in Appendix C.

Figure 3.27 shows the visualization panel of LabView interface, and, as seen in the image, the recording sampling rate (Hz) can be modified by the user.

The visual panel also displays the output raw voltage coming from the sensors, the offset zero adjustment, and continuous and averaged values of pressure rise, flow rate and current rotating speed with their respective units of measurement ($\mathrm{mmHg}, \mathrm{L\ min^{-1}}, \mathrm{RPM}$). Appendix D includes the LabView block diagram schematic.

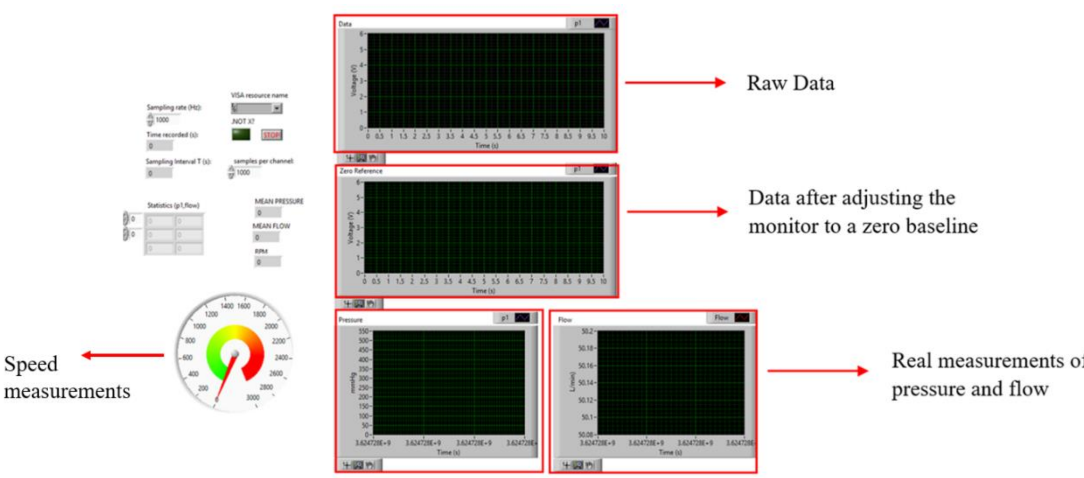

Figure 3.27 Visualization panel of the generated LabView program.

3.4.5 Hydraulic Network

A flexible clear tubing of 1” ID (6516T34 Tygon, McMaster-Carr, Illinois, USA) widely used in cardiovascular in vitro systems [6, 41, 74, 94, 116] was used to create the hydraulic piping network of the test-rig along with a transparent 7 L fluid reservoir open to atmospheric pressure.

The hydraulic connections were made using conventional pipe fittings and connectors and several hydraulic considerations were taken into account to eliminate undesirable resistances and pressure drops within the hydraulic circuit, such as: having a greater bending radius than the minimum allowed bending radius of the tubing, the use of gradual reducers (if needed), avoidance of compound bends, T fittings, and prevention of tubing twisting.

Since flow measurements are taken predominantly in the turbulent flow regime at $N = 335.1$ rad s^{-1}, the length of the tubing prior entering the flow probe was determined using the turbulent fully developed flow profile equation; in which for a $Re = \frac{\rho\, D^2 N}{\mu} = \frac{(1080\ \mathrm{kg\ m^{-3}})(0.0254\ \mathrm{m})^2\ (335\ \mathrm{rad\ s^{-1}})}{(3.5 \times 10^{-3}\ \mathrm{Pa\ s})} = 66{,}711$, the tubing length following a turbulent regime is $L_{turbulent} = 5.3\ Re^{0.12}\ d = 5.3\ (66{,}711)^{0.12}(0.0254\ \mathrm{m}) = 0.47\ \mathrm{m}$.

To run the test pump over its full performance rate, a gate valve was placed at the inlet of the reservoir and at the outlet of the flow probe to vary flow resistance.

Since the assumption of a Newtonian behaviour becomes acceptable in LVAD environments (shear rates > $100\ s^{-1}$), a Newtonian fluid mixture of glycerine in water was used as a blood analog fluid [113, 117-120]. Using a capillary Ubbelohde viscometer (SK-98934-12, Cole Palmer, Illinois, USA) and a weight balance, different glycerine concentrations between from 35% to 47% were tested to verify the fluid properties of the mixture at ambient temperature (23.5◦C). The results are shown in figure 3.28, and, in conclusion, the mixture of 37% of glycerine in water provided better blood-mimicking behaviour in terms of dynamic viscosity μ and density ρ as 3.46×10^{-3} Pa s and $1082\ \mathrm{kg\ m^{-3}}$, respectively.

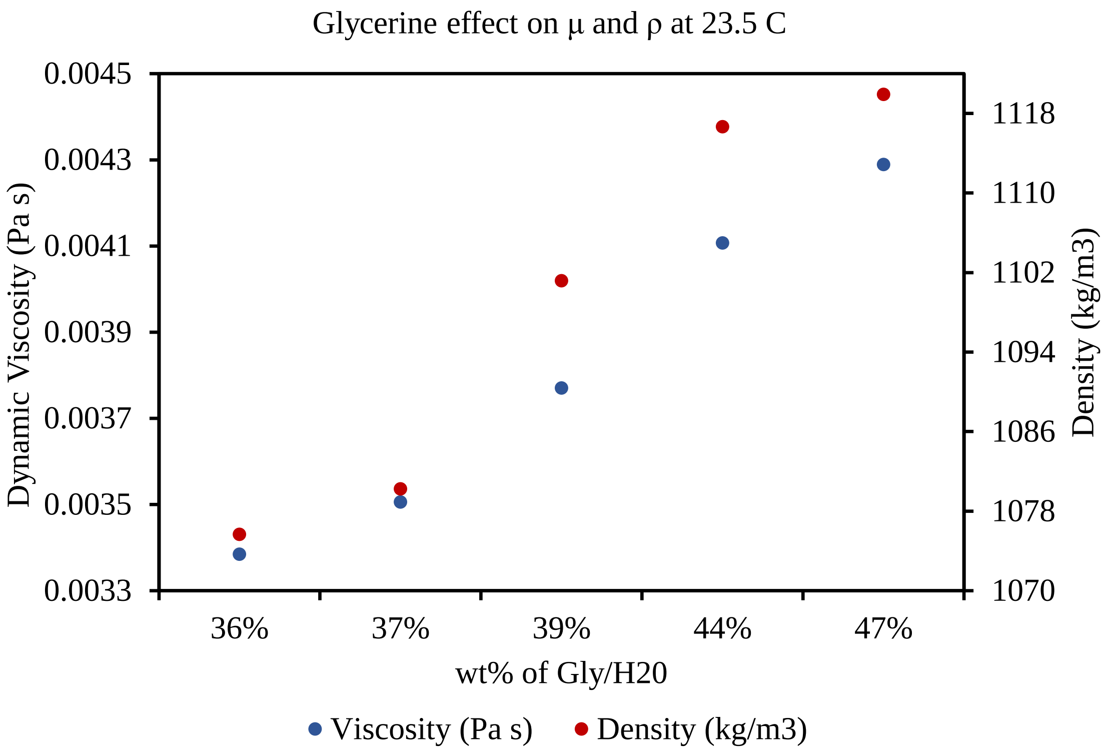

Figure 3.28 Dynamic viscosity and density as functions of Glycerine in water.

CHAPTER 4: RESULTS

Numerical and experimental results are presented in this chapter. The first section covers the results of the CFD-based methodology, while the second one presents the in-vitro experiments conducted on the hydraulic test-rig.

4.1 Numerical Solutions

Residual values of the mass and momentum equations and the parameters of interest: flow rate Q, pressure rise ΔP, and torque τ, were tracked in the convergency log. The parameters of interests were defined as expressions in CFX-Pre and monitored in CFX solver at each time step.

Figure 4.1 shows an example of the convergence log at $Q = 5\,x\,10^{-5}$ $\mathrm{m^3\,s^{-1}}$ and N=335.10 rad $\mathrm{s^{-1}}$. Figure 4.1A shows the RMS values reaching convergency criteria of $<10^{-5}$, while figure 4.1B shows stability in the values of the parameters of interest after an accumulated timestep of ~ 200.

A.

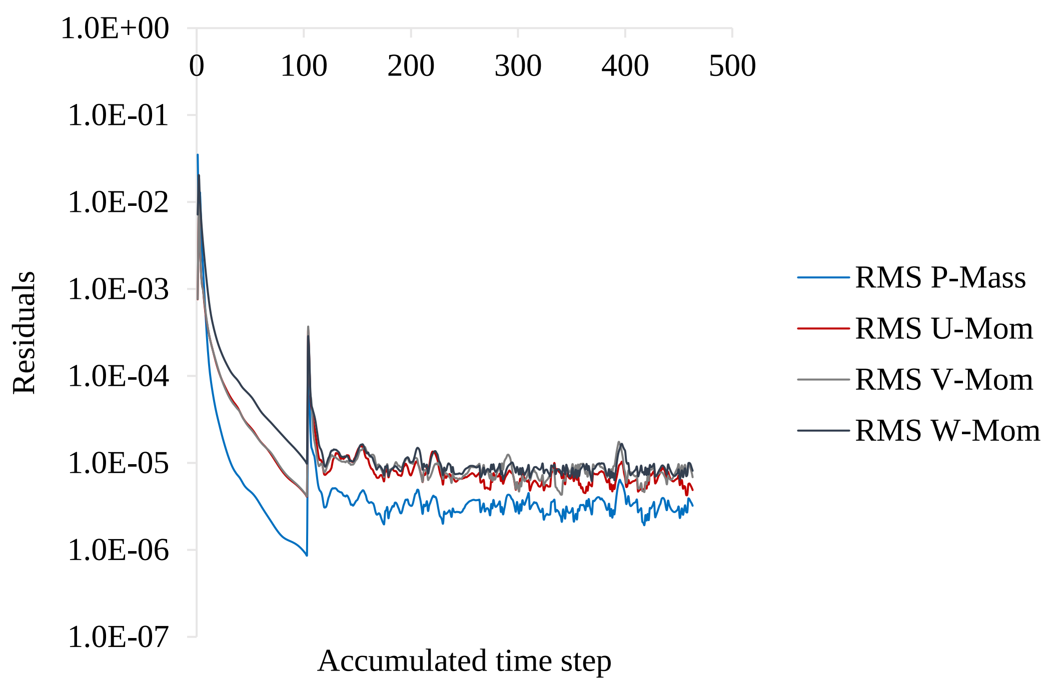

B.

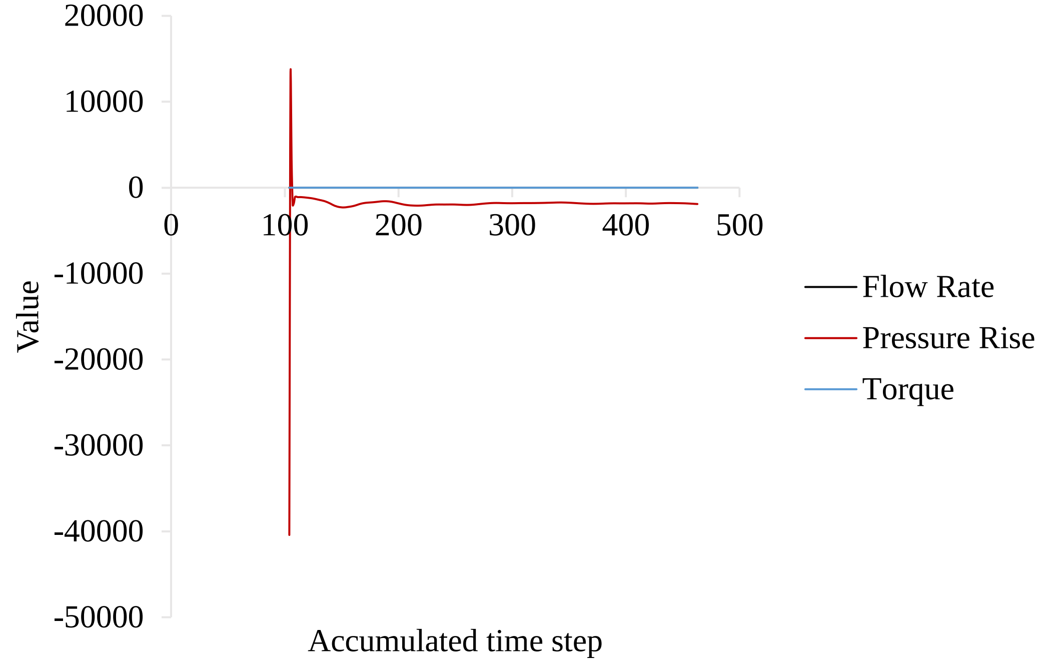

Figure 4.1 (A) Mass and Momentum convergency log and (B) monitored parameters at the Design Operating Point

Since the SST turbulent model provides a more accurate prediction of boundary layer separation, Y plus (Y+) was evaluated. Y+ is a non-dimensional wall distance used to describe how coarse or fine a mesh is. It helps determining if the size of the elements near the fluid domain walls were properly defined; and for accurate solutions, small Y plus values are highly desirable and should not exceed a value of 200.

Figure 4.2 shows localized Y+ contours on the walls of the fluid domain at the lowest and highest rotational regimes at Q = 5×10^{-5} $m^3\ s^{-1}$. As seen in the image, Y+ values ranged between 5 and 60, and were kept within the limits. No adjustments were made in the legends nor ranges of all CFX results presented below (i.e., only automatic default scales were included in graphic CFX results).

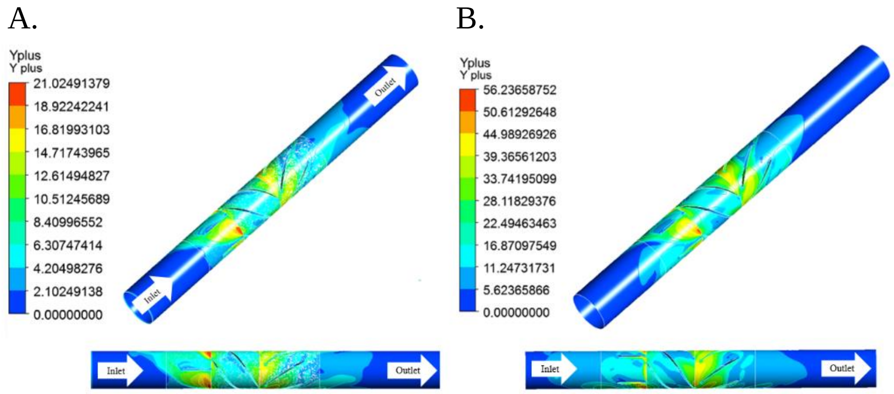

Figure 4.2 Side and Isometric views of the Y-plus wall contours at (A) $N = 209.43\ \mathrm{rad/s}$ and (B) and $N = 837.75\ \mathrm{rad/s}$.

The streamline distribution of flow velocities from the inlet to the outlet was used to evaluate recirculation and stagnation zones in Design A and Design B at different rotational speeds. Figure 4.3 shows the flow velocity vector as a function of rotational speed and flow rate. As seen in the image, flow velocity streamlines exhibited whirl at the diffuser portion of the pump and higher stagnation zones were observed between the inducer-impeller interface than at the impeller-diffuser interface.

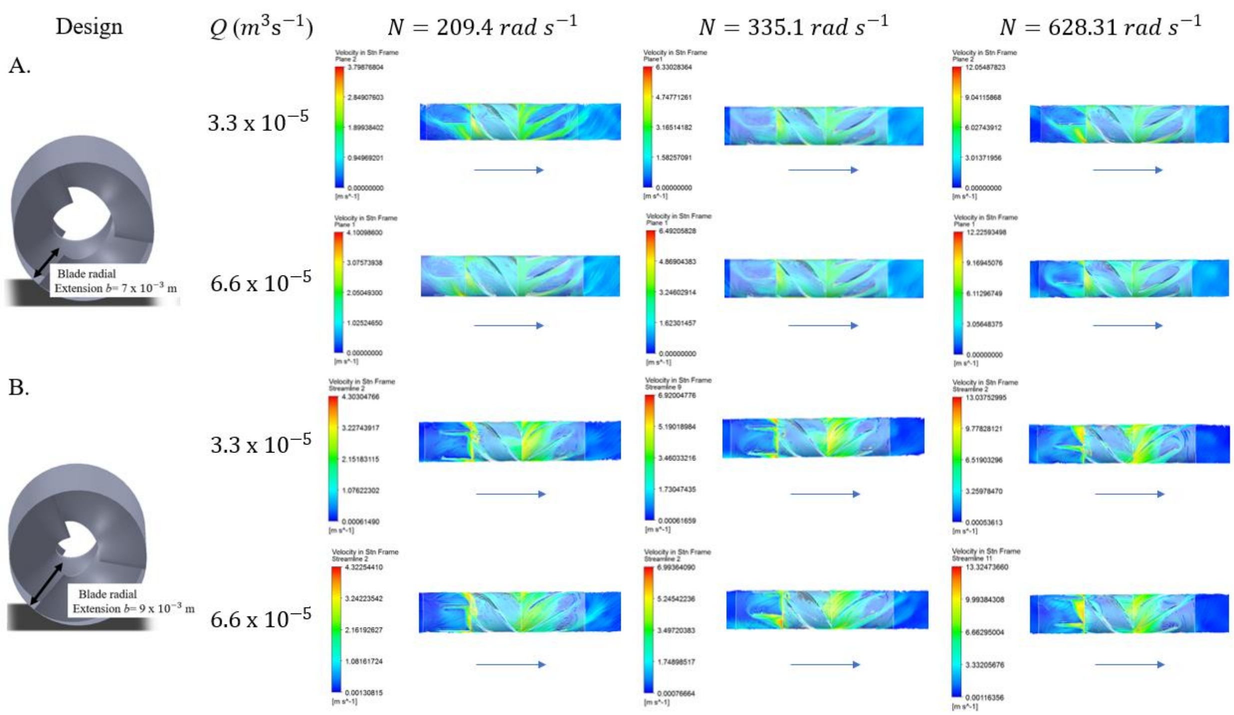

Figure 4.3 Flow velocities of (A) Design A and (B) Design B.

Since wall shear stresses (WSS) can be used as initial predictors of critical shear stresses, and blood damage, WSS contours of Design A and Design B were evaluated at different flow rates and rotating speeds. Figure 4.4 shows the wall shear stress contours at Q = 3.3 x 10^{-5} $\mathrm{m}^3\ \mathrm{s}^{-1}$, $6.6\ x\ 10^{-5}\ m^3\ s^{-1}$ and N= 209.4 rad s^{-1}, 335.1 rad s^{-1}, 628.31 rad s^{-1}. No range adjustments were made on the legend of the plots.

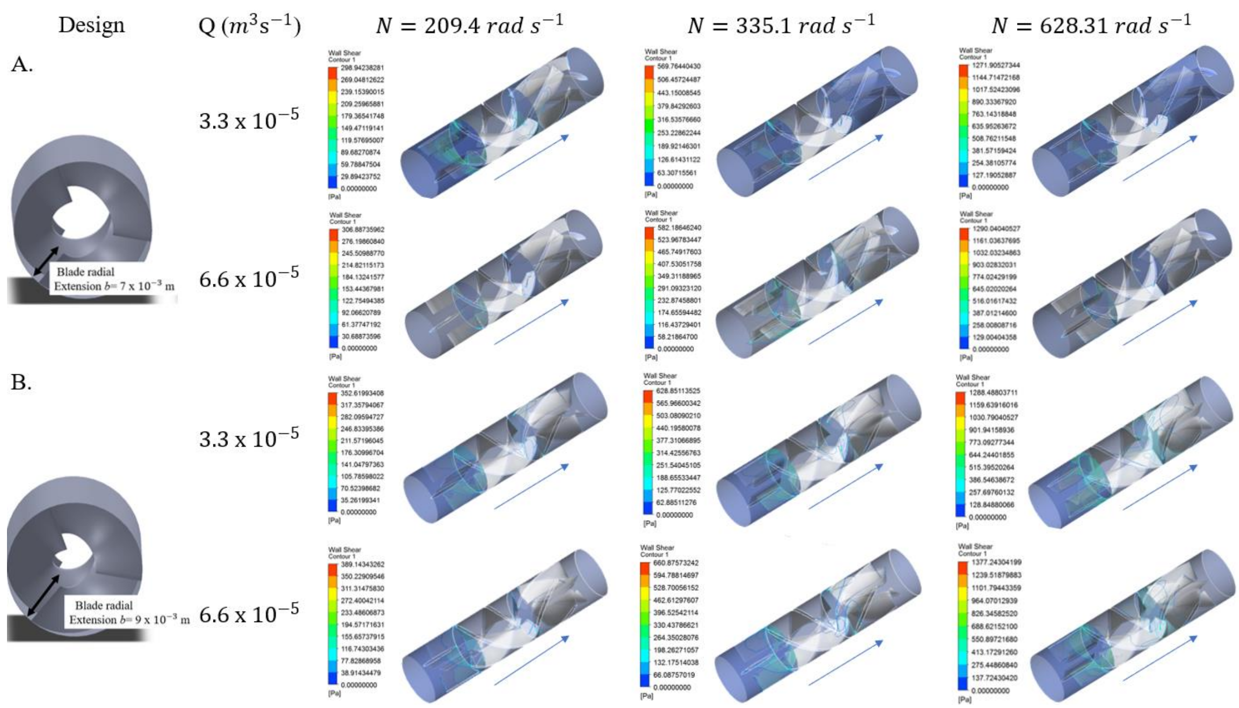

Figure 4.4 Scalar wall shear stresses of (A) Design A and (B) Design B at different operating regimes.

Moreover, the average WSS for nominal Q = 3.3 x 10^{-5} m s^{-3} and 6.6 x 10^{-5} m s^{-3} at different operating speeds are shown in Table 4.1

Table 4.7 Numerical WSS of Design A and Design B at different operating conditions

	Flow rate Q (m s^{-3})	N=209.4 rad s^{-1}	N=335.1 rad s^{-1}	N=628.31 rad s^{-1}
Design A	3.3 x 10^{-5}	150 Pa	322 Pa	726 Pa
	6.6 x 10^{-5}	185 Pa	341 Pa	780 Pa
Design B	3.3 x 10^{-5}	210 Pa	368 Pa	820 Pa
	6.6 x 10^{-5}	245 Pa	392 Pa	956 Pa

Flows within the pump were evaluated based on the pump Reynolds number Re_p ($Re_p = D^2\rho\, N\,/\mu$) and the axial-flow Reynolds number Re_a ($Re_a = D\rho v\,/\mu$).

Calculations of Re_p were assessed at different rotating speeds (N =209.4 rad s^{-1}, 335.1 rad s^{-1}, 418.87 rad s^{-1}, 628.31 rad s^{-1}, and 837.75 rad s^{-1}) and are given in Table 4.2.

Table 4.8 Pump Reynolds Number at different rotating speeds.

External diameter D (m)	Density ρ (kg m^{-3})	Rotational speed N (rad s^{-1})	Dynamic viscosity μ (kg $m^{-1}s^{-1}$)	$Re_p = \dfrac{D^2\rho\, N}{\mu}$
2.5 x 10^{-2}	1060	209.4	3.5 x 10^{-3}	39.643 x 10^3
		335.1		63.430 x 10^3
		418.87		79.287 x 10^3
		628.31		118.931 x 10^3
		837.75		158.575 x 10^3

To evaluate the axial-flow Reynolds number Re_a ($Re_a = OD\rho v\,/\mu$), two cross-sectional planes located at the inlet and outlet portions of the impeller were created. Figure 4.5 illustrates the average Re_a of both design variations (Design A and Design B) over the whole capacity range at N=335.1 rad s^{-1}.

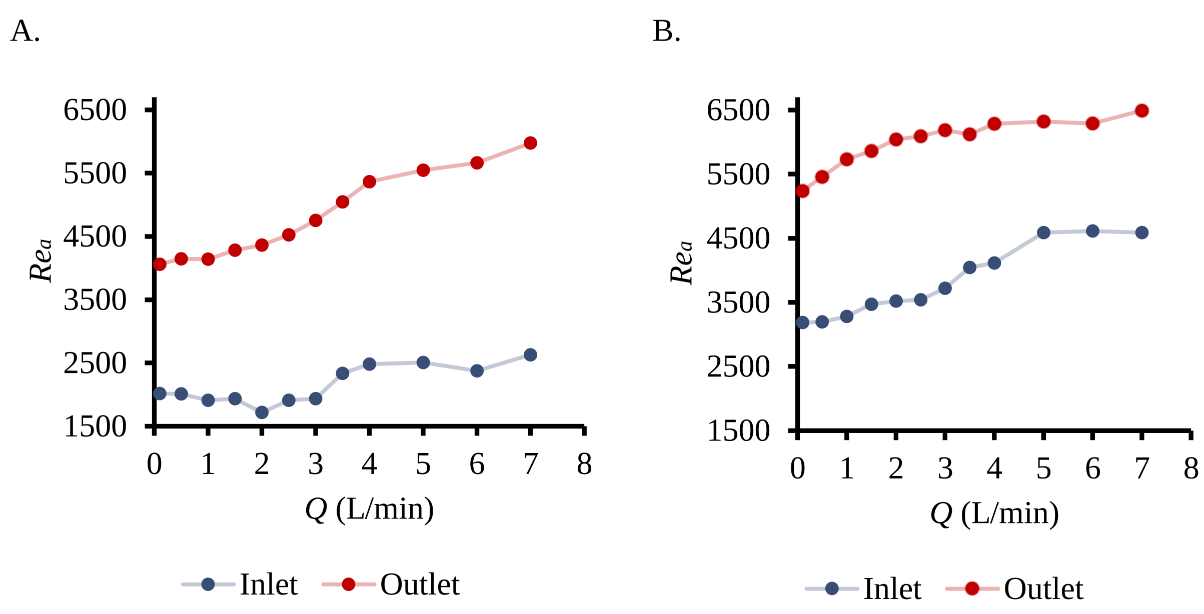

Figure 4.5 Re_a of (A) Design A and (B) Design B as a function of flow rate Q.

Similarly, pressure rise ΔP was evaluated using cross-sectional planes at the inlet and outlet portions of the pump and averaging the pressure values through the plane. To illustrate the approach, figure 4.8 shows an example of cross-sectional pressure planes at different axial lengths of the pump at a specific operating point.

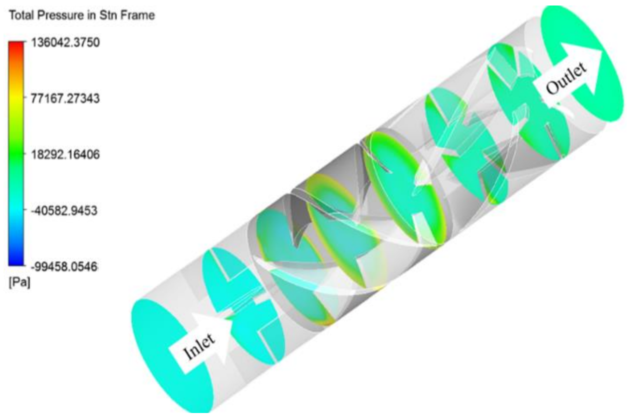

Figure 4.8 Cross-sectional pressure planes at different axial lengths of the pump. (CFD results of Design A at Q= 2 L min^{-1} and N= 837.75 rad s^{-1}).

Pressures in CFD analysis are relative to the reference and to the absolute pressures specified in the boundary conditions; the negative values represent the suction line, while the positive ones represent the discharge line. Figure 4.8 illustrates higher pressures at the outer contours of the impeller section due to the rotational speed to which the component is exposed to. Using CFD, the pressure rise ΔP across Design A and Design B was virtually determined for flow rates of Q =1.666 x 10^{-6} m^3s^{-1} to 1.166 x 10^{-4} m^3s^{-1} (Fig. 4.9) at different rotating speeds.

A.

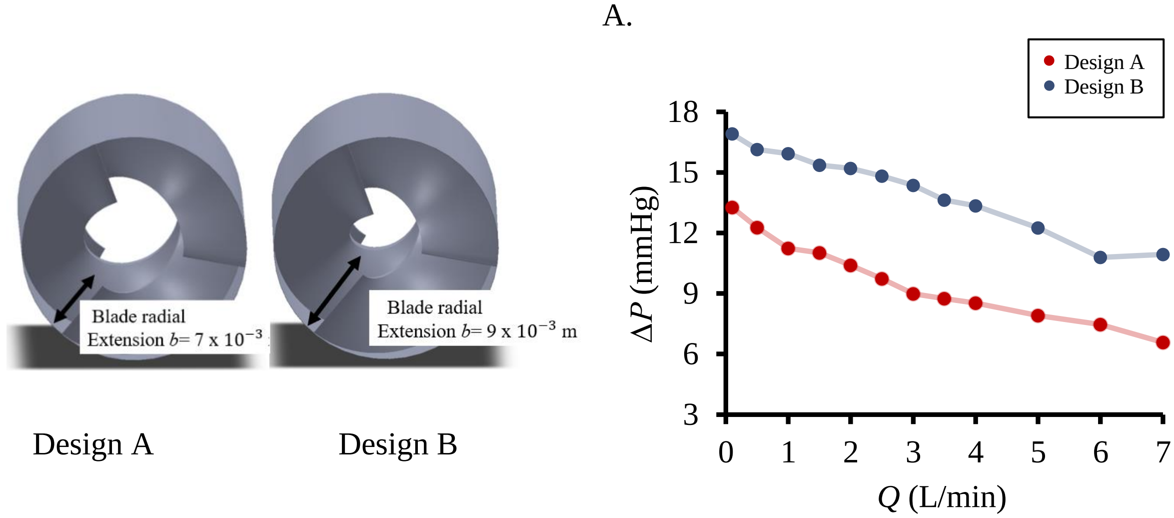

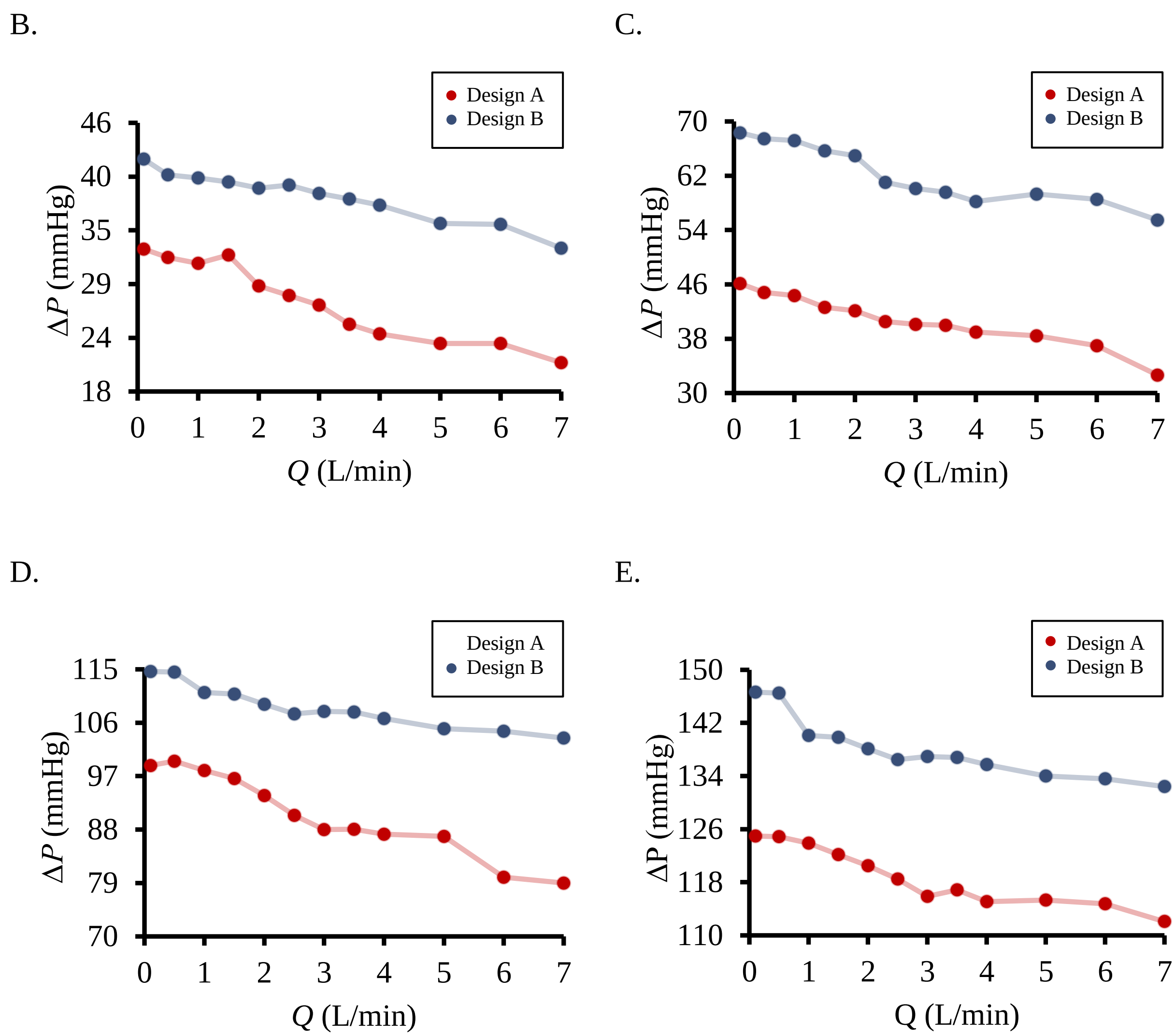

Figure 4.9 CFD HQ curves for Design A and Design B at (A) 209.4 rad/s. (B) 335.1 rad/s. (C) 418.87 rad/s. (D) 628.31 rad/s. (E) 837.75 rad/s.

4.2 Experimental Results

A functional prototype of Design A was tested varying the resistance of the system with a flow restriction valve. The experimental HQ curve and the hydraulic efficiency curve along with the already predicted CFD results are shown in figure 4.10.

A.

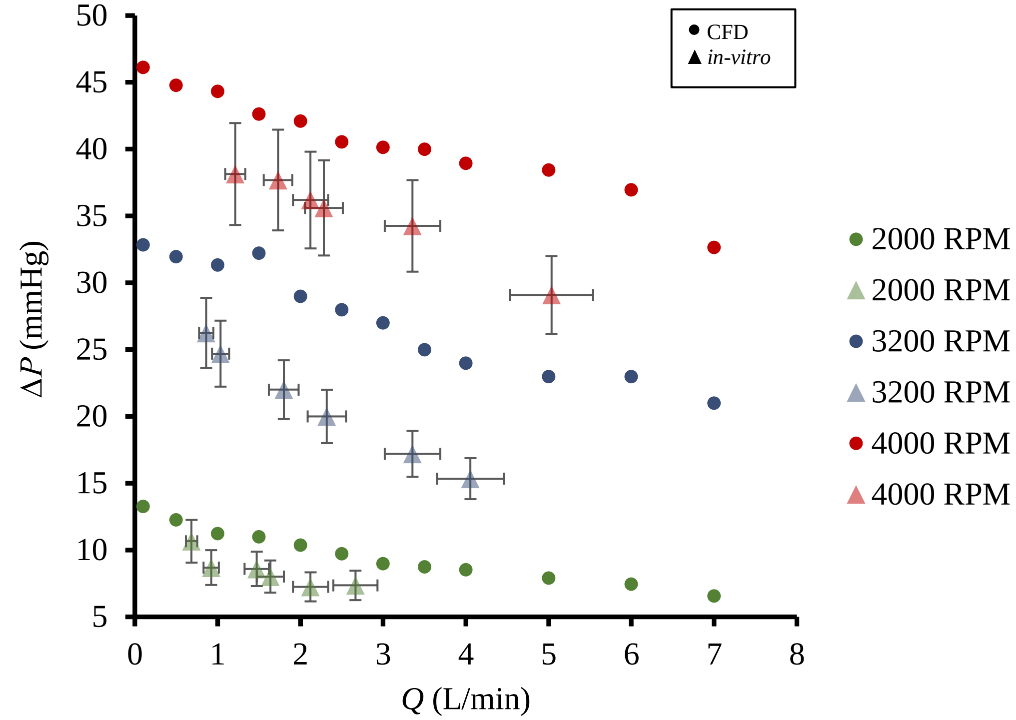

B.

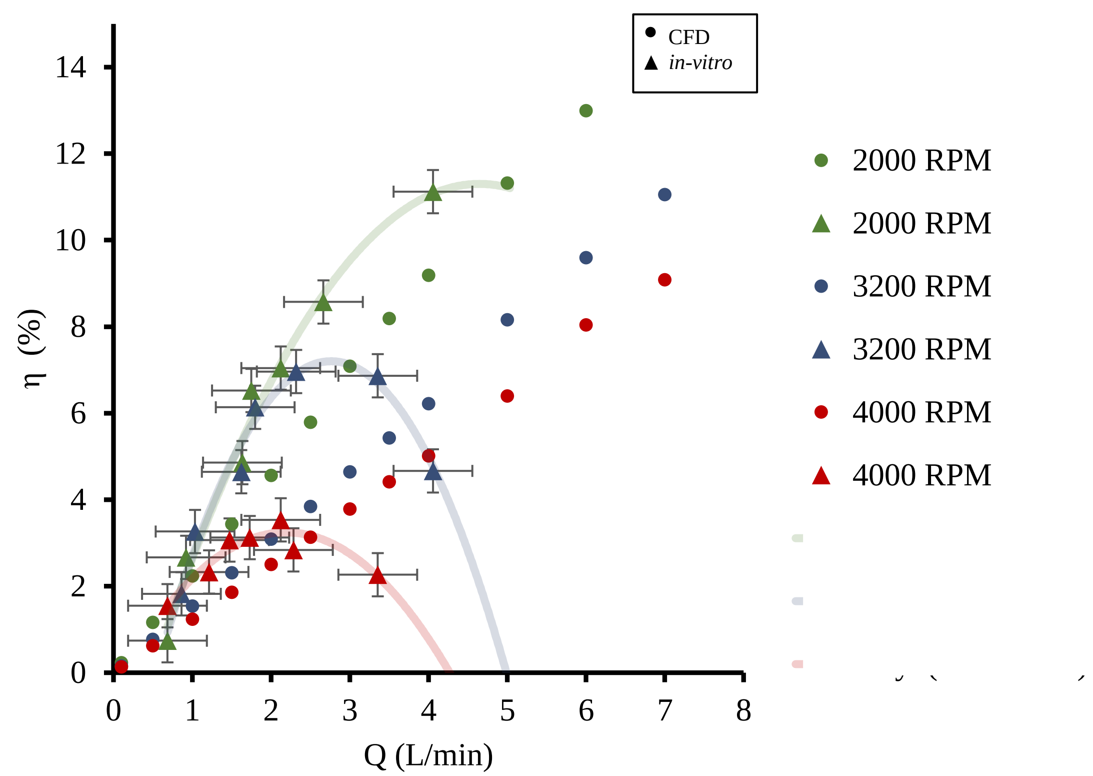

Figure 4.10 Numerical and experimental (A) HQ curve and (B) η curve of Design A.

CHAPTER 5: DISCUSSION, LIMITATIONS, AND FUTURE WORK

5.1 Discussion of Results

The evaluation of scalar wall shear stresses was used as an initial predictor of blood damage. Figure 4.4 shows that for all operating regimes, high WSS was encountered at the interface regions of the impeller. Likewise, it was observed that WSS increased as a function of the rotating speed N and flow rate Q. For Q = 5 x 10^{-5} m s^{-3} , a maximum wall shear stress of ~1.150 x 10^{3} Pa was encountered at N = 837.75 rad s^{-1}, which results in a potential erythrocyte rupture. Therefore, a further increase in rotational speed would potentially increase blood trauma. Moreover, an increase of blade radial extension b (Design B) resulted in higher shear stress because of the additional length for boundary layer growth, which increased the risk of blood damage. Since blood damage depends on magnitude and duration of exposure, this study should extend investigations to exposure times, and different turbulence models to create a database for potential functional correlations. In addition, it is important to note that blood should be modeled as a non-Newtonian fluid and that the resolution of the mesh near the walls should be adjusted to keep low Y+ values to accurately capture wall shear stress. A reliable CFD model to quantify blood damage also needs more detailed knowledge about the mechanics of RBC membranes under complex fluid dynamics conditions.

The pump Reynolds number was used as a flow comparison parameter at different operating regimes. It ranged from $\sim 40 \times 10^{3}$ at N = 209.4 rad s^{-1}, up to a maximum of ~160 x 10^{3} at N = 837.75 rad s^{-1} . This demonstrates that pump Reynolds number is within the range of commercially available adult pumps such as HeartMate III and CentriMag ($Re_p \approx$ 77.59 x 10^{3} – 155.32 x 10^{3}) [46]. Additionally, the axial-flow Reynolds number was computed at the inlet and outlet portion of the impeller at N = 335.1 rad s^{-1}. Over the whole capacity range, the inlet portion of Design A resulted in laminar and transitional flows (0 < Re_a < 2500), whereas all other sections of analysis resulted turbulent flows (Re_a > 4000). Which leads to the conclusion that much of the flow is transitioning to a turbulent scheme. However, it is worth mentioning that the computed axial Reynolds number is influenced by the fluid-fluid interface from the frozen rotor frame, which accounts for the momentum transfer from the noninitial frame to the inertial one, and by the geometry of the virtual model. Therefore, more accurate predictions should account for the potential placement location of the pump (anatomical geometry) and the possibility of including the pulsatility of the heart.

Numerical HQ curve predictions (Fig 4.9) demonstrate a general trend of increased ΔP as a function of the rotating speed *N* was observed from the plots. A larger hollow cross-sectional area for flow (Design A) resulted in lower pressure rise ΔP when compared to the heads of Design B. At the design operating point DOP, Design A and Design B provided ΔP of 3.599 x 10^3 Pa and 5.066 x 10^3 Pa, respectively. However, at a rotating speed *N* = 628.31 rad s^{-1}, Design A and Design B were able to provide physiological relevant pressures for left ventricular support between 1.0665 x 10 ^{4} Pa and 15.332 x 10^4 Pa (Plot D, Fig. 4.9), shifting thus, the best efficiency point to a higher rotational speed *N*.

Through experiments at rotating speeds *N* of 209.4 rad s^{-1}, 335.1 rad s^{-1}, and 418.87 rad s^{-1}, the pump provided maximum flow rates Q of 4.5 x 10^{-5} m$^3 s^{-1}$, 7 x 10^{-5} m$^3 s^{-1}$, and 8.333 x 10^{-5} m$^3 s^{-1}$, respectively. Although the CFD predictions are not in good agreement with the experiments, the slope of the HQ curves follow the same flat behaviour over the entire range of rotational speeds tested. This indicates that the closing action of the flow restriction valve did not create much pressure drop in the pump. Similarly, at the DOP, the pump performed at ΔP = 2.733 x 10^3 Pa and a maximum hydraulic efficiency η = ~7.4%. However, the experimental hydraulic efficiency curves disclosed discrepancy with CFD predictions because the virtual predictions followed a linear flow-efficiency relationship. This could be attributed to the hydraulic efficiency dependency to the inlet boundary condition and to the flow idealization through simulations. Future numerical predictions should explore the pump performance at various combinations of boundary conditions to match experiments.

Moreover, the underestimated pressure rise (ΔP < 6.666 x 10^3 Pa [50 mmHg]) opens the possibility of exploring the hubless concept for other cardiovascular application, since the HQ Curves show adequate hydraulic relations for Fontan circulation or right ventricular support [121, 122]. The blade aerodynamic design through CF Turbo yielded an increase in efficiency of 5% at the design operating point when compared to preliminary reference design results [123].

5.2 Limitations and Future Work

Although significant progress towards the proof-of-concept POC has been developed, several limitations were encountered.

Due to the extensive and time consuming process to design 3D print and test prototypes, the project was limited to study the variation of only one blade parameter: blade radial extension b. Future work should consider an exhaustive exploration of the impact of each blade parameters (e.g. the number of blades, leading and trailing edge angles, wrap angle, blade thickness…) on the performance of the pump to better understand the flow dynamics of the 'hubless' configuration.

Although the 3D printing layer resolution was kept low (in the scale of micrometers), no in depth surface roughness study was performed in this project. Future work should study the roughness of the materials to establish manufacturing control metrics for future prototypes. Similarly, no biomaterials were used during the manufacturing process, therefore, hemocompatibility and RBC damage assessment were out of the scope of this thesis.

Eventually, a metallic model of the most promising pump configuration should be developed for hemolysis assessment. Biomaterials for blood-contacting surfaces, such as the ones mentioned in the literature review, and the lost-wax casting approach for prototype development should be explored to produce a durable metallic prototype using the already acquired MAX2 wax 3D printer (Solidscape Inc., New Hampshire, USA).

Although numerical solutions converged to RMS error values $< 10^{-5}$, no mesh independence study was performed. Future designers should perform a mesh independence study to guarantee independency between the numerical results and the mesh element size.

Virtual testing was limited by the hardware resources. The combination of an SST turbulence model, the frozen rotor rotating model, the number of rotations and iterations per simulation turned the model into a complex problem. Therefore, the use of a supercomputer could considerably reduce the time taken to run simulations since an iterative design-testing procedure is required for pump optimization.

The fluid in both numerical simulations and experiments was modeled as a Newtonian fluid, even though this assumption is acceptable at high shear-stresses. The use of a non-Newtonian blood model for virtual and experimental tests could better predict hemodynamics of blood when exposed to the device.

Due to time constraints, experimental tests of only Design A were performed, and no physical prototype of Design B was constructed. Therefore, the experimental study of Design B could increase the accuracy and trustworthiness of results.

Physical experiments were restrained to rotational speeds N up to 418.87 rad s^{-1} due to the motor's limitations. Therefore, for future tests, experimenters should consider the use of a brushless motor to replicate numerical results at N= 628.31 rad s^{-1} and 837.75 rad s^{-1}.

Similarly, the use of similarity laws could facilitate the optimization procedure since pump performance results at one rotation speed could help predict the performance curves of the pump at another speed or could ease determining the effects of changing the overall pump diameter for pump performance predictions of scaled up or down prototypes.

The use of Particle Image Velocimetry (PIV) in vitro experiments can help to elaborate more detailed understanding of the complications that might occur in the flow field of the proposed 'hubless' configuration by studying and simultaneously validating CFD fluid characteristics. For this reason, the refractive index of the transparent prototypes should be studied to match the test fluid to allow optical accessibility. A more sophisticated test-rig system should be developed to account for the PIV equipment (i.e.: laser, cylindrical lense, high-speed camera, synchronizer, and data acquisition software and computer).

Lastly, all in-vitro experiments were performed in steady-state conditions, and the native heart anatomy and physiological pulsatility were omitted at this stage of design. However, the exploration of the pump performance in a dynamic environment (pulsatile behaviour) is crucial for an accurate prediction of the changes in the aortic root, sinus compliance, and to examine any other events that could occur when the pump is operating, such as suction events or aortic valve insufficiency. Hence, the incorporation of pulsatile conditions in the test-rig would be an important next step, acknowledging the fact that dynamic pulsatility of the heart shall be still accounted in LVAD support mechanisms.

CHAPTER 6: CONCLUSION

An unmet need in the field of mechanical circulatory support is the inherent mechanical damage to blood cells when in contact with left ventricular assist devices. However, the shear stresses linked to blood trauma can be minimized by exploring different LVAD geometries and configurations.

The present thesis explores the development and early testing of a novel axial LVAD configuration characteristic by an outer blade mount aimed to provide long-term therapy for patients with heart failure.

The blade parameters of the pump were defined using a turbomachinery software that combines theoretical equations and empirical correlations. The STL files of the previously described pump geometry were generated to create a physical prototype of pump using PLA and SLA 3D printers.

Combining CFD-based computational models and experimental studies, the hydraulic performance characterization of the pump was evaluated. Results prove the hypothesis since the 'hubless' pump provided circulatory support flow rates Q of $8.33 \text{ x } 10^{-6}$ m s^{-3} to $5.83 \text{ x } 10^{-5}$ m s^{-3} are experimentally achieved at significant lower rotational speeds than conventional continuous rotary axial-flow blood pumps. However, numerical and experimental predictions of pressure rise ΔP demonstrate that the pump performed below the desired DOP. Therefore, further exploration of blade parameters and scaled models could bring the performance to an optimal operating region.

This study is a starting point for pump optimization and future development stages. It is believed that with design optimization, the hubless LVAD concept can potentially offer heart failure patients a fully, minimally-invasive, biocompatible solution for long-term therapy.

APPENDIX A. Mesh Quality of the Numerical Simulations

Mesh quality of the simulations was evaluated in terms of Aspect Ratio, Skewness, and Orthogonal Quality using ANSYS mesh control metrics. Aspect Ratio measures how stretched elements in a fluid domain are and aspect ratios below 100 are desirable and values closer to 1 are ideal as they represent an equilateral cell shape. Skewness is the difference between the shape of a cell and the shape of an equilateral cell with similar volume. Highly skewed elements (i.e.: values closer to 1) decrease reliability of the solver and complicate convergency, therefore skewed cell with values closer to 0 are desirable. Orthogonal Quality refers to the measurement alignment (angle) between the normal vector on a face and the normal vector from node to node of the same cell. Orthogonal Quality values closer to 0 are not desirable as they affect convergency and values closer to 1 are ideal. Table A 1 and Table A 2 shows the skewness and orthogonal quality spectrum, respectively, and their respective mesh quality characteristic.

Table A 1 Skewness quality spectrum

Skewness value	Mesh quality
0-0.25	Excellent
0.25-0.5	Very Good
0.5-0.8	Good
0.8-0.94	Acceptable
0.95-0.97	Bad
0.98-1.00	Unacceptable

Table A 2 Orthogonal Quality spectrum

Orthogonal quality value	Mesh quality
.95-1.00	Excellent
0.70-0.95	Very Good
0.20-0.69	Good
0.15-0.20	Acceptable
0.001-0.14	Bad
0-0.001	Unacceptable

Table A 3 shows the average values and standard deviation of Aspect Ratio, Skewness, and Orthogonal Quality for Design A and B and figures A1 and A2 show the cell distributions over the mesh control metrics spectrum of Design A and Design B, respectively.

Table A 3 Mesh quality of Design A and Design B

	Design A			Design B		
Parameter	Aspect Ratio	Skewness	Orthogonal Quality	Aspect Ratio	Skewness	Orthogonal Quality
Average	2.07	0.265	0.85	2.07	0.265	0.85
Standard Deviation	1.17	0.15	0.11	1.17	0.15	0.11

A.

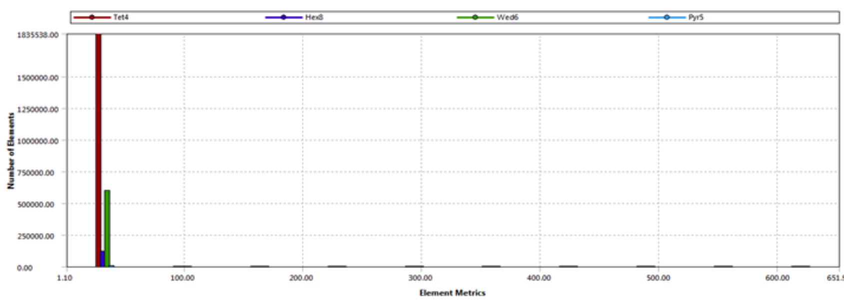

B.

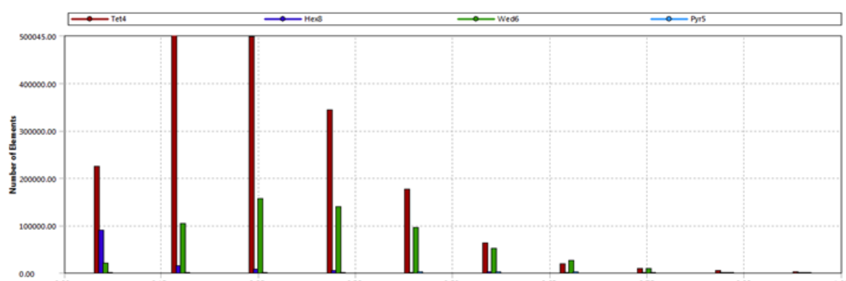

C.

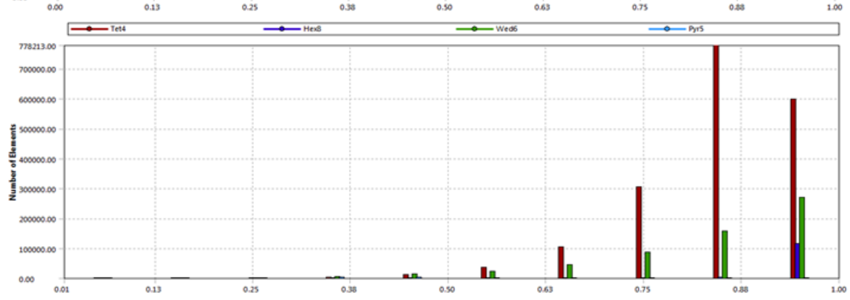

Figure A1 Mesh elements distribution of Design A in terms of (A) Aspect Ratio. (B) Skewness. (C) Orthogonal Quality.

A.

B.

C.

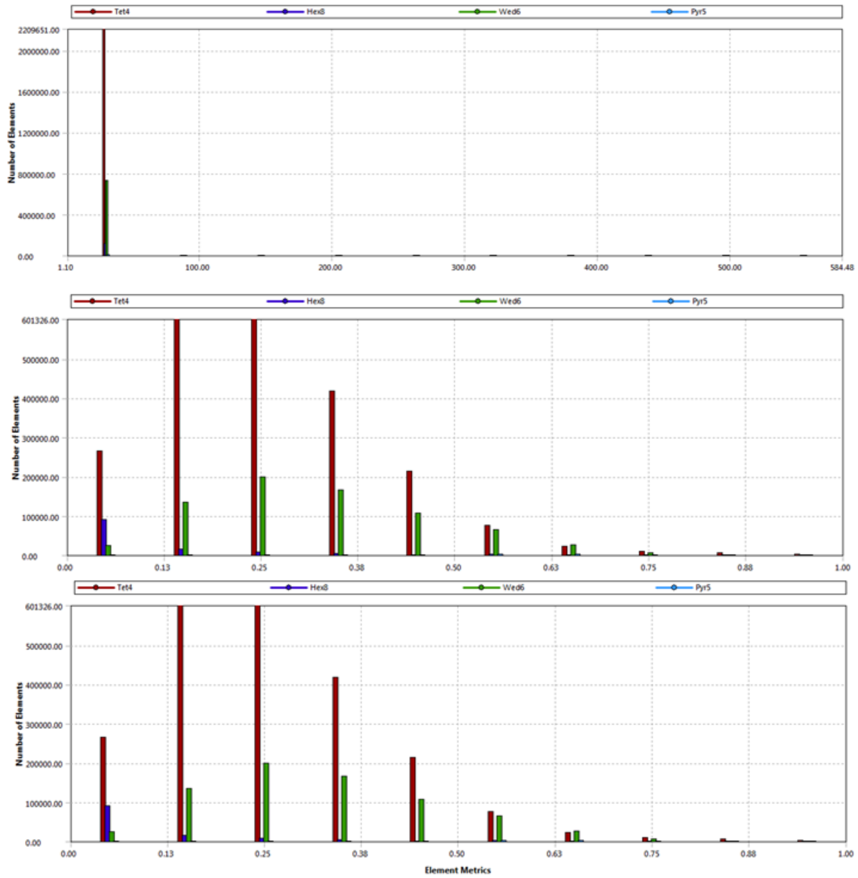

Figure A2 Mesh elements distribution of Design B in terms of (A) Aspect Ratio. (B) Skewness. (C) Orthogonal Quality.

APPENDIX B. Motor Speed and Feedback Controller.

The Gain (Km) and time (τ) constants of the transfer function of the DC motor: $G(s) = \frac{\mathrm{Km}}{\mathrm{s}+\tau}$ were obtained using the linear Least Squares Method (LSM). To this end, the motor speed (rad/sec and the input voltage (volts) were acquired to specify the motor speed-input voltage relation. Speed and voltage measurements were taken using the LM393 sensor reading from the Arduino and a multimeter, respectively. Figure B1 shows the motor speed at no-load condition for a given input voltage.

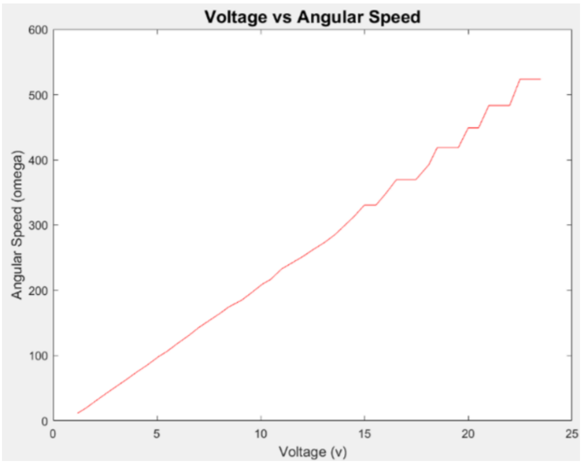

Figure B1 Voltage-angular speed relation of the DC motor at no-load condition.

Applying the LSM:

$$\mathrm{G(s)} = \frac{\mathrm{Km}}{\tau\,\mathrm{s}+1}$$

$$\frac{\omega(s)}{v(s)} = \frac{\mathrm{Km}}{\tau\,\mathrm{s}+1}$$

$$\omega(s) = \frac{\mathrm{Km}\,v(s)}{\tau\,\mathrm{s}+1}$$

$$\omega(s) * (\mathrm{s}+\tau) = \mathrm{Km}\,v(s)$$

$$\mathrm{s}\,\omega(s) + \tau\,\omega(s) = \mathrm{Km}\,v(s)$$

$$\mathrm{s}\,\omega(s) = \mathrm{Km}\,v(s) - \tau\,\omega(s)$$

$$\omega(i) - \omega(i-1) = \mathrm{Km}\,v(i) - \tau\,\omega(i)$$

$$\begin{bmatrix} v(i) & \omega(i) \\ \vdots & \vdots \end{bmatrix} \begin{bmatrix} \mathrm{Km} \\ -\tau \end{bmatrix} = \begin{bmatrix} \omega(i) - \omega(i-1) \\ \vdots \end{bmatrix}$$

Where

$$\begin{bmatrix} v(i) & \omega(i) \\ \vdots & \vdots \end{bmatrix} = A$$

$$\begin{bmatrix} \mathrm{Km} \\ -\tau \end{bmatrix} = x$$

$$\begin{bmatrix} \omega(i) - \omega(i-1) \\ \vdots \end{bmatrix} = b$$

$$x = (A.A^T)^{-1}.A^T.b$$

We get a transfer function of

$$\mathrm{G(s)} = \frac{2.51990039}{\mathrm{s} + 0.082001677}$$

Having defined the motor's transfer function, the PID autotuning tool of Simulink was used perform experimental frequency-response estimations (Fig. B2) based on the PID autotuner blocks (Fig. B3):

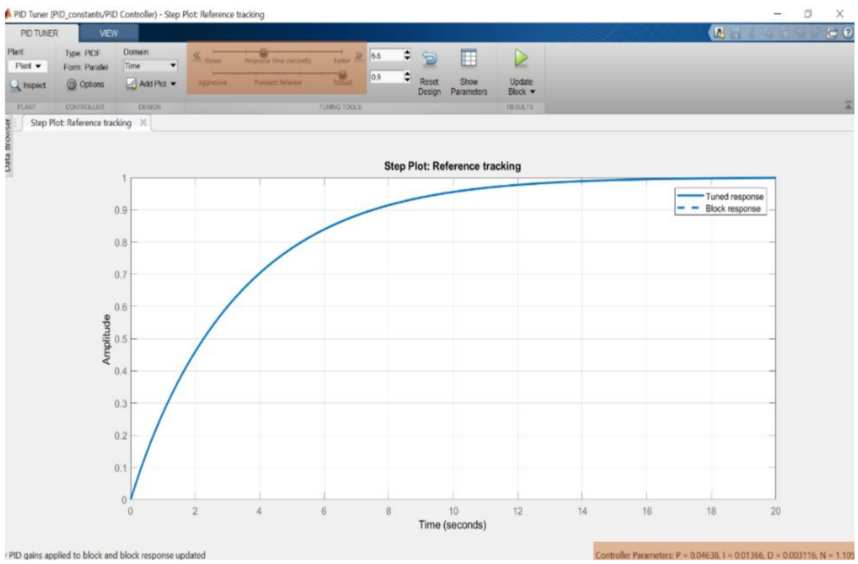

Figure B2 Simulink PID Autotuning tool used to find the PID constants for the motor speed controller.

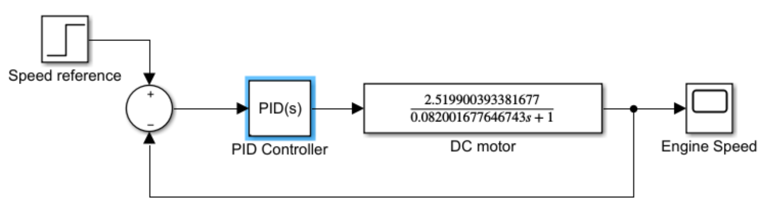

Figure B3 Simulink Speed PID Autotuner block diagram.

The experimental estimations were tested with different sets of PID constants (previously defined through the frequency-response panel of Simulink). The constants were incorporated into the Arduino speed code using the <PID_v1.h> Arduino library.

Figure B4 shows the comparison between the measured speed (blue) and the predetermined set point of 2000 RPM (red). The final chosen PID constants to be included in the speed control system (Kp = 0.0384, ki = 0.0110, kd =0) were selected as a result of the error E quantification between the real speed (Set Point) and the measured speed (feedback signal) $E = \frac{Feedback\ Signal - Set\ Point}{Set\ Point}$.

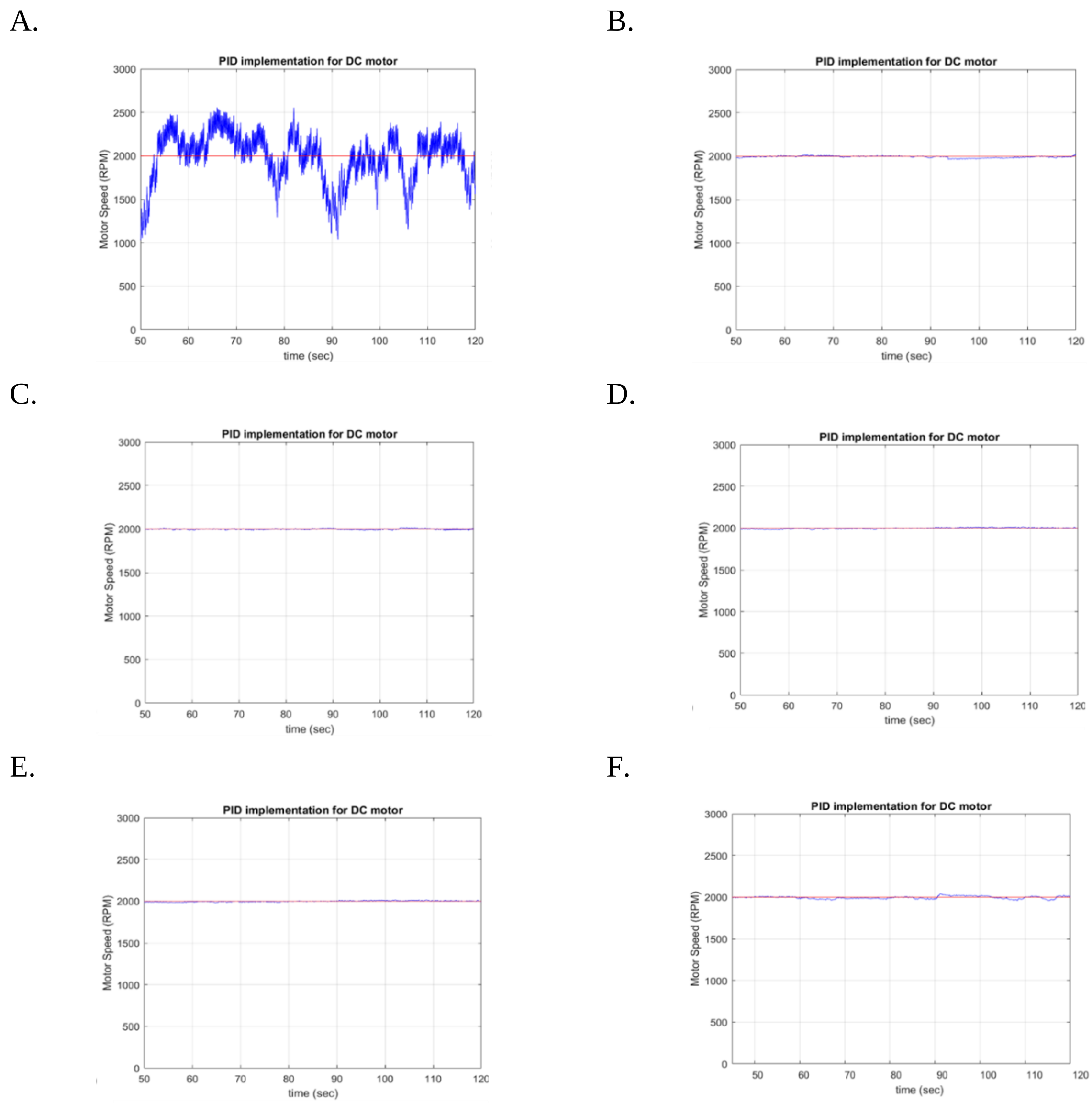

Figure B4 Motor control behaviour with PID constants of (A) kp=0.0594, ki=0.0191, kd=0.6881. $\bar{X}$: 1979.8 RPM, Error: 1.0113. (B) Motor control behaviour at kp=0.0470, ki=0.0139, kd=0.0039. $\bar{X}$: 1994.6 RPM, Error: 0.27. (C) Motor control behaviour at kp=0.0445, ki=0.0132 , kd=0. $\bar{X}$: 1998.6 RPM, Error: 0.070. (D) Motor control behaviour at kp =0.0463, ki=0.0136, kd=0.0031. $\bar{X}$: 1998.7

RPM, Error: 0.065. (E) kp=0.0384, ki=0.01105 , kd =0. $\bar{X}$: 1999.7 RPM, Error: 0.015. (F) Motor control behaviour at kp=0.0307, ki=0.0088, kd =0. $\bar{X}$: 1991.2 RPM, Error: 0.44

Kp = 0.0384, ki = 0.0110, kd =0 were selected as default PID constants since they produce the least error (0.015%) between the real and measured value at 2000 RPM.

Arduino PID speed control code:

```
#include <Servo.h>
#include <PID_v1.h>
volatile unsigned long MicrosecondsPerRevolution = 0;
const unsigned long MicrosecondsPerMinute = 60UL * 1000000UL;
Servo myservo;
double Input, Setpoint, Output;
const double kp = 0.03846153846153846153846153846153846384, ki = 0.01105 , kd =0;
PID myPID(&Input, &Output, &Setpoint, kp, ki, kd, DIRECT);
void docount(){ /* take time to make one turn from the speed sensor */
static unsigned long isrMicros = 0; //take the time taken to make one turn (ms)
unsigned long currentMicros = micros();
unsigned long delta = currentMicros - isrMicros;
if (delta > 5000) { // Skip signal bounces
MicrosecondsPerRevolution = currentMicros - isrMicros;
isrMicros = currentMicros; }}
void setup(){
Serial.begin(9600);
attachInterrupt(2, docount, FALLING);
myservo.attach(9);
Setpoint = 2000.0; //desired speed value to keep RPMsRPM
RPM
myPID.SetOutputLimits(1501.0, 2000.0);  // range for servo.writeMicroseconds()
myPID.SetMode(AUTOMATIC); } //turn PID on
void loop(){
static unsigned long outputTimer = 0;
```

```
noInterrupts();  // Grab volatile data with
unsigned long microsecondsPerRevolution = MicrosecondsPerRevolution;
interrupts();
Input = MicrosecondsPerMinute / microsecondsPerRevolution;  //  RPM
myPID.Compute();
  myservo.writeMicroseconds((int)Output);//  Report status every five seconds
  if (outputTimer - millis() >= 5000){
  outputTimer = millis();
  Serial.println(Input);  }
  delay(1);}
```

APPENDIX C. Experimental Protocol for Experiments

Prior to experiments, initial calibration should be made to the instrumentation device (e.g.: pressure control unit and flow meter). Therefore, the experimental protocol has been divided into two phases:

(Phase I) Equipment Calibration	**(Phase II)** Experimental Procedure and data collection

I. Equipment Calibration procedure:

a. Pressure Calibration (SPR-524 Mikro-Tip ®, Millar Instruments Inc.)

(Approximate Duration: 45 min)

1) Presoak the pressure sensor in sterile water or sterile saline water for 30 minutes prior use to minimize the drift.
2) Connect each pressure catheter to the dual channel pressure control unit (PCU-2000, Millar) of figure C1 through the input channels located at the back of the unit.

Figure C1 Pressure Control Unit (PCU).

3) Connect the output channels of the pressure control unit (PCU-2000, Millar) to the data acquisition card (USB-6008, Texas Instruments) using universal 1/4” mono plug TS cable adaptors.
4) Connect the data acquisition card to a computer where the LabView 2016 software is installed.

5) Open the DAS-hydraulic-system.vi program through the LabView 2016 software and make sure that the data acquisition card is detected through the LabView DAQ driver.

The following *Front panel* (Fig. C2) should appear on the screen:

Figure C2 LabView front monitoring panel.

6) Open the *Block Diagram* (Fig. C3) in the menu bar as following: Window/Show Block Diagram.

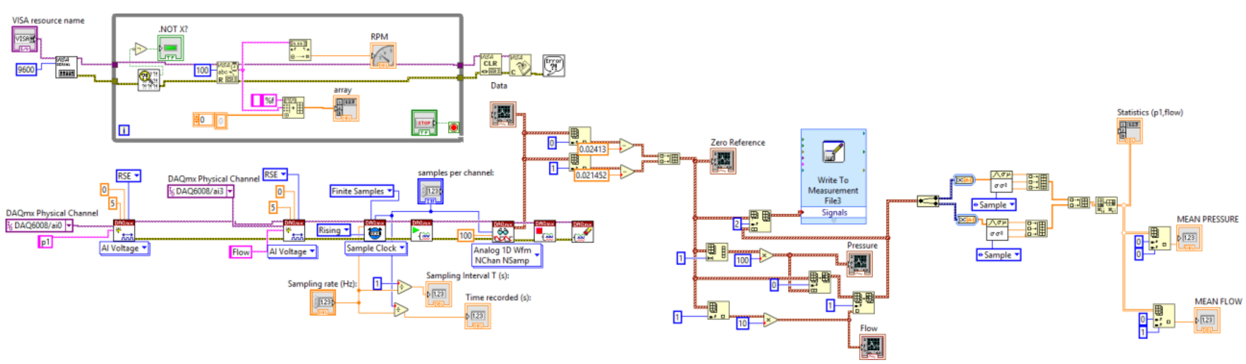

Figure C3 Block diagram of the Data Acquisition Interface.

7) Turn the pressure control unit function switch to STANDBY 0.

8) As the measurements will be taken as mean values of continuous measurements, adjust the time recorded to be at least 10 seconds by changing the sample rate and the sampling rate in the front panel.

9) Click on Run in the *Front Panel* to adjust the **Zero Reference** plot.

10) Subtract the offset value that appears in the *Front Panel* **Data** plot of pressure by changing the subtraction value in the *Block Diagram* panel as shown in figure C4.

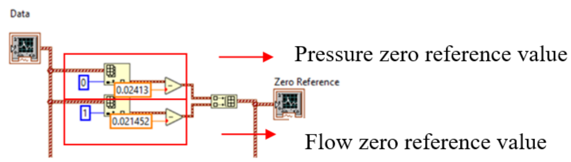

Figure C4 LabView monitor adjustment values to zero baseline.

11) Click Run in the *Front Panel* to verify a **Zero Reference** plot of pressure of 0.

12) Submerge the pressure sensor in a saline solution (Terg-A-Zyme, Alconox, INC.) just below the end of the transducer tip and shield from ambient light.

13) Turn the pressure control unit function switch to TRANSDUCER

14) Adjust the TRANSDUCER BALANCE control on the pressure control unit to the same zero baseline as Step 11.

15) After obtaining the desired zero baseline, activate the catheter balance locking mechanism by moving it to the LOCK position.

16) *Data Validation:* Connect the pressure catheter tip to the syringe and pressure gauge system for data validation (Fig. C5)

Figure C5 Pressure data validation system showing the connection in parallel between the pressure sensor and the mechanical manometer.

17) Apply pressure with the syringe and observe the pressure gauge (manometer) reading.

18) Click Run ➪ in the *Front Panel* and verify the readings comparing the values to the ones obtained in the manometer.

19) Place the pressure catheters to the inlet and outlet of the pump.

b. Flow Probe Calibration (EP690, Carolina Medical)

Duration: 60 minutes

1) Soak the flow probe in a saline solution (Terg-A-Zyme, Alconox, INC.) for 15-30 minutes for electrode conditioning.

2) Rinse the flow probe thoroughly in distilled water and dry before its use.

3) Place the flow probe the outlet of the test pump, the peristaltic pump (Masterflex L/S) and the calibration flow tubing (L/S 36 MasterFlex tubing). Use gradual reducer fittings, clamps and abrasion-resistant gum rubber tubing (5546K53, McMaster) to avoid leaks between the connected parts.

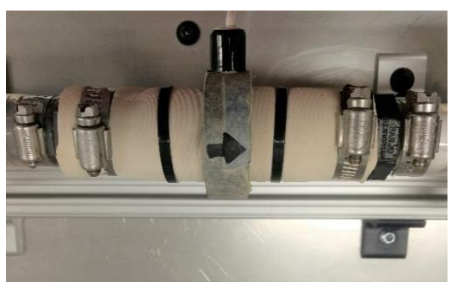

Figure C6 Flow probe connection at the outlet of the test pump.

4) Close the ON/OFF ball valve located at the outlet of the reservoir.

5) Place the stainless-steel ring end of the ground cable of the flowmeter inside the reservoir.

6) Connect the electronic end of the ground cable to the flowmeter. Figure C7 shows the ground cable.

Figure C7 Flowmeter ground cable.

7) Make sure that the flowmeter (501D, Carolina Medical, North Carolina, USA) POWER and PROBE switches are OFF.

8) Fill the reservoir with 7 liters of blood analog solution (37% glycerine in water) and mix the solution with 100 grams of salt as the electrodes of the flow probe should be in contact with a conductive liquid. The viscosity of the fluid can be validated using the Ubbelohde Viscometer (SK-98934-12, Cole Palmer, Illinois, USA) at ambient temperature.

9) Open the ON/OFF valve.

10) Set the peristaltic pump to 1000 ml/min and let the fluid circulate clockwise if the mock circulatory loop is looked from above.
NOTE: During experiments, the peristaltic pump is only used during the priming procedure (take out the bubbles trapped in the fluid); and during calibration is only used as a flow reference to adjust the gain of the flow probe using the flowmeter (501D, Carolina Medical, North Carolina, USA).

11) Make sure that the circulatory loop is fully primed.

12) Turn off the peristaltic pump, OFF, but do not open the handle that creates resistance on the L/S 36 Masterflex tubing.

13) Connect the PLUS output (located on the rear chassis of the flowmeter) to the data acquisition card (USB-6008, Texas Instruments) using a universal 1/4” mono plug TS cable adaptor.

14) Turn the POWER switch of the flowmeter on. If the ALARM lamp is ON, press the ALARM indicator to reset the alarm circuit.

15) Set the PULSATILE Hz RESPONSE control in the flowmeter to 30 and the MEAN to LO (these controls determine the frequency response of the flowmeter).

16) Set the display meter of the flowmeter to zero with the ZERO control. The ZERO control sets the “no-signal” level of the mean and pulsatile outputs and the meter.

17) Set the monitor to the zero-flow baseline by repeating steps 4 to 6 and 9 to 11 steps of the Pressure Catheter Calibration procedure but considering the flow line in the **Data** plot and subtracting flow in the *Block Diagram* Panel.

18) Simultaneously apply and hold either 1 VOLT or 0.01 VOLT calibration signal through the flowmeter and run the LabVIEW program to validate the readings in the **Flow** plot (*Front Panel*).

19) Set the BALANCE control of the flowmeter to 500.

20) Set the PROBE FACTOR to 568 as indicated in the Blood flow probe calibration sheet (Fig C8) and the RANGE control to C-LO.

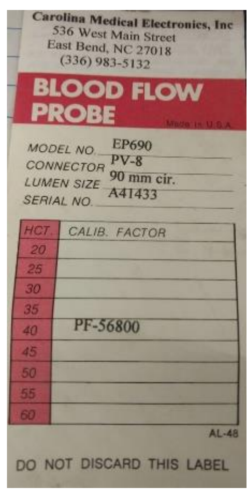

Figure C8 Flow probe calibration sheet.

21) Turn the PROBE switch to NULL. Adjust the NULL control until the display indicates the minimum reading. Next turn the PROBE switch to BAL position and adjust the meter to zero with the BALANCE control.

These two-adjustment set up the zero-flow reference. Next turn the PROBE switch on to +. Figure C9 provides a front view of the flowmeter.

Figure C9 501D flowmeter (Front view).

22) If the flowmeter does not indicate zero when the PROBE switch is set to +, reset it to zero with the BALANCE control.

23) Move the arrows of the peristaltic pump until the displayed value is 1500 ml/min and turn it ON.

24) Once the fluid starts to circulate, wait 3 minutes to stabilize the flow, and read the values on the display of the flowmeter.

25) If the value indicated on the flowmeter is not the same as the peristaltic pump, adjust the BALANCE control of the flowmeter until the value displayed is similar to the one in the peristaltic pump

26) Turn the peristaltic pump OFF and wait 5 minutes to reach the zero value on the flowmeter display.

27) Repeat steps 22 to 25 three to five times to verify the readings on the flowmeter.

28) Once the lectures are within the ± 3 % of error the flow probe is ready for use.

29) Open the handle of the peristaltic pump and adjust the ZERO control of the flowmeter to 0 to eliminate the offset of the resistance imposed by the peristaltic pump.

II. Experimental In-Vitro Protocol

Objective: measure the performance curves of the axial LVAD configuration.

a. Perform the initial calibration run of Phase I.
b. Connect the torque sensor to the torque meter and turn the unit ON.
c. Set the desired RPM in the Arduino code and compile the code into the board.
d. Connect the Arduino PWM signal to the HB 25 motor controller.
e. Connect the HB 25 controller to a +15 V power source and to the motor terminals.
f. Make sure that the hydraulic gate valve is fully opened, that the rig is fully primed and that the power transmission system is properly aligned and correctly adjusted on the LVAD prototype embodiment.
g. Turn the power source ON and compare the speed measurements of the motor using the LabView *Front Panel* values and a digital tachometer.
h. Let the pump run for 2 minutes to let the speed stabilize.
i. Set a sampling rate in the LabView *Front Panel* acquire n numbers.
   NOTE: The mean value is the average of all those samples.
j. Click RUN on the LabView *Front Panel* to obtain mean values of pressure rise, flow rate and speed and simultaneously record the displayed torque value of the torque meter.
k. Close the gate ½ of a turn to acquire another data point.
l. Repeat step i to record the four variables (pressure rise, flow rate, speed and torque) at a different valve setting.
m. Repeat step j and i as many times as needed to reach a fully closed position (i.e.: to run the pump over its full performance range).
n. Turn the power source OFF.
o. Open the gate valve.
p. Store data and compute HQ and η curves.
q. Make a plot of pressure rise and η (y axis) versus flow rate (X axis).

APPENDIX D. LabView Block Diagram for Data Acquisition

Image D1 shows the block diagram schematic of the LabView Software developed to acquire data from the pressure sensors, flow probe and rotational speed control of the motor. The blue square represents the microcontroller communication with Arduino to display the rotational speed simultaneously to the pressure and flow measurements. The orange square represents the voltage input to the DAQ coming from the pressure sensors and flow probe. The green square represents the mathematical zero reference for the pressure sensors and the flow probe to adjust for offset values. The dark blue square represents the conversion between voltage output signal to respective units of measurement for both, pressure sensors and the flow probe. The yellow square shows the statistics acquired from the continuous data acquisition for mean values (discrete data) acquisition.

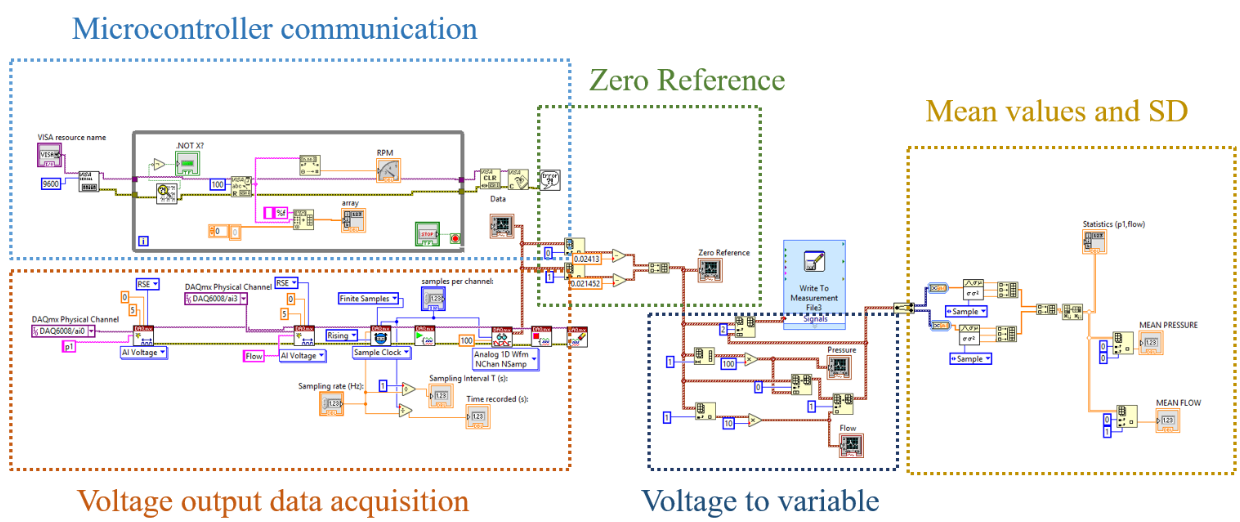

Figure D1 Detailed LabView block diagram.

APPENDIX E. List of Units Conversion

The following list shows the unit conversion of the biomechanics variables of interest in this thesis

Pressure:

133.322 Pa = 1 mmHg

Flow rate:

$$1\ m^3\ s^{-1} = 60000\ L\ min^{-1}$$

Rotational Speed:

$$1\ rad\ s^{-1} = \frac{60}{2\ \pi}\ RPM$$

Viscosity:

$$1\ \text{Pa s} = 1000\ \text{cP}$$

REFERENCES

[1] Cecere, R., Chung, Y. H., Mongrain, R., and Azar, T., 2017, "Axial Flow Blood Pump," US Patent 9,726,195 B2.

[2] Mongrain, R., Chung, Y., Azar, T., and Cecere, R., 2017, "Development of a New Hubless Ventricular Assist Device," *Proceedings of the 7th International Conference on Mechanics and Materials in Design*, Portugal, pp. 1565-1569.

[3] Chung, Y., Cecere, R., Mongrain, R., and Azar, T., 2016, "A novel dual-angle blade, coreless Ventricular Assist Device," Canadian Journal of Cardiology, **32**(10), pp. S173.

[4] Hall, J., and Guyton, A., 2016, *Guyton and Hall textbook of medical physiology*, Elsevier, Philadelphia, US

[5] Elmoselhi, A., 2018, *Cardiology : an integrated approach*, McGraw-Hill Education, New York, US

[6] Gregory, S., Stevens, M., and Fraser, J., 2017, *Mechanical circulatory and respiratory support*, Academic Press, London, UK.

[7] Institute of Medicine (US) Committee on Social Security Cardiovascular Disability Criteria, 2010, "Cardiovascular Disability: Updating the Social Security Listings," National Academies Press, Washington, US.

[8] Benjamin, E., Virani, S., Callaway, C., Chamberlain, A., Chang, A., Cheng, S., Chiuve, S., Cushman, M., Delling, F. N., Deo, R., de Ferranti, S., Ferguson, J., Fornage, M., Gillespie, C., Isasi, C., Jimenez, M., Jordan, L., Judd, S. E., Lackland, D., Lichtman, J., Lisabeth, L., Liu, S., Longenecker, C., Lutsey, P., Mackey, J., Matchar, D., Matsushita, K., Mussolino, M., Nasir, K., O'Flaherty, M., Palaniappan, L., Pandey, A., Pandey, D., Reeves, M., Ritchey, M., Rodriguez, C., Roth, G., Rosamond, W., Sampson, U., Satou, G., Shah, S., Spartano, N., Tirschwell, D., Tsao, C., Voeks, J., Willey, J., Wilkins, J., Wu, J., Alger, H., Wong, S., and Muntner, P., 2018, "Heart Disease and Stroke Statistics—2018 Update: A Report From the American Heart Association," Circulation Journal, **137**(12), pp. e67-e492.

[9] National Heart Lung and Blood Institute, 2018, "Heart Failure, Also known as Congestive heart failure," from https://www.nhlbi.nih.gov/health-topics/heart-failure.

[10] Bui, A., Horwich, T., and Fonarow, G., 2011, "Epidemiology and risk profile of heart failure," Nature reviews. Cardiology, **8**(1), pp. 30-41.

[11] Savarese, G., and Lund, L., 2017, "Global Public Health Burden of Heart Failure," Cardiac failure review, **3**(1), pp. 7-11.

[12] Canadian Heart Failure Network, 2011, "Facts about heart failure in Canada:Cardiovascular Disease and Mortality," from http://www.chfn.ca/facts_about_chf_in_canada.

[13] Díez-Villanueva, P., and Alfonso, F., 2016, "Heart failure in the elderly," Journal of Geriatric Cardiology, **13**(2), pp. 115-117.

[14] Heidenreich, P., Albert, N., Allen, L., Bluemke, D., Butler, J., Fonarow, G., Ikonomidis, J., Khavjou, O., Konstam, M., Maddox, T., Nichol, G., Pham, M., Pina, I. L., and Trogdon, J., 2013, "Forecasting the impact of heart failure in the United States: a policy statement from the American Heart Association," Circulation Journal: Heart failure, **6**(3), pp. 606-619.

[15] Strait, J., and Lakatta, E., 2012, "Aging-associated cardiovascular changes and their relationship to heart failure," Heart Failure Clinics Journal, **8**(1), pp. 143-164.

[16] American Heart Association (AHA), 2018, "Classes of Heart Failure ", from https://www.cdc.gov/heartdisease/facts.htm.

[17] Friedrich, E., and Böhm, M., 2007, "Management of end stage heart failure," Heart Journal, **93**(5), pp. 626-631.
[18] Timms, D., 2005, "Design, development and evaluation of Centrifugal Ventricular Assist Devices," Ph.D. Thesis, Queensland University of Technology.
[19] Canadian Institute for Health Information, 2017, "Canadian Organ Replacement Register (CORR) Annual Statistics Report", CIHI, Ottawa, CA.
[20] Goldstein, B., Thomas, L., Zaroff, J., Nguyen, J., Menza, R., and Khush, K., 2016, "Assessment of heart transplant waitlist time and pre- and post-transplant failure: A mixed methods approach," Epidemiology Journal, **27**(4), pp. 469-476.
[21] US Department of Health and Human Services, "Organ Procurement and Transplantation Network," Virginia US.
[22] Hsich, E., 2016, "Matching the Market for Heart Transplantation," Circulation Journal: Heart failure, **9**(4), pp. e002679.
[23] National Institutes of Health, 2011, "The Adrian Kantrowitz Papers, Replacing Hearts: Left Ventricle Assist Devices and Transplants, 1960-1970: Documents," from https://profiles.nlm.nih.gov/ps/retrieve/Narrative/GN/p-nid/315.
[24] DeBakey, M., 1971, "Left ventricular bypass pump for cardiac assistance.," The American Journal of Cardiology, **27**(1), pp. 3-11.
[25] Holman, W., 2012, "Interagency Registry for Mechanically Assisted Circulatory Support (INTERMACS)," Circulation Journal, **126**(11), pp. 1401-1406.
[26] Kirklin, J., and Naftel, D., 2008, "Mechanical circulatory support: registering a therapy in evolution," Circulation Journal: Heart failure, **1**(3), pp. 200-205.
[27] Norman, J., Brook, M., Cooley, D., Klima, T., Kahan, B., Frazier, O., Keats, A., Hacker, J., Massin, E., Duncan, J., Solis, R. T., Dacso, C., Luper, W., Winston, D., and Reul, G., 1978, "Total support of the circulation of a patient with post-cardiotomy stone-heart syndrome by a partial artificial heart (ALVAD) for 5 days followed by heart and kidney transplantation," The Lancet Journal, **1**(8074), pp. 1125-1127.
[28] Rose, E., Gelijns, A., Moskowitz, A., Heitjan, D., Stevenson, L., Dembitsky, W., Long, J. W., Ascheim, D. D., Tierney, A. R., Levitan, R. G., Watson, J. T., Meier, P., Ronan, N. S., Shapiro, P. A., Lazar, R. M., Miller, L. W., Gupta, L., Frazier, O. H., Desvigne-Nickens, P., Oz, M. C., and Poirier, V. L., 2001, "Long-term use of a left ventricular assist device for end-stage heart failure," The New England Journal of Medicine, **345**(20), pp. 1435-1443.
[29] Frazier, O., Wampler, R., Duncan, J., Dear, W., Macris, M., Parnis, S., and Fuqua, J., 1990, "First human use of the Hemopump, a catheter-mounted ventricular assist device," The Annals of Thoracic Surgery, **49**(2), pp. 299-304.
[30] Mayo Clinic, 2019, "Left ventricular assist device (LVAD)," from https://www.mayoclinic.org/tests-procedures/ventricular-assist-device/multimedia/left-ventricular-assist-device/img-20006714.
[31] Peng, W., 2008, *Fundamentals of turbomachinery*, *John Wiley* & Sons, Inc, New Jersey, US.
[32] Slaughter , M., Rogers , J., Milano , C., Russell , S., Conte , J., Feldman , D., Sun , B., Tatooles, A., Delgado , R., Long , J., Wozniak , T., Ghumman , W., Farrar , D., and Frazier , H., 2009, "Advanced Heart Failure Treated with Continuous-Flow Left Ventricular Assist Device," New England Journal of Medicine, **361**(23), pp. 2241-2251.
[33] Meyer, A., Kuehn, C., Weidemann, J., Malehsa, D., Bara, C., Fischer, S., Haverich, A., and Strüber, M., 2008, "Thrombus formation in a HeartMate II left ventricular assist device," The Journal of Thoracic and Cardiovascular Surgery, **135**(1), pp. 203-204.

[34] Rothenburger, M., Wilhelm, M., Hammel, D., Schmidt, C., Tjan, T. D., Bocker, D., Scheld, H., and Schmid, C., 2002, "Treatment of thrombus formation associated with the MicroMed DeBakey VAD using recombinant tissue plasminogen activator," Circulation Journal, **106**(12 Suppl 1), pp. I189-192.
[35] US Food and Drug Administration (FDA), 2018, "HeartMate 3 Left Ventricular Assist System (LVAS) - P160054/S008," from https://www.fda.gov/MedicalDevices/ProductsandMedicalProcedures/DeviceApprovalsandClearances/Recently-ApprovedDevices/ucm624155.htm.
[36] Abbott Laboratories, 2019, "HeartMate 3™ LVAD now approved for DT," from https://www.heartmate.com/healthcare-provider/heartmate-3-lvad.
[37] Rodriguez, L., Suarez, E., Loebe, M., and Bruckner, B., 2013, "Ventricular assist devices (VAD) therapy: new technology, new hope?," Methodist DeBakey Cardiovascular Journal, **9**(1), pp. 32-37.
[38] F. Dorman and P. Bernstein and L. Blackshear, 1969, "Implantable blood pump," US Patent 3608088A.
[39] Mehra, M., Goldstein, D., Uriel, N., Cleveland, J., Yuzefpolskaya, M., Salerno, C., Walsh, M., Milano, C., Patel, C., Ewald, G., Itoh, A., Dean, D., Krishnamoorthy, A., Cotts, W. G., Tatooles, A. J., Jorde, U. P., Bruckner, B. A., Estep, J. D., Jeevanandam, V., Sayer, G., Horstmanshof, D., Long, J. W., Gulati, S., Skipper, E. R., O'Connell, J. B., Heatley, G., Sood, P., and Naka, Y., 2018, "Two-Year Outcomes with a Magnetically Levitated Cardiac Pump in Heart Failure," New England Journal of Medicine, **378**(15), pp. 1386-1395.
[40] Mehra, M., Uriel, N., Naka, Y., Cleveland, J., Yuzefpolskaya, M., Salerno, C. T., Walsh, M. N., Milano, C. A., Patel, C. B., Hutchins, S. W., Ransom, J., Ewald, G. A., Itoh, A., Raval, N. Y., Silvestry, S. C., Cogswell, R., John, R., Bhimaraj, A., Bruckner, B. A., Lowes, B. D., Um, J. Y., Jeevanandam, V., Sayer, G., Mangi, A. A., Molina, E. J., Sheikh, F., Aaronson, K., Pagani, F. D., Cotts, W. G., Tatooles, A. J., Babu, A., Chomsky, D., Katz, J. N., Tessmann, P. B., Dean, D., Krishnamoorthy, A., Chuang, J., Topuria, I., Sood, P., and Goldstein, D. J., 2019, "A Fully Magnetically Levitated Left Ventricular Assist Device — Final Report," New England Journal of Medicine, **380**(17), pp. 1618-1627.
[41] Olia S., 2018, "Design optimization and preclinical testing of pediatric rotary blood pumps and components: towards the pediaflow VAD," Ph.D. Thesis, Department of Bioengineering, University of Pittsburgh.
[42] Baskurt, O., 2007, *Handbook of hemorheology and hemodynamics*, IOS Press, Washington, US.
[43] Bleiziffer, M., 2018, "Development of a new design method for axial propeller-pumps used as Left Venticular Assist Device," Ph.D. Thesis, University of Erlangen-Nuremberg.
[44] Errill, E., 1969, "Rheology of blood," Physiological Reviews, **49**(4), pp. 863-888.
[45] Wiegmann, L., Boes, S., de Zelicourt, D., Thamsen, B., Schmid Daners, M., Meboldt, M., and Kurtcuoglu, V., 2018, "Blood Pump Design Variations and Their Influence on Hydraulic Performance and Indicators of Hemocompatibility," Annals of Biomedical Engineering, **46**(3), pp. 417-428.
[46] Fraser, K., Taskin, E., Griffith, B., and Wu, Z., 2011, "The use of computational fluid dynamics in the development of ventricular assist devices," Medical Engineering & Physics Journal, **33**(3), pp. 263-280.
[47] Giridharan, G., Lederer, C., Berthe, A., Goubergrits, L., Hutzenlaub, J., Slaughter, M., Dowling, R., Spence, P., and Koenig, S., 2011, "Flow dynamics of a novel counterpulsation device

characterized by CFD and PIV modeling," Medical Engineering and Physics Journal, **33**(10), pp. 1193-1202.
[48] Wu, J., Antaki, J., Verkaik, J., Snyder, S., and Ricci, M., 2012, "Computational Fluid Dynamics-Based Design Optimization for an Implantable Miniature Maglev Pediatric Ventricular Assist Device," Journal of Fluids Engineering, **134**(4), pp. 41101-NaN.
[49] Zhang, J., Gellman, B., Koert, A., Dasse, K., Gilbert, R., Griffith, B., and Wu, Z. J., 2006, "Computational and experimental evaluation of the fluid dynamics and hemocompatibility of the CentriMag blood pump," Artificial Organs Journal, **30**(3), pp. 168-177.
[50] Sohrabi, S., and Liu, Y., 2017, "A Cellular Model of Shear-Induced Hemolysis," Artificial Organs Journal, **41**(9), pp. E80-E91.
[51] Leverett, L., Hellums, J., Alfrey, C., and Lynch, E., 1972, "Red blood cell damage by shear stress," Biophysical Journal, **12**(3), pp. 257-273.
[52] ASTM, 2005, "Assessment of Hemolysis in Continuous Flow Blood Pumps," F1841-97.
[53] Bartoli, C., Zhang, D., Kang, J., Hennessy-Strahs, S., Restle, D., Howard, J., Redline, G., Bermudez, C., Atluri, P., and Acker, M., 2018, "Clinical and In Vitro Evidence That Subclinical Hemolysis Contributes to LVAD Thrombosis," Annals of Thoracic Surgery, **105**(3), pp. 807-814.
[54] Bourque, K., Cotter, C., Dague, C., Harjes, D., Dur, O., Duhamel, J., Spink, K., Walsh, K., and Burke, E., 2016, "Design Rationale and Preclinical Evaluation of the HeartMate 3 Left Ventricular Assist System for Hemocompatibility," American Society for Artificial Internal Organs, 62(4), pp. 375-383.
[55] Cowger, J., Romano, M., Shah, P., Shah, N., Mehta, V., Haft, J. W., Aaronson, K., and Pagani, F., 2014, "Hemolysis: a harbinger of adverse outcome after left ventricular assist device implant," Journal of Heart and Lung Transplantation, **33**(1), pp. 35-43.
[56] Malinauskas, R., 1997, "Plasma Hemoglobin Measurement Techniques for the In Vitro Evaluation of Blood Damage Caused by Medical Devices," Artificial Organs, **21**(12), pp. 1255-1267.
[57] Boehning, F., Mejia, T., Schmitz-Rode, T., and Steinseifer, U., 2014, "Hemolysis in a Laminar Flow-Through Couette Shearing Device: An Experimental Study Hemolysis in Couette Shearing Device," Artificial Organs, **38**(9), pp. 761-5.
[58] Paul, R., Apel, J., Klaus, S., Schügner, F., Schwindke, P., and Reul, H., 2003, "Shear Stress Related Blood Damage in Laminar Couette Flow," Artificial Organs, **27**(6), pp. 517-529.
[59] Giersiepen, M., Wurzinger, L., Opitz, R., and Reul, H., 1990, "Estimation of shear stress-related blood damage in heart valve prostheses--in vitro comparison of 25 aortic valves," Artificial Organs, **13**(5), pp. 300-306.
[60] Smith, S., Travers, R., and Morrissey, J., 2015, "How it all starts: Initiation of the clotting cascade," Critical Reviews in Biochemistry and Molecular Biology, **50**(4), pp. 326-336.
[61] Kirklin, J., Pagani, F., Kormos, R., Stevenson, L., Blume, E., Myers, S., Miller, M., Baldwin, J., Young, J., and Naftel, D., 2017, "Eighth annual INTERMACS report: Special focus on framing the impact of adverse events," Journal of Heart and Lung Transplantation, **36**(10), pp. 1080-1086.
[62] Kormos, R., Cowger, J., Pagani, F., Teuteberg, J., Goldstein, D., Jacobs, J., Higgins, R., Stevenson, L., Stehlik, J., Atluri, P., Grady, K., and Kirklin, J., 2019, "The Society of Thoracic Surgeons Intermacs database annual report: Evolving indications, outcomes, and scientific partnerships," Journal of Heart and Lung Transplantation, **38**(2), pp. 114-126.
[63] Legallois, D., and Manrique, A., 2019, "Diagnosis of infection in patients with left ventricular assist device: PET or SPECT?," Journal of Nuclear Cardiology, **26**(1), pp. 56-58.

[64] Leuck, A., 2015, "Left ventricular assist device driveline infections: recent advances and future goals," Journal of Thoracic Disease, 7(12), pp. 2151-2157.

[65] O'Horo, J., Abu, O., Stulak, J., Wilhelm, M., Baddour, L., and Rizwan Sohail, 2018, "Left Ventricular Assist Device Infections: A Systematic Review," American Society for Artificial Internal Organs Journal, **64**(3), pp. 287-294.

[66] Sin, D. C., Kei, H. L., and Miao, X., 2009, "Surface coatings for ventricular assist devices," Expert Review of Medical Devices, **6**(1), pp. 51-60.

[67] Chahal, D., Sepehry, A., Wright, A., and Toma, M., 2017, "The impact of Left Ventricular Assist Device Infections on Post Cardiac Transplant survival: systematic review and meta-analysis.," Canadian Journal of Cardiology, **33**(10), pp. S159.

[68] Grand View Research, 2018, "Ventricular Assist Device Market Size, Share & Trends Analysis Report By Product (LVAD, RVAD), By Type of Flow (Pulsatile, Continuous), By Application, By Region, And Segment Forecasts, 2019 - 2025," from https://www.grandviewresearch.com/industry-analysis/ventricular-assist-devices-market.

[69] Research and Markets, 2017, "Ventricular Assist Device (VAD) Market - Global Industry Analysis, Size, Share, Trends and Forecast, 2014-2022," from https://www.researchandmarkets.com/reports/4085063/ventricular-assist-device-vad-market-global.

[70] Karimov, J., Polakowski, A., Fukamachi, K., and Miyamoto, T., 2019, "Progress in mechanical circulatory support: Challenges and opportunities," Artificial Organs, **43**(9), pp.818-820.

[71] CorWave, 2018, "Neptune: The Next Gen LVAD," from https://www.corwave.com/product/neptune/.

[72] Windmill Cardiovascular Systems, I., 2005, "TORVAD: Toroidal Ventricular Assist Device," from http://www.windmillcvs.com/.

[73] Evaheart Inc., 2014, "EVAHEART: Centrifugal LVAS ", from http://www.evaheart-usa.com/.

[74] Letzen, B., Park, J., Tuzun, Z., and Bonde, P., 2018, "Design and Development of a Miniaturized Percutaneously Deployable Wireless Left Ventricular Assist Device: Early Prototypes and Feasibility Testing," American Society for Artificial Internal Organs Journal, **64**(2), pp. 147-153.

[75] Waters, B., Sample, A., Smith, J., and Bonde, P., 2011, "Toward total implantability using free-range resonant electrical energy delivery system: achieving untethered ventricular assist device operation over large distances," Interventional *Cardiology Clinic*, **29**(4), pp. 609-625.

[76] Waters, B., Smith, J. R., and Bonde, P., 2014, "Innovative Free-range Resonant Electrical Energy Delivery system (FREE-D System) for a ventricular assist device using wireless power," American Society for Artificial Internal Organs Journal, **60**(1), pp. 31-37.

[77] Bocan, K., and Sejdic, E., 2016, "Adaptive Transcutaneous Power Transfer to Implantable Devices: A State of the Art Review," Sensors Journal, **16**(3).

[78] Wang, J., Smith, J., and Bonde, P., 2014, "Energy transmission and power sources for mechanical circulatory support devices to achieve total implantability," Annals of Thoracic Surgery, **97**(4), pp. 1467-1474.

[79] Pya, Y., Maly, J., Bekbossynova, M., Salov, R., Schueler, S., Meyns, B., Kassif, Y., Massetti, M., Zilbershlag, M., and Netuka, I., 2019, "First human use of a wireless coplanar energy transfer coupled with a continuous-flow left ventricular assist device," Journal of Heart and Lung Transplantation, **38**(4), pp. 339-343.

[80] Munson, B., Gerhart, P. M., Gerhart, A. L., Hochstein, J. I., Young, D. F., and Okiishi, T. H., 2016, *Fundamentals of fluid mechanics*, John Wiley & Sons, Inc., New Jersey, US.
[81] Lewis, R., 1996, *Turbomachinery performance analysis*, John Wiley & Sons, Inc., London UK.
[82] Volk, M., 2005, *Pump characteristics and applications*,Taylor & Francis.
[83] Stepanoff, A., 1957, *Centrifugal and axial flow pumps: theory, design, and application*, John Wiley & Sons, Inc. New York US.
[84] Nourbakhsh, A., 2008, *Turbopumps and pumping systems*, Springer, Berlin, Germany.
[85] Toptop, K., and Kadipasaoglu, K., 2013, "Design and numeric evaluation of a novel axial-flow left ventricular assist device," American Society for Artificial Internal Organs Journal **59**(3), pp. 230-239.
[86] Csandy, G., 1964, *Theory of Turbomachines*, McGraw-Hill, New York, US.
[87] Epple, P., Durst, F., and Delgado, A., 2010, "A theoretical derivation of the Cordier diagram for turbomachines," *Proceedings of The Institution of Mechanical Engineers Part C, Journal of Mechanical Engineering Science*, pp. 1-15.
[88] Arnold, W., and Bourque, K., 2013, "The engineer and the clinician: Understanding the work output and troubleshooting of the HeartMate II rotary flow pump," The Journal of Thoracic and Cardiovascular Surgery, **145**(1), pp. 32-36.
[89] Castegnaro, S., 2018, "Aerodynamic Design of Low-Speed Axial-Flow Fans: A Historical Overview," Designs, **2**(3), pp. 20.
[90] Kim, J.-H., and Kim, K.-Y., 2012, "Analysis and Optimization of a Vaned Diffuser in a Mixed Flow Pump to Improve Hydrodynamic Performance," Journal of Fluids Engineering, **134**(7), pp. 071104-071110.
[91] Okamoto, E., Hashimoto, T., Inoue, T., and Mitamura, Y., 2003, "Blood Compatible Design of a Pulsatile Blood Pump Using Computational Fluid Dynamics and Computer-Aided Design and Manufacturing Technology," Artificial Organs, **27**(1), pp. 61-67.
[92] Untaroiu, A., Wood, H., Allaire, P., Throckmorton, A., Day, S., Patel, S., Ellman, P., Tribble, C., and Olsen, D., 2005, "Computational Design and Experimental Testing of a Novel Axial Flow LVAD," American Society for Artificial Internal Organs Journal, **51**(6), pp. 702-710.
[93] Smith, W., Allaire, P., Antaki, J., Butler, K., Kerkhoffs, W., Kink, T., Loree, H., and Reul, H., 2004, "Collected Nondimensional Performance of Rotary Dynamic Blood Pumps," American Society for Artificial Internal Organs Journal, **50**(1), pp. 25-32.
[94] Stanfield, J., Selzman, C., Pardyjak, E., and Bamberg, S., 2012, "Flow characteristics of continuous-flow left ventricular assist devices in a novel open-loop system," American Society for Artificial Internal Organs Journal, **58**(6), pp. 590-596.
[95] Asama J., Shinshi, T., Hoshih, H., Takatani S., and A., S., 2006, "A Compact Highly Efficient and Low Hemolytic Centrifugal Blood Pump With a Magnetically Levitated Impeller," Artificial Organs, **30**(3), pp. 160–167.
[96] Apel, J., Neudel, F., and Reul, H., 2001, "Computational Fluid Dynamics and Experimental Validation of a Microaxial Blood Pump," Americal Asociation of Artificial Internal Organs Journal, **47**(5), pp. 552-558.
[97] Sieß, T., Reul, H., and Rau, G. n., 1995, "Concept, Realization, and First In Vitro Testing of an Intraarterial Microaxial Blood Pump," Artificial Organs, **19**(7), pp. 644-652.
[98] Selgrade, B., 2010, "Fluid Dynamics of a Centrifugal Left Ventricular Assist Device " M.S. Thesis, Department of Biomedical Engineering, Duke University.

[99] Marsden, A., Bazilevs, Y., Long, C., and Behr, M., 2014, "Recent advances in computational methodology for simulation of mechanical circulatory assist devices," Wiley interdisciplinary reviews: Systems biology and medicine, **6**(2), pp. 169-188.
[100] Burgreen, G., Antaki, J., Wu, Z., and Holmes, A., 2001, "Computational fluid dynamics as a development tool for rotary blood pumps," Artificial Organs, **25**(5), pp. 336-340.
[101] Zhu, L., Zhang, X., and Yao, Z., 2010, "Shape Optimization of the Diffuser Blade of an Axial Blood Pump by Computational Fluid Dynamics," Artificial Organs, **34**(3), pp. 185-192.
[102] Malinauskas, R., Hariharan, P., Day, S., Herbertson, L., Buesen, M., Steinseifer, U., Aycock, K., Good, B., Deutsch, S., Manning, K., and Craven, B., 2017, "FDA Benchmark Medical Device Flow Models for CFD Validation," American Society for Artificial Internal Organs Journal, **63**(2), pp. 150-160.
[103] Stewart, S., Hariharan, P., Paterson, E., Burgreen, G., Reddy, V., Day, S., Giarra, M., Manning, K., Deutsch, S., Berman, M., Myers, M., and Malinauskas, R., 2013, "Results of FDA's First Interlaboratory Computational Study of a Nozzle with a Sudden Contraction and Conical Diffuser," Cardiovascular Engineering and Technology Journal, **4**(4), pp. 374-391.
[104] Gordon, D., 1979, *Hydraulic systems*, Ottawa, CA.
[105] Kundu, P., and Cohen, I., 2008, *Fluid mechanics*, Academic Press, Amsterdam.
[106] White, F., 2008, *Fluid mechanics*, McGraw-Hill, New York, US.
[107] Wolf, S., 1983, *Guide to electronic measurements and laboratory practice*, Prentice-Hall, New Jersey, US.
[108] Untaroiu, A., Throckmorton, A., Patel, S., Wood, H., Allaire, P., and Olsen, D., 2005, "Numerical and experimental analysis of an axial flow left ventricular assist device: the influence of the diffuser on overall pump performance," Artificial Organs, **29**(7), pp. 581-591.
[109] Lorenz, M., and Smith, W., 2002, "Rotodynamic pump scaling," American Society for Artificial Internal Organs Journal, **48**(1058-2916 [Print]), pp. 419-430.
[110] Park, J., Oki, K., Hesselmann, F., Geirsson, A., Kaufmann, T., and Bonde, P., 2019, "Biologically Inspired, Open, Helicoid Impeller Design for Mechanical Circulatory Assist," American Society for Artificial Internal Organs Journal, Publish Ahead of Print.
[111] Kannojiya, V., Das, A., and Das, P., 2019, "Numerical simulation of centrifugal and hemodynamically levitated LVAD for performance improvement," Artificial Organs, **44**(2), pp. E1-E19.
[112] Sorgüven, E., Ciblak, N., Okyar, F., Akgun, M., Egrican, A., Safak, K., Ahn, H., Lazoglu, I., Küçükaksu, D., 2007, "Flow Simulation and Optimization of a Left Ventricular Assist Device," *ASME 2007 International Mechanical Engineering Congress and Exposition*, pp. 1401-1407.
[113] Throckmorton, A., Kapadia, J., Chopski, S., Bhavsar, S., Moskowitz, W., Gullquist, S., Gangemi, J., Haggerty, C., and Yoganathan, A., 2011, "Numerical, hydraulic, and hemolytic evaluation of an intravascular axial flow blood pump to mechanically support Fontan patients," Annals of Biomedical Engineering, **39**(1), pp. 324-336.
[114] Delaux, A., 2017, "Design of a Left Ventricular Assisting Device for Congestive Heart Failure Condition," McGill University.
[115] Farooqi, K., 2017, *Rapid prototyping in cardiac disease : 3D printing the heart*, Springer, Cham, Switzerland.
[116] Crosby, J., DeCook, K., Tran, P., Smith, R., Larson, D., Khalpey, Z., Burkhoff, D., and Slepian, M., 2015, "Physiological characterization of the SynCardia total artificial heart in a mock circulation system," American Society for Artificial Internal Organs Journal, **61**(3), pp. 274-281.

[117] Friedberg, J., Chavez, M., Young, J., Daigle, J., and Taylor, C., 2016, "Liquid Property Control System for LVAD ISO 5198 Testing and Mock Circulatory Loop Simulations," *32nd Southern Biomedical Engineering Conference (SBEC)*, pp. 33-34.
[118] Charles, E., 2013, "Modernization of the Mock Circlatory Loop: Advanced Physical Modeling, High Performance Hardware, and Incorporation of Anatomical Models," Ph.D. Thesis, Virginia Commonwealth University.
[119] Tomaiuolo, G., 2007, "Blood-mimicking fluid for Biotechnological Applicationds. Fluidodynamic Behaviour of red blood cells and droplets under confined shear flow," Ph.D. thesis, Università di Napoli Federico II.
[120] Bumrungpetch, J., 2016, "Mechanism design of Ventricular Assist Device," Ph.D. thesis, Mechanical Engineering, Queensland University of Technology.
[121] Pekkan, K., Aka, I. B., Tutsak, E., Ermek, E., Balim, H., Lazoglu, I., and Turkoz, R., 2018, "In vitro validation of a self-driving aortic-turbine venous-assist device for Fontan patients," The Journal of Thoracic and Cardiovascular Surgery, **156**(1), pp. 292-301.
[122] Trusty, P. M., Tree, M., Maher, K., Slesnick, T. C., Kanter, K. R., Yoganathan, A. P., and Deshpande, S., 2019, "An in vitro analysis of the PediMag and CentriMag for right-sided failing Fontan support," Journal of Thoracic and Cardiovascular Surgery, **158**(5), pp. 1413-1421.
[123] McKean, A., 2018, "Numerical Simulations of a Hubless Axial Flow LVAD," McGill University.